DEEP ULTRAVIOLET SURFACE INSPECTION WITH PHOTOEMISSION ENHANCEMENT

by

Benjamin Duaine Buckner

A Dissertation Presented in Partial Fulfillment
of the Requirements for the Degree
Doctor of Philosophy

ARIZONA STATE UNIVERSITY

December 2002

DEEP ULTRAVIOLET SURFACE INSPECTION WITH PHOTOEMISSION ENHANCEMENT

by

Benjamin Duaine Buckner

has been approved

July 2002

APPROVED:

______________________________, Chair

____

____

____

____

Supervisory Committee

ACCEPTED:

____

Department Chair

____

Dean, Graduate College

ABSTRACT

The potential utility of surface inspection with deep ultraviolet (DUV) light has been explored from a theoretical and experimental standpoint, with the construction of a high-vacuum DUV scatterometer and photoemission measurement system. DUV based inspection has the possibility of extending surface inspection technology to meet the needs of the semiconductor industry into the era of 70 nm critical dimensions in three major respects, the enhanced light scattering cross-section from small defects and structures at shorter wavelengths, the material-sensitive properties of photoemission, and the photoemission voltage contrast effect. Experimental results in the 140 nm to 240 nm wavelength range roughly confirm theoretical predictions of the scattering cross-section in the DUV and also reinforce the idea that photoemission techniques could constitute important new inspection modes. Clear evidence of photoemission voltage contrast is also shown, and absolutely calibrated measurements of photoemission yield indicate that signal levels are sufficient to allow the use of photoemission in high-speed inspection with laser sources. Issues surrounding DUV and vacuum inspection technology are analyzed, and approaches to solving related problems, such as vacuum actuator heating and mirror fouling by carbon deposition, are discussed.

To kith and kin multifarious.

ACKNOWLEDGEMENTS

The author would like to thank the Semiconductor Research Corporation for funding this project under task 733.001.

Thanks are also due to Adriaan Stellingwerff, Thomas Heller, Jon Duncan, Jake Fehrman, Euiwon Bae, Sang-Youp Lee, Brent Nebeker, Joe Iamphungporn, and Jim Hale for helping with all the bits and pieces and to Rick Jarvis for providing a particularly essential sample.

The forbearance and of Tugan, Kuhlun, and Matthias during periods of the author's distraction should also be recognized, as well as Mark Davis' valiant experiments with ceramic circuit boards.

And finally, gratitude is expressed to Dr. Hirleman and Dr. Roedel for many years of support, moral and otherwise.

TABLE OF CONTENTS

Page

LIST OF TABLES ix

LIST OF FIGURES x

I. INTRODUCTION 1

A. Project summary 1

B. Background 1

C. Project description 6

1. DUV scatterometer construction 6

2. DUV light scattering measurements 9

3. DUV photoemission measurements 13

4. Photoemission voltage contrast 17

C. Significance of the project 21

II. HEUDI SYSTEM DESIGN 23

A. Overview 23

B. Hardware 26

1. Vacuum system 26

2. Stage assembly 28

3. Detector assembly 33

4. Optical source train 35

5. Interfacing electronics 50

C. Software 52

D. Experimental setup 54

Page

III. DUV SCATTERING MEASUREMENTS 60

A. Measurement and calculation of BRDF 63

B. Unpatterned silicon sample 68

C. 700 nm PSL sample 76

D. HARI sample 85

1. S-polarization measurements 89

2. P-polarization measurements 97

3. Comparison with Diffraction Theory 101

IV. DUV-STIMULATED PHOTOEMISSION MEASUREMENTS 103

A. Photoemission apparatus 104

B. Analysis 108

C. Experiments 113

1. Initial material contrast samples 113

2. Carbon deposition experiment 117

3. HARI photoemission measurements 123

V. PHOTOEMISSION VOLTAGE CONTRAST MEASUREMENTS 137

A. First chrome mask 139

B. Second chrome mask 146

VI. SUMMARY AND CONCLUSIONS 157

A. Experimental topics 157

1. Scattering 157

2. Photoemission 159

Page

3. Photoemission voltage contrast 159

B. Implications for practical DUV inspection.. 160

C. Future work 161

REFERENCES.. 164

APPENDIX

I. SURFINDUV FILE FORMATS 169

A. X-Y Scans.. 170

B. Angle Scans 173

LIST OF TABLES

Table Page

1. Photoelectric Thresholds of Common VLSI/ULSI Materials. 16

2. UVG-5 photodiode spectral responsivities. 112

3. Second mask incident powers and PE yield factors. 146

4. XY file, line 3 field headers. 171

5. XY file, line 5 field headers. 172

6. XY file, 2nd to last line field headers. 172

7. ANG file, line 3 field headers. 173

8. ANG file, line 5 field headers. 174

LIST OF FIGURES

Figure Page

1. Regions of the ultraviolet spectrum. 5

2. Proposed DUV scatterometer/SPEEM with broad-band source (not to scale). 9

3. Total scattering cross section as a function of wavelength for a 60 nm diameter polystyrene latex particle on a Si wafer. 10

4. DUV scatterometer with excimer laser source (not to scale). 13

5. DUV scatterometer (side view) 25

6. Stage assembly (dimension in inches). 29

7. MgF_2 Rochon polarizer characteristics. 41

8. Lens focal lengths (index data from Crystran Optics'). 45

9. 50-mm MgF_2 lens focal spot. 48

10. Interfacing system. 52

11. Screen shot of control software (electronic noise). 53

12. System coordinates 55

13. General optical configuration and focusing system. 57

14. Relative wavelength response at atmospheric pressure with Hamamatsu R7311 PMT and Xe flash lamp. 65

15. PMT response curve at high vacuum. 66

16. Full-throughput avg. power during pulse - MgF_2 lens, atmospheric pressure, 3 nm bandwidth. 67

17. Sample mounted in chamber (PMT tube has been rotated to face the camera). 69

18. Initial 550 nm large spot scan to locate deposition region (bright spot at upper right). 70

19. HEUDI control software screen shot. 200 nm wavelength scans with 200 μm spot size. 72

Figure Page

20. BRDFs of sample features at 200 nm wavelength. Bare silicon substrate, 45° incidence angle, spot size approximately 200 μm. Specular beam at 0°.................. 74

21. 20 × 10 mm map of deposition boundary area, 230 nm unpolarized light at 40° incidence, scan angle 30°, spot size 100 μm. 77

22. Angle scans from suspected 700 nm PSL spheres. 78

23. Particle 6 beam profile (used for calibration), 230 nm, 45° inc., 30° detector. 80

24. Particle 6 scans compared with DDSURF simulation for n=1.55. 81

25. Predicted DSCs for 700 nm spheres of varying *n*, 45° inc., 230 nm unpolarized light, on Si. 83

26. Diagram of HARI wafer via arrays. (Inset courtesy of Rick Jarvis of SEMATECH.) 87

27. Large-area scatter map of HARI wafer. 200 nm, 45° inc. Arrow shows A1 array with defects (inset, 50 μm resolution). 88

28. DUV real and imaginary indices of refraction for Si and SiO_2. 89

29. Scattering by HARI via array for various angles of incidence, *s*-pol. 180 nm, beam width approx. 0.3 mm at normal. 90

30. Scattering by HARI oxide background for various angles of incidence, s-pol. 180 nm, beam width approx. 0.3 mm at normal. 91

31. Surface plot of spectral scattering by a via array vs. angle, *s*-pol., 45º inc. 92

32. Contour map for FIG. 29. 93

33. Surface plot of spectral scattering by background oxide vs. angle, *s*-pol., 45º inc. 94

34. X-Y scan of via arrays A1 (with programmed defects, upper) and A2 (without defects, lower) at 180 nm, 45º incidence, *s*-pol., detector at 37º. 95

35. X-Y scan of arrays A1 and A2, 190 nm, 45º incidence, *s*-pol., detector at 32.5º. 96

36. Dark field (upper) and bright field (lower) scans of A1 at 460 nm, *p*-pol., 45º inc. Both scans cover a 1.4 × 1.6 mm area. The apparent shift in position is reproducible and may be an optical effect of the underlying SiO_2 layer. 98

37. Scattering from A1 area and bare area, 220 nm, *p*-pol., 45º inc. 99

Figure Page

38. Scattering from A1 area and bare area, 200 nm, *p*-pol., 45º inc. 100

39. Experimental, predicted, and fitted angular positions of the first and second diffraction orders from the HAR via arrays *vs*. wavelength.................................... 102

40. PE rate with varying deflection filter voltage (aluminum, at 185 nm). 107

41. Wide area (10 mm × 22 mm) 185 nm photoemission scan of sample A, Al foil on glass.. 114

42. Signal variation along Y direction (X = -7.66 mm) of FIG. 38. 115

43. PE line scans of BiCMOS wafer, 60° incidence (90° = normal) at 185 nm and 230 nm wavelengths. 116

44. Mean count rates (per 3 µS pulse) from Si for different wavelengths. 117

45. Reflection signal vs. beam exposure time. 121

46. Large spot via array scan, 200 nm illumination at normal incidence. Left- scatter at 60º, middle – scatter at 52º, right – photoemission. 126

47. Spectral Si (fiducial) to SiO_2 contrast for the HARI sample (95% conf. interval from sample error < 5%). 128

48. PE rate vs. distance between lens and sample for Si wafer at 230 nm.................... 130

49. 9-mm focal lens photocurrents. 131

50. Si signal and SiO_2 signal vs. distance. 132

51. PE from vacuum grease on clean aluminum. 133

52. 160 nm PE yields for via array A1 and bare Si, for second experiment. 135

53. Chrome photoemission current at 160 nm *vs*. bias voltage. 138

54. Chrome mask patterned region. 140

55. X-Y map of chrome mask photocurrent with 150 nm illumination (sample rotated about 45°), mean counts per 5 µs pulse. 141

Figure Page

56. Chrome mask photocurrent at 160 nm, right chrome area grounded (above) and floating (below). Position in mm, mean counts per 5 μs pulse. 142

57. PE current map for a horizontal strips (at the 2.0 mm vertical position) with varying right-area bias voltages (-10, -1, gnd., +1, +10 V). 145

58. 190 nm PE scan of area between two 50 um-wide grounded chrome strips........... 148

59. Strips and background at various filter voltages (160 nm illumination)................. 150

60. 190 nm scan of strips at -0.73 V potential (area 8 mm wide by 5 mm high).......... 151

61. Chrome strips with varying contact potentials at 140 nm....................................... 154

I. INTRODUCTION

A. Project summary

The aim of this work is to explore the possibilities of deep and vacuum ultraviolet illumination in high-speed surface inspection technology. In addition to dealing with the extension of traditional visible-wavelength light-scattering methods into this domain, this work will also examine the potential of photoemission, which is not a significant effect at traditional visible-light inspection wavelengths, to extend and enhance surface inspection technology.

To meet this aim, the project will consist of four major task categories:

1. Design and build a DUV electrooptical scatterometer
2. Measure DUV scattering from various samples
3. Measure photoemission from relevant samples
4. Demonstrate and analyze photoemission voltage contrast

In particular, scattering and photoemission from high-aspect ratio features will be observed, since inspection of such features is particularly problematic with current inspection systems and there is good reason to believe that shorter wavelengths will be more suitable for high-aspect-ratio inspection (HARI).

B. Background

High-speed wafer inspection technology is continually challenged by the decreasing dimension of integrated circuit structures. With IC critical dimensions now

considerably smaller than visible-light wavelengths, older visible-light optical inspection technologies simply cannot satisfactorily detect the smallest defects of interest. Developments along two distinct paths are addressing this problem, that of short wavelength (UV) optical systems and that of electron-beam systems.

Short-wavelength optical systems rely on improvements in imaging resolution and increases in scattering cross-section sometimes gained at UV illumination wavelengths. For certain types of inspection, these improvements may well be adequate for some years to come. This short-wavelength trend is generally expected to meet the needs of unpatterned wafer inspection for instance. On the other hand, for inspection of the densest patterns, the ultimate adequacy of UV illumination is as yet uncertain. Optical systems as well are generally thought to be incapable of directly observing out-of-specification electrical properties, though this is not necessarily the case as will be seen later.

Electron-beam systems, conversely, are capable of more than sufficient imaging resolution to permit observation of even the smallest topographic defects that will be of interest in the next decade. Electron-beam systems are also capable of directly observing electrical properties via voltage contrast. However, electron-beam systems suffer a number of disadvantages over their optical counterparts, most clearly in speed. Even the fastest e-beam inspection technologies are orders of magnitude slower than even low-throughput optical systems. This problem arises from considerations of beam diameter, total electron flux, and the comparatively large background signal. When inspecting electrically insulating surfaces, electron-beam systems are also often stymied by the same

charging effects which allow them to perform voltage contrast measurements. These charging effects also can be sensitive to subsurface features such that deep complex patterns may introduce unacceptable levels of pattern-originated noise. Furthermore, electron beams can damage sensitive structures and lightly coat surfaces with carbon buildup. Electron-beam systems also require vacuum and tend to be much larger than optical systems.

For many of these problems, various solutions have been proposed. Speed might be improved by increased electron gun brightness, massively parallel multi-beam systems, or contrast-improving filter techniques (energy, angle, or even polarization). Charging can be controlled by the environmental-SEM approach or by carefully controlling the beam energy.[1] Damage and subsurface sensitivity can similarly be controlled by proper energy selection. However, all of these solutions do require considerable engineering effort to implement and often require sacrificing some aspects of system performance.

The requirement of vacuum is somewhat less of an objection in comparison to UV systems, since UV systems may at some point require a degree of rarefaction in the ambient to control Rayleigh scattering by vacuum fluctuations in the ambient gas, though this effect could be reduced by using helium as well.[2] Wavelengths less than 200 nm will require vacuum or an alternative ambient due to the high optical absorption of air in that spectral region.

UV systems present new technological challenges as well, though these are not generally so daunting as those of electron-beam systems. Major concerns still lie in the

area of UV light sources, which are more usually more expensive and difficult to operate than visible-light sources. No readily available coherent UV sources yet exist for wavelengths between 157 nm and around 40 nm. Sub-40 nm (EUV/X-ray) coherent sources exist but are currently prohibitively expensive.

There is some question as to whether coherent or incoherent sources are preferable for this application, though. Coherent sources are used in the visible wavelengths mostly for the sake of brightness, plus the relative ease of engineering monochromatic optical systems and interpreting monochromatic diffraction patterns. However coherent UV radiation can lead to unwanted noise from interference effects due to small process variations that are too small to introduce significant phase variations with visible-wavelength coherent light.[3] Thus, incoherent DUV/VUV-emitting sources, which are readily available with tens or hundreds of watts of broad-band output power, might prove suitable for future commercial inspection systems.

Another concern is that UV radiation can produce damaging chemical and physical effects which are not encountered to any great extent in visible light. UV is more prone to breaking chemical bonds and so can produce chemical changes in both the materials of the optical train (as in the well-known solarization effect) and in inspected materials. This chemical effect is also sometimes responsible for deposition of air-borne contaminants, via the same hydrocarbon-cracking mechanism seen in e-beam carbon deposition.[3] UV light is also more prone to producing fluorescence, though there is currently no clear evidence that fluorescence will prove to be a significant difficulty.

This and most of the above effects tend to become more and more pronounced as wavelength decreases though.

From experiences in UV lithography and current research presumably underway among various inspection-system vendors, these technological challenges of UV inspection appear to be fairly well understood in the near ultraviolet region (400 - 300 nm) (FIG. 1).

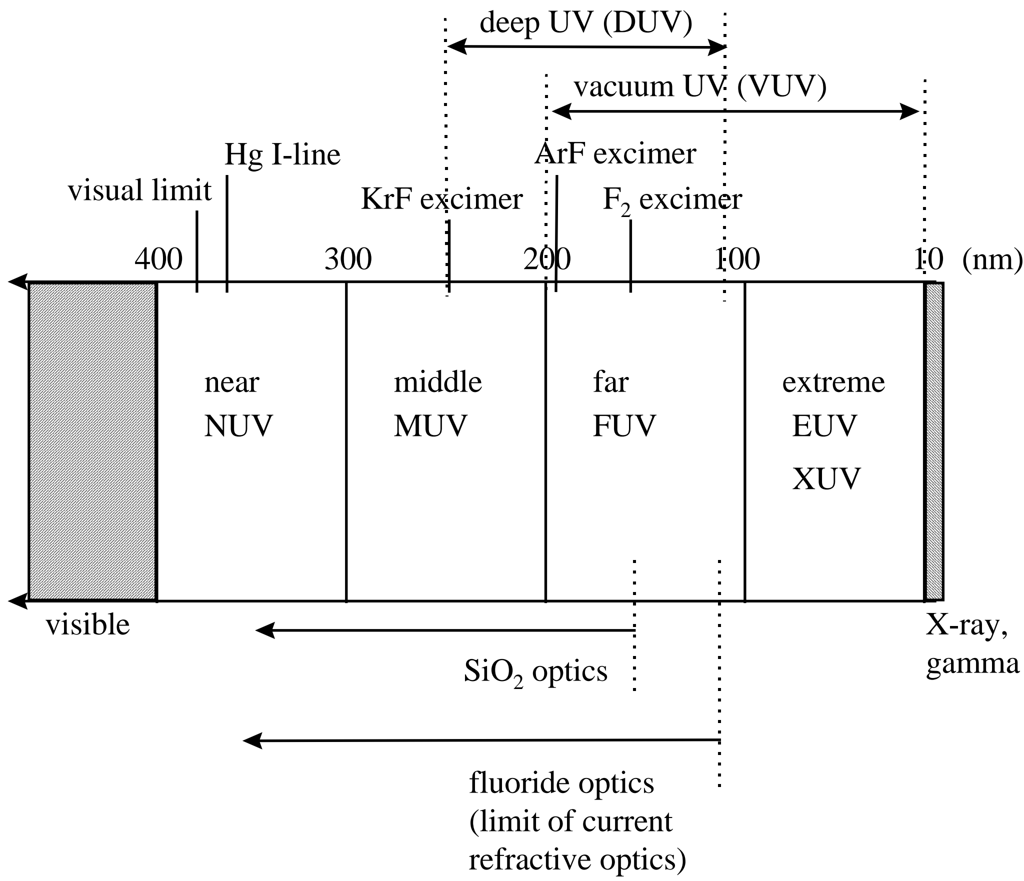

FIG. 1. Regions of the ultraviolet spectrum.

However, the potential utility and technological difficulties of inspection using light in the "deep" ultraviolet (DUV) is far more poorly understood than in the more

familiar NUV spectrum. This area is currently the forefront of optical lithography research. In recent years, some scatterometric work has been performed with broad-band UV scattering for measurement of particulate levels in various media,[4,5] and for DUV scattering by surfaces[6-9] but there has been little work concerning the fundamental properties of DUV scattering and on DUV scattering by particles on surfaces.

Indeed, the term DUV itself is somewhat murky in its definition. The excimer laser wavelengths of 248 nm (Ar-F) and 193 nm (Kr-F) are generally considered to belong to this region in the lithography literature, and for the purposes of this work the DUV will be considered to run from 250 nm to 115 nm. (Below 115 nm no materials suitable for refractive optics are available.) The better part of the DUV, from 200 nm down, lies in the vacuum UV (VUV), in which significant partial pressures of air cannot be present in the optical train due to absorptive properties of oxygen and water vapor.

Consequently, the present work is proposed to explore technological potential and challenges of DUV-based surface inspection both with experiments conducted with a newly constructed DUV research instrument and with theoretical analysis.

C. Project description

1. DUV scatterometer construction

Central to the project's completion is the construction of the DUV scatterometer apparatus. There are to date only two other known DUV scatterometers in existence, so there is no standard blueprint for the system, though visible-light scatterometers are well understood, having been the subject of an entire book now in its second edition.[10]

Additionally, this system is somewhat unique in that it aims to simultaneously measure photoemission and scattering.

We may immediately lay out several obvious requirements for the design:

- Vacuum environment - Needed for UV below 200 nm in wavelength and for photoelectron measurement. Also useful for suppressing Rayleigh scattering by the ambient.
- Scanning stage - Required for sample positioning, as microstructures are to be measured.
- Optical source train - UV source and optics.
- Optical detector assembly - UV detectors and detector positioning.
- Electron detector - Measures photoelectron current.

In fact, scanning photoemission electron microscopy (SPEEM) systems have been a subject of interest for some time, particularly since the late 1980s and early 1990s, when groups in Germany and the United Kingdom built and demonstrated SPEEMs with micron or submicron-scale lateral resolution.[11-18] In many ways, the DUV scatterometer is simply a SPEEM with optical detectors, so that many proven design elements of SPEEM systems can be applied to this project. This instrument is not intended (primarily) as a qualitative analysis tool though as are most SPEEMs, so no energy-resolution features were planned for the electron detector. A simple deflection plate was however mounted on the channeltron detector for separating photon and photoelectron signals, and it can function as a very simple energy filter.

The target wavelengths of the system were planned to be from 120 nm up to around 250 nm, depending on the capacities of the particular source ultimately chosen. The shorter wavelengths were preferred, so that the source selection and wavelength-specific design considerations were biased in favor of the 150 - 200 nm (upper VUV) range. Wavelengths above 200 nm (MUV) were desirable as well, but MUV capability was to be sacrificed for VUV performance if necessary. As realized, the source met these objectives and had considerably better long wavelength performance than required.

The 120 nm short-wavelength limit is determined by the transmission of the refractive optics, which are composed of fluorides. Fluoride optics typically can be made transparent at wavelengths no shorter than 115 nm. Fluoride lenses are considerably more expensive than silica-based lenses, but the added cost is considered to be worth the added capability, particularly given the possibility of a future upgrade to a VUV excimer laser. The greatest drawback to using fluoride optics is in the availability of high quality lenses. Fluoride lenses with high numerical apertures (NAs) in particular are hard to obtain, and aberration-corrected lenses or lens sets such as aspheres, achromats, and aplanats are virtually unavailable in optics catalogs, which puts limits on the smallest achievable focal spot. For very high NA, reflection objectives are essentially the only option not involving custom design and manufacturing.

From these considerations, a diagram of the proposed system arises (FIG. 2).

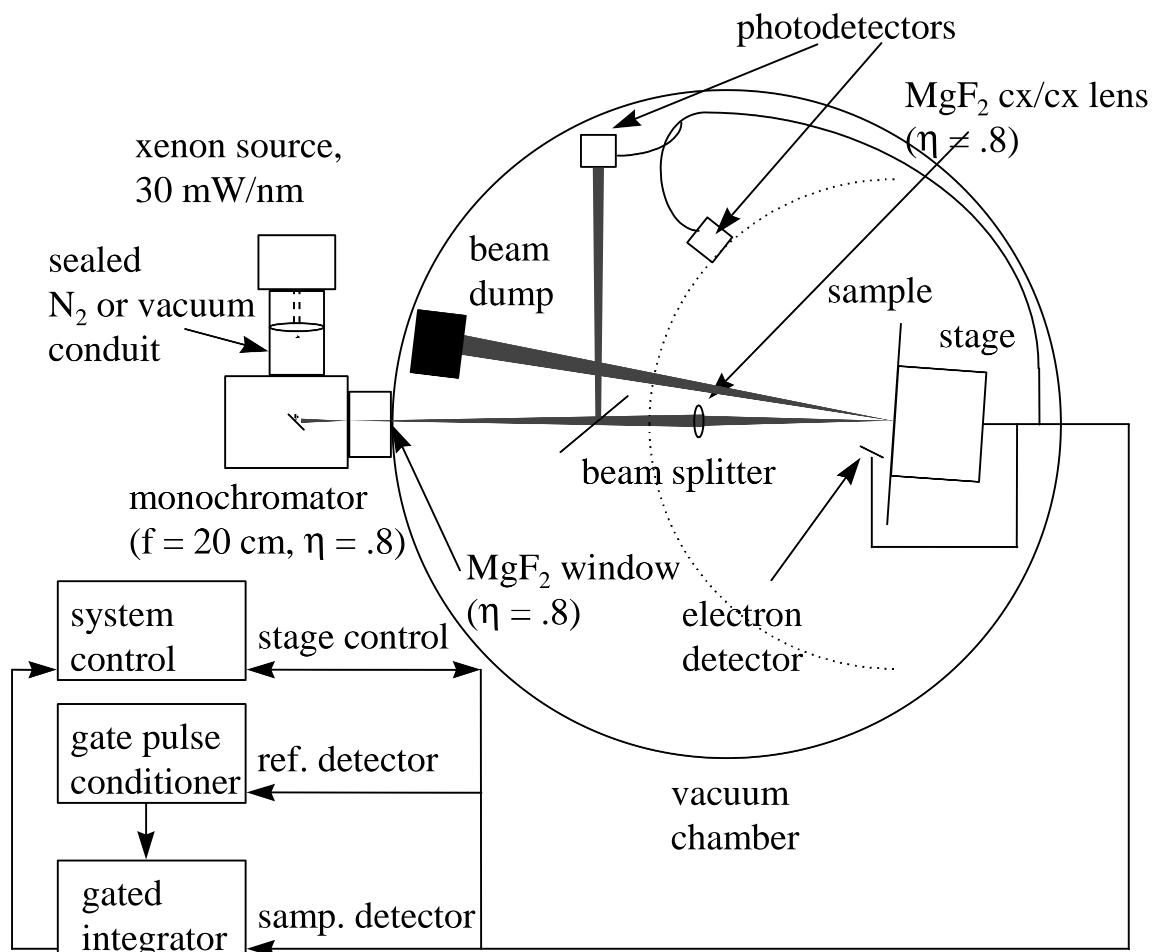

FIG. 2. Proposed DUV scatterometer/SPEEM with broad-band source (not to scale).

Unforeseen concerns were expected to arise in the design and construction of this instrument, and discovery and resolution of difficulties particular to the DUV regime was a significant motivation for this research.

2. DUV light scattering measurements

One of the chief purposes of the DUV scatterometer is naturally to perform scattering measurements in the DUV wavelengths. This will allow comparison with

currently existing scattering models to test their validity in the DUV regime, particularly to confirm predictions that nanoparticle scattering cross-sections will be greatly increased when compared to visible-wavelength illumination.

Electromagnetic scatter modeling performed in previous work by the author and colleagues shows the dramatic increase in scattering cross section by sub-100 nm particles for DUV illumination, FIG. 3.

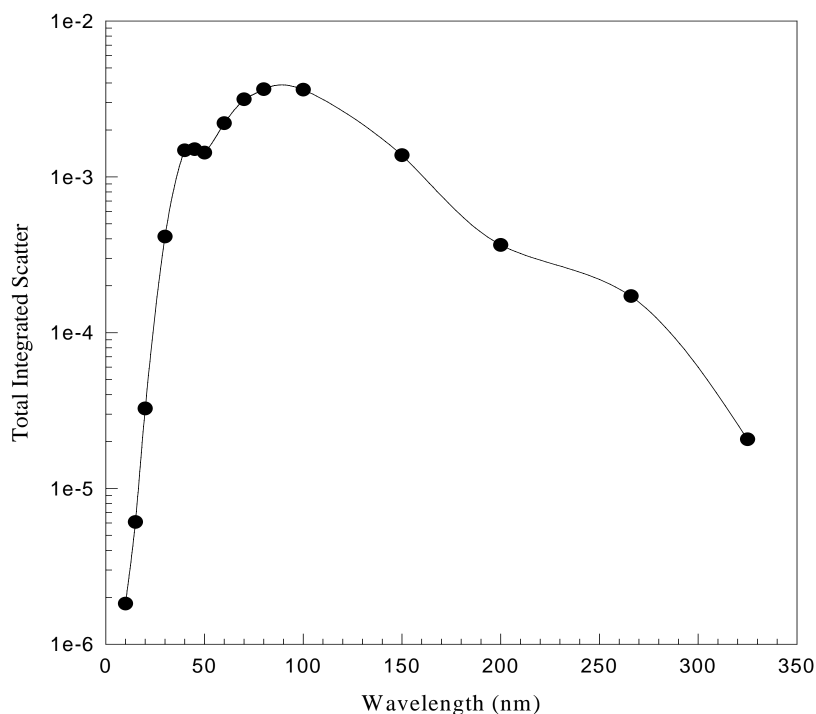

FIG. 3. Total scattering cross section as a function of wavelength for a 60 nm diameter polystyrene latex particle on a Si wafer.[2]

The system was also to allow measurement of scattering cross-sections of more complex features for which scatter modeling is not yet considered reliable. Of particular

interest are high-aspect-ratio (HAR) features, for which current inspection technologies are considered inadequate. It was once thought that scattering from HAR via features would increase as wavelength decreases, however some earlier modeling and experimental results had suggested that scattering non-intuitively increases with wavelength and that the cross-section would be relatively insensitive to the deep inner structure of the via in regimes where the via inner diameter is smaller than or nearly the same as the illumination wavelength, at least in the visible spectrum.[19]

This effect can be explained by observing the resemblance of sub-wavelength apertures to near-field optical probes,[20] such that we can think of a sub-wavelength-diameter via as a sort of near-field probe of its own interior, with the attendant exponential decay of the field away from the surface (an evanescent wave). We should though keep in mind that along with this evanescent component that results from "leakage" of the interrupted surface reflection, there is also a transmitted component as well.

The decay length (analogous to penetration depth) of the evanescent wave of course is proportional to wavelength, so in that respect, shorter wavelengths reduce the likelihood of the via bottom to be illuminated, explaining why sub-wavelength diameter vias, at least in a certain regime, have deeper light penetration with longer wavelengths. However, for DUV radiation, the via diameters are of the same scale as the wavelength, so the field can be expected to begin to lose its evanescent character at some point, improving the penetration.

Thus it was suspected that the extremely short wavelengths available in the DUV scatterometer might lie sufficiently far from this regime for vias of interest to reverse the wavelength trend and allow optical interrogation of the via interior. It was as well thought that accompanying photoelectron measurements might provide a means to probe the critical deep interior of the via structure, since some common types of via contamination should produce changes in material contrast.

Other potential applications particularly well-suited for DUV scatterometry are width measurements of extremely small critical dimensions, since shorter wavelength illumination can measure thinner lines than what could be measured at visible wavelengths.[21] This is of particular interest for the metrology of increasingly fine-dimensioned ULSI processes.

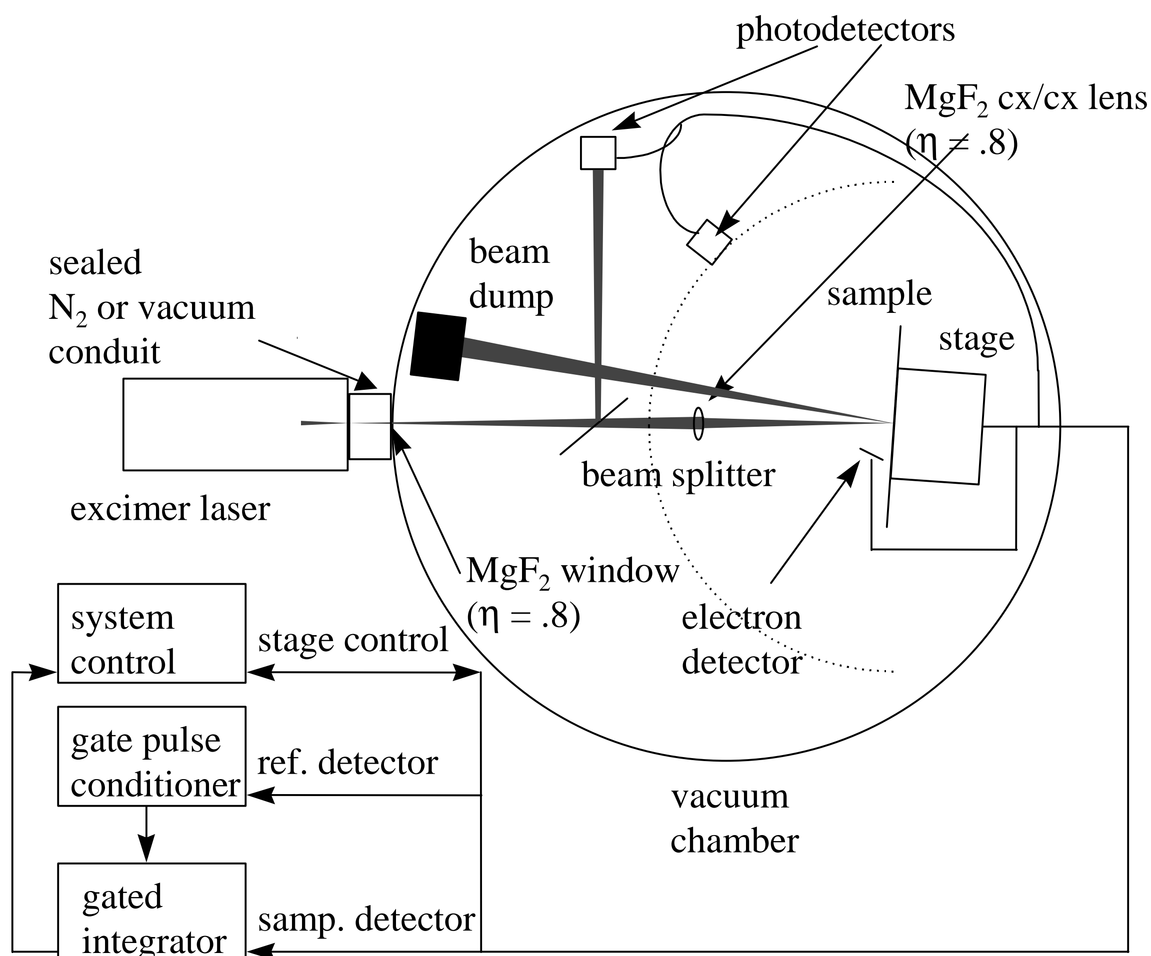

FIG. 4. DUV scatterometer with excimer laser source (not to scale).

3. DUV photoemission measurements

The DUV scatterometer is also unique in that it is designed to gather not only the light-scattering data as in a traditional scatterometer but also photoemission data. Photoemission electron microscopy (PEEM) in itself has a long history, dating back to the work of Brüche in 1933,[22] however, as mentioned earlier, it has only in the past decade been realized as a high resolution scanning microscopic technique.[17] In this form, its potential convergence with short-wavelength scanning optical scatterometric

techniques is somewhat obvious, since both utilize scanned highly focused UV light. However, SPEEM is mostly viewed as a qualitative analytical technique, with topographic contrast mechanisms considered little more than an undesirable artifact, indeed a "pronounced" artifact as observed in a recent work on artifacts in SPEEM contrast formation.[23] Of course, one technology's artifact is often another technology's fundamental principle; we can reasonably expect that SPEEM contrast can provide information on both topographic and material defects in ULSI structures.

Analytical SPEEMs also must operate in ultra-high vacuum (UHV), primarily to prevent ambient gasses from adsorbing to the sample (which is normally cleaned beforehand) and thus obscuring or weakening the desired signal. In the current application though, the instrument is intended to observe surface contaminants as well as to inspect samples which have been exposed to normal atmosphere for some time. Thus, cleaning the surface is out of the question and any adsorbable gasses will have long since adsorbed, so there is really no benefit to using UHV as opposed to weaker vacuum in such a system. The reduced photoemission current is an unavoidable tradeoff required by the application.

It is in fact desirable to operate the system in the weakest possible vacuum, since in an industrial production environment excessive pump-down time would introduce costly throughput limitations. The maximum residual gas pressure would of course ultimately be limited by the attenuation of photoelectron signal due to collisions with gas molecules though.

This leads to the question of how strong the expected photoemission signal will be, a particularly critical issue in wafer inspection, since the photoemission yield will set the ultimate limitation on inspection speed. This is rather difficult to answer precisely, though the next section will attempt an approximate prediction.

Table 1 shows the photoemission threshold wavelengths for materials commonly encountered on the surfaces of VLSI and ULSI wafers. Most non-insulating materials might seem to begin to photoemit in the MUV, however it must be remembered that the surfaces in this application will be rather contaminated relative to usual photoemission experiments. Virtually all oxide-forming materials will have at least a thin layer of native oxide. The emission depth for photoelectrons is also quite small, such that even thin surface oxide layers can block emission from underlying material. The oxide layers themselves of course are insulating (at least in bulk) and therefore have much higher photoemission thresholds than the underlying metals. This problem is somewhat alleviated for near-threshold UV photoemission at which photoelectron energies are in the 1 to 10 eV range. For such electron energies the mean free paths are considerably longer than at higher energies seen in X-ray photoemission.[24] This does lead to something of a tradeoff, though, since higher energy illumination yields more photoelectrons per photon but at the same time many of those added photoelectrons also have higher energies and thus have a shorter escape depth. This project is expected to yield insights into these tradeoffs, which are not so commonly encountered in UHV analytical SPEEM work, which tends to use higher photon energies for the sake of photoelectron energy spectroscopy.

Table 1. Photoelectric Thresholds of Common VLSI/ULSI Materials. Si, Ge, and GaAs from Cardona and Ley[25], SiO_2 estimated as $\frac{1}{2}E_G+\chi$ from ionization energy data in Porter et al.[26], and Si_3N_4 estimated assuming E_g=5 eV, χ=2 eV.

Material	Threshold (eV)	Threshold (nm)
SiO_2	11.7 (7.2 - traps)	106 (170 - traps)
Si_3N_4	~7 (~4.5 - traps)?	~180 (~280 - traps)?
GaAs	5.5 - 5.6	220
Si	5.15	241
Ge	4.80	258
Cu	4.65	270
W	4.6	270
Al	4.3	290

Photocurrents can depend as well on topographic effects arising from spatial non-uniformity of electromagnetic fields at the surface, non-uniform electrostatic potentials, or even from scattering of photoelectrons by surface structures. Arnold[27] notes observations of enhanced photoemission by micron-scale particles, which is attributed to their electromagnetic resonances (a phenomenon that can be simulated by electromagnetic scattering packages such as DDSURF[28]).

Even without topographic effects, first-principles modeling of photoemission is of course quite complicated, particularly with respect to predicting the energy and angular distribution of emitted electrons, and theoretical predictions often diverge significantly from experiment. Electromagnetic scattering modeling is somewhat more mature, and allows some confidence in computed field distributions. So, for a basic approach to topographic photoemission contrast, we may be able to apply a relatively simple photoemission model to fields computed with scatter modeling.

For metals and sometimes for other materials, photoemission current near the threshold is related to the square of the difference between photon energy and the photoemission threshold in an expression often known as the Fowler-Nordheim equation[29]

$$j(\omega) = A(\hbar\omega - E_T)^2 \tag{1}$$

Within a few *kT* of the threshold, the current deviates from this expression due to spreading of the Fermi level.[25] The expression also fails for insulators and semiconductors with large thresholds, since a vertical transition in k-space from the valence band edge then requires some sort of additional scattering process to conserve momentum. At some second threshold energy above the first threshold, higher energy non-vertical transitions may occur as a faster second-order process, at which point the usual quadratic behavior is seen. The relation at energies between these thresholds is linear in the energy difference,

$$j(\omega) = A_1(\hbar\omega - E_{T1})\,. \tag{2}$$

The two thresholds are however usually no more than a few tenths of an eV apart.

Deviations may also occur under several other conditions, but the power of the energy difference is generally less than 2.5. Kane[30] treats the peculiarities of photoemission from semiconductors thoroughly.

4. Photoemission voltage contrast

Among the more interesting possible applications of photoemission surface inspection is to observe voltage contrast, since voltage contrast inspection is often

considered to the exclusive province of SEM-based inspection. In SEM, the electron beam charges surface structures and the nature of electrical connections of that structure determine the rate at which the charge dissipates, ultimately affecting the electrostatic potential of the structure and thus the SEM image. This has obvious applications in testing IC structures in process, particularly for contacts.

Photoemission, however, even though no electron-beam illumination is involved, charges surface structures as well, a fact which has been known for many years.[31] This produces potential differences in surface structures in the same manner as with SEM voltage contrast. These potential differences are then observed in the photoemission current via the retardation of the emitted electrons.[23]

Photoemission voltage contrast (PEVC) differs from SEM VC in several notable ways. First, PEVC always charges the surface to a positive potential, whereas SEM VC usually charges it to the negative (though it is possible to achieve positive charging for some beam energies). This difference has several conceivable uses. First SEM charging could be actively countered via photoemission. Since charging of insulating substrates is a significant problem in SEM-based inspection of insulating substrates, use of UV illumination in conjunction with a SEM inspection system might enable its use for layers for which it was previously unsuited. This effect (called “photodepopulation”) has been demonstrated incidentally as a spectroscopic method used to study the energies of SiO_2 traps.[32]

Second, spatially separated UV and electron beams could be used for non-contact testing of individual circuit paths. Traditional voltage contrast is essentially limited to

observing structure-to-ground connections, but e-beam/photoemission voltage contrast could allow observation of structure-to-structure connections, at least those which have significantly lower resistance than either connection has to ground. Similar techniques have in fact been realized (though on comparatively large scales) with multiple electron beams[33,34] and with single contacts detecting photoemissively generated currents.[35]

The most significant feature of photoemission voltage contrast though is that the illumination wavelength may be selected to suppress background photoemission substantially. VC observations are generally conducted against an insulating background, upon or through which the conductive structures extend. With e-beam observations, this background layer will produce a background signal. Even though a metal structure (particularly a well-grounded contact) may produce a larger signal, this background still reduces the contrast and thus the speed and accuracy of the observation.

With PEVC the photon energy may be selected below the insulator's threshold (recalling that metals tend to have much lower PE thresholds than insulators) but above the metal's threshold. Thus, the PEVC background should be comparatively darker than the SEM VC background. This contrast enhancement may allow either faster evaluation of individual contacts or equivalently a larger beam spot (simultaneous observation of a larger number of contacts).

Using the shot-noise limited detection model developed by Buckner *et al*. we can analyze the maximum detection speed for a set of contacts, if we make a few assumptions. We take a field consisting of 25 cylindrical contacts, each of 0.2 μm diameter, all illuminated by a circular beam 5 μm in diameter with, for simplicity, a flat

irradiance profile. Further we assume a flux of 10^{16} photons/s (8 mW for a 248 nm wavelength beam) and we assume that the photoelectric yield from the contacts will be 10^{-4} electrons/photon and the photoelectron detection efficiency is 50%. Each contact will receive 0.16% of the photon flux, such that the 25 contacts totally receive 4% or 4×10^{14} photons/s, yielding 4×10^{10} electrons/s, of which 2×10^{10} are detected (3 nA, a respectable current in an e-beam system). The background photoemission (from SiO_2) will be assumed negligible. If one contact is totally missing, the detected electron flux will drop to 1.92×10^{10} e/s. This might also be expressed as 4% contrast. The question then is how long must this flux be integrated such that this difference is reliably detectable, assuming shot noise to be the limiting noise source?

The answer can be computed numerically with little effort. With a background of 5×10^4 photons/sample, a contrast of approximately 4% is sufficient to enable a 95% detection probability and 1 false count in 10^{11} samples. So, this flux could be sampled at roughly $2\times10^{10}/5\times10^4=4\times10^5$ samples/s. For our 5 μm spot and a 200 mm wafer, we would need approximately $(2\times10^5\ \mu m / 5\ \mu m)^2=1.6$ billion samples, such that it would require about 4000 seconds to scan an entire wafer full of such contacts. Slightly more than an hour per wafer might seem like a long period at first glance, but it is 50 times faster than the speed achievable by current e-beam systems and is also in line with the ambitious hour-per-wafer goals for e-beam inspection modes set at a recent SEMATECH workshop on the subject.[36]

The shot-noise limited model is simplistic though, ignoring other noise sources as well as the difficulty of rastering the beam at a shot-noise limited rate. Non-shot-noise

variance sources tend to be hard to quantify and rather system specific, so we must be content at this stage only to note their existence and the fact that they will slow the system to some degree. The rastering rate issue can however be addressed at least in a qualitative manner. We should recall that these calculations assumed a 5 μm diameter spot. This size is quite large by the standards of electron beams and so does not require anything approaching the raster rates of an e-beam system. It is on the small side for an optical beam (several times smaller than the typical configuration, though it would not be unreasonable to speculate that some commercial systems already use a spot size near this), but we should recall that optical inspection systems operate in terms of wafers per minute. Thus it would seem highly likely that full wafer rastering of a 5 μm optical beam in the period of 1 hour is entirely possible. UV illumination might complicate rastering systems somewhat since electrooptic beam steering is not an option below a certain wavelength (due to absorption in the active material, *e.g.* $LiNbO_3$, which absorbs strongly in the UV[37]), but mechanical beam steering is not uncommon in current inspection systems.

Thus, in addition to the advantages of short-wavelength optical scatterometry, utilization of photoemission effects in a DUV scatterometer should also provide much faster access to some important e-beam inspection modes.

C. Significance of the project

Ultimately, the results of this project should enable the development of more sophisticated high-speed surface inspection systems. As has been shown, UV inspection may provide alternative approaches to applications now only tractable with off-line SEM-

based inspection. This would allow additional capabilities to be added to the conventional sphere of optical systems, such that a single DUV inspection system might be able to perform the most significant tasks of several contemporary inspection systems, yielding savings in terms of industrial floor space and facilities. Such a system would also probably be considerably less costly than an electron-beam system.

The ultimate feasibility of high-speed inspection systems can often be determined by an analysis of shot-noise performance limitations, which requires knowledge of both the detected defect signal and background signal.[38] This project will provide information on those critical parameters.

II. HEUDI SYSTEM DESIGN

A. Overview

The hybrid-emission deep ultraviolet inspection apparatus (FIG. 5) is designed to take light scattering and photoemission data from a sample surface positioned with 1 µm X-Y resolution at high vacuum (or at atmospheric pressure for longer wavelength scattering measurements). The vertical-mount sample stage allows computer-controlled translation over a 25 mm (25 000 µm, ~1 inch) range in both directions and additionally may be manually rotated around a vertical axis to select incidence angles from 0 to 90º. A motorized Z-direction stage allows the surface of a sample up to 12.5 mm (1/2 inch) thick to be positioned coincident with the eucentric axis of the stage, if eucentric stage rotation is required. Illumination is currently provided by a 20 W (maximum average power) broad-spectrum pulsed Xe lamp which feeds into a monochromator capable of selecting wavelengths from 120 nm (vacuum UV) to 550 nm (visible yellow). The bandwidth is selectable from 0.1 nm (high monochromaticity, low incident power) to 10 nm (low monochromaticity, high incident power). Most experiments are performed in the 240 nm – 140 nm range, although fortuitous emission peaks allow some measurements to be performed around 460 nm and 520 nm as well.

The optical detector apparatus revolves under computer control in a horizontal plane around the stage rotational axis over a 270º range, though in practice this is usually somewhat more restricted by mechanical interference with the converging lens assembly. The detector mount supports a photomultiplier tube, which transduces the optical signal

to a low-noise, high-gain electronic signal. This signal is then processed through a Stanford Research Systems SR250 gated integrator (GI) to discriminate the microsecond-scale scattering signal from background noise. The GI output is converted to a digital reading by an analog-to-digital conversion card in the controlling computer system. This same data path processes the signal from an electron detector (in high vacuum operation) to measure photoemission signals.

The current photoemission detection apparatus is an Amptek 501 channel electron multiplier (often known as a "channeltron") with digital output. It is supplied by a 15 V DC power source and uses its own on-board circuitry to provide the internal high voltage for avalanche amplification and charge-cloud detection. Since this is a digital instrument, its output signal is measured in discrete and uniform (5 V) pulses. The detection software actually analyzes the analog GI signal to calculate the number of these digital pulses arriving within the GI gate pulse, effectively as a software-based gated counter. This approach was chosen since it was initially unclear whether the highly sensitive channeltron would be required for the system or a simpler analog Faraday cup would be sufficient, and it was desired to determine the true requirements before introducing another level of complication to the hardware by adding a gated counter. The Faraday cup output is, of course, a pulsed analog signal, and it is thus as well suited to acquisition by the GI as the photomultiplier output sign is. Further experience with the system has shown that the Faraday cup will not usually be sensitive enough for use with the present source, but the software counting system has worked well enough that this arrangement will probably be retained for the foreseeable future. Future experiments with a brighter,

more powerful source (such as an excimer laser) may well be suitable for the more easily calibrated Faraday cup detector though.

A source pulse rate of around 50 Hz and a high-bandwidth computerized data collection system (utilizing direct memory access) allow acquisition of 50 samples per second, though in some cases the speed is limited by positioning delay. Rates up to 300 Hz are also possible with slight modification of the pulse generation electronics but probably not useful in most cases. Windows-based graphical control software allows easy navigation from low-resolution scans to acquire high-resolution X-Y and angle scans of target features.

This chapter discusses the system design in two sections, the first dealing with the hardware and the second with the software.D

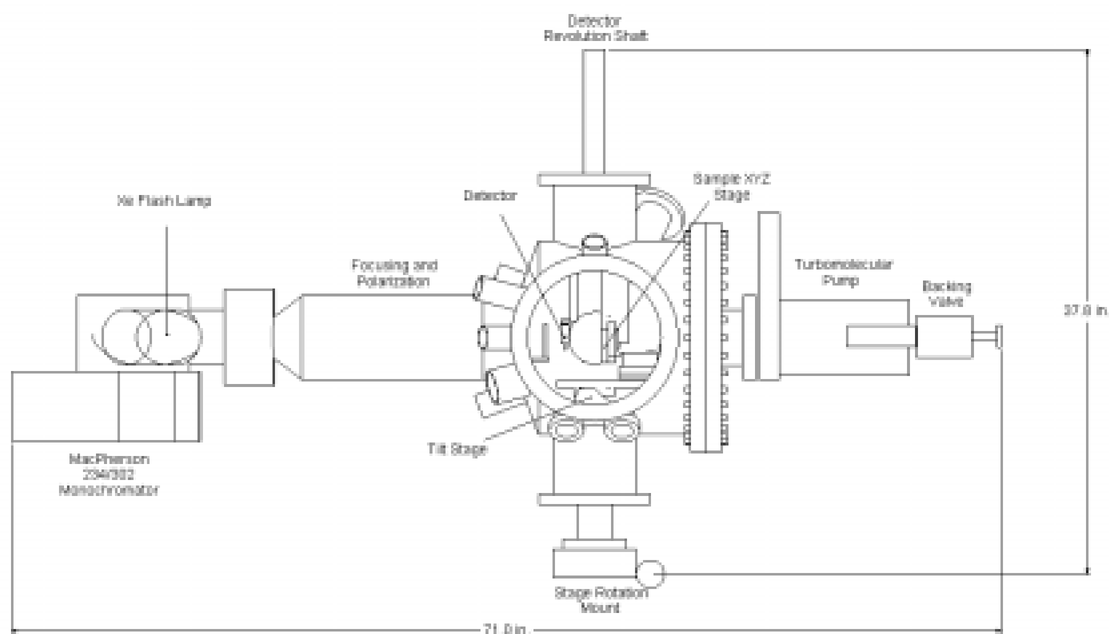

FIG. 5. DUV scatterometer (side view)

B. Hardware

The HEUDI system comprises five major hardware subsystems, the vacuum system, the stage assembly, the detector assembly, the optical source train, and the interfacing electronics.

1. Vacuum system

The vacuum system includes the chamber, pumping apparatus, and vacuum gauges, mostly standard off-the-shelf vacuum equipment. It is designed to achieve high-vacuum operation with pressure no higher than 10^{-4} Torr with a pump-down time of less than 30 minutes, and the system does reach this level in as little as 10 - 15 minutes. After several days at high vacuum, pressures as low as 4×10^{-7} Torr have been reached, so the vacuum system in general performs beyond the requirements. This allows some additional flexibility with the design of the internal experimental apparatus, since there is a fair amount of excess evacuation capacity to handle "virtual leaks" from gas traps such as unvented screws or absorptive materials such as flock paper.

The chamber is a slightly modified version of MDC Vacuum Products' SSAC-12 Surface Science Analysis chamber. This vessel is composed of electropolished 304 stainless steel and provides a variety of standard-sized ports for vacuum feedthrough mounting and equipment connection. The chamber is normally 12" in diameter, but the modified version increases this to 14" to allow more room for the stage motors and mounting 8" diameter samples. The standard large side port, upon which the quick-access door will be mounted, has also been enlarged from an 8" to a 10" diameter to accommodate 8"-sample loading. Fully motorized 8" translation is not possible with

these modifications but an 8” sample can be mounted and most of its area will be accessible to the probe beam. This has been deemed a good tradeoff between the expense, pumping-volume, and logistical problems associated with full 8” translation stages and the utility of being able to mount 8” wafers.

The roughly cylindrical chamber is mounted with its long axis horizontally, in order to provide the most efficient use on chamber volume for the application.

The roughing pump is a Leybold Trivac D16B. With a nominal volume flow rate of 13.4 ft^3/min (~380 l/min), this pump exceeds the requirements of the system, which it can rough in less than the five minutes required for the turbopump to reach operating speed, allowing valveless operation of the turbopump, at least when unusual loads are not present. The total volume of the high-vacuum section is approximately 37 liters and the low-vacuum optical train segment encloses only about 5 liters more space. Most of the roughing system is provided with 1.5” diameter tubing, connected by easily removable compression clamps, although the present roughing pump (and high-vacuum pump) are connected with narrower 1” fittings.

The roughing system connects to the chamber through a valve and is equipped with gauges to help the operator prevent the oil-sealed roughing pump from being directly connected to the chamber in molecular flow.

The high-vacuum pump is an Osaka Vacuum TF160CA, a greased-bearing turbomolecular pump, which can be horizontally mounted. This pump requires a backing flow rate of at least 80 l/min and has a start-up time of five minutes. Its volume

flow rate is approximately 160 l/s. This pump connects to the front end of the chamber and is valveless in the current configuration.

2. Stage assembly

The stage assembly (FIG. 6) is the most mechanically complex system, supplying five degrees of positioning freedom, of which three are motorized and two are computer-controlled. It holds and positions the sample. The assembly is supported by a custom-designed Thermionics rotary feedthrough with manual positioning. It provides the ability to select incidence angle.

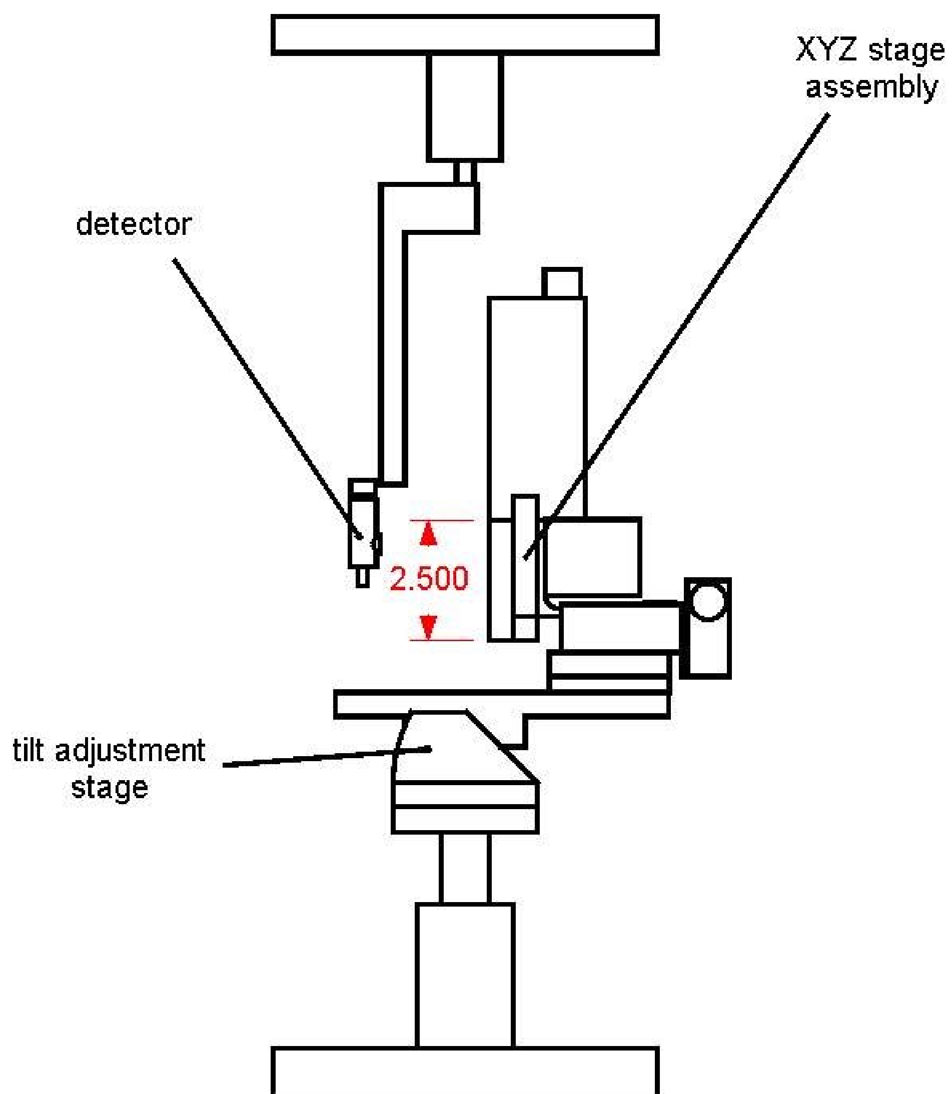

FIG. 6. Stage assembly (dimension in inches).

This feedthrough can be equipped with a separate high-vacuum pump to allow stage rotation under vacuum without pressure bursts, but such bursts are not noticeable at normal operating pressures. Custom design was primarily required to cope with the

weight of the stage assembly, which exceeds the limits of off-the-shelf models, typically around 10 pounds.

The feedthrough supports a small mounting bracket which in turn supports a vacuum-compatible manual tilt stage. The SD Instruments tilt stage ensures that the vertical surface of the X-Y stage can be made plumb and so only needs occasional adjustment with the system at atmosphere (the alignment can be performed with the monochromator set to visible output, compatible with atmospheric operation).

In the original mount a long plate connects the tilt stage to the Newport 462-XYZ positioning stage. This arrangement allows the tilt stage to rest directly over the feedthrough shaft to reduce axial strain (compensated for by the tilt stage).

An alternative mount has also been constructed which provides more space for mounting 8" wafers, but it removes the tilt stage and so lacks the capability for azimuthal adjustment.

The X-Y-Z stage presents its X-Y plane vertically, with the Z-axis long the horizontal. The Z-axis is motorized (but manually controlled) with a vacuum-compatible New Focus picomotor actuator. This motor was chosen for its short length (due to its space-critical position), although it allows a ½" positioning range out of the 1" available to the stage. Its main function is to allow the sample surface to be positioned to coincide with the rotational axis of the stage assembly (and the lens focal point). Since it is horizontally mounted, the picomotor only needs to push against stage friction, so as not to exceed its rather limited load capacity.

The X and Y stages are moved independently by identical Newport 850 GV actuators. These actuators have 2" ranges, but the actuator range is not fully utilized due to the 1" range of the stages. The 850s are capable of sub-micron positioning resolution, are available as standard vacuum-compatible parts, provide feedback for closed-loop operation, and have non-rotating shafts to improve accuracy and reduce particle generation. This last feature is especially important since they will be operated more frequently than any other actuators in the system. The focusing stage uses the same actuator, so that a single control unit can economically operate all three.

A major obstacle encountered during the implementation of the actuator system was thermal buildup during vacuum operation. At atmospheric pressure, the actuators can operate continuously for an indefinite period without excessive heat buildup. However in vacuum, the loss of the convective heat transfer mode seems to allow heat to build slowly, so that after an hour or two of vacuum operation (or applying holding torque), the motor temperatures rise to levels that can damage the mechanism.

This problem was ultimately diagnosed by observing the odor of decomposing insulation and subsequent measurements of temperature after repressurization, but not before several units were damaged to the point of inoperability.

The problem was successfully dealt with by two means. First, the scanning software routines were altered. The motors are now normally shut down when not moving the stage, rather than providing a holding torque as previously. The disadvantage of this is that some drift in position can occur (observable from the encoder output), but typically only by a few micrometers. The software also now offers a "spiral scan" mode.

In this mode, the scan begins at the upper left position and works around the scan rectangle in a spiral pattern, ending the scan in the center of the scan rectangle. This reduces the motor temperature compared to the raster scans, because while the total distance moved is approximately the same, the distance and operating time is more evenly divided between the motors. In the raster scan mode, either the X or Y motor is operating almost continuously, so that the rastering motor tends to build up far more heat.

The second temperature reduction step was more involved. It was observed that the only significant heat conduction path from the motors in vacuum would have to be conduction, since radiation heat loss would not be significant for a body slightly above room temperature in a room-temperature chamber, at least not until the motors had already exceeded a safe operating temperature. Examination of the motor mounts revealed that the cross-sectional area of the motor-to-mount contact surface was quite small due to the beveling of one of the parts. The contact area between the mount and the stage body was severely constricted as well. Cross-sectional area of course is a major factor in thermal conductance, so a new mount was designed and machined, increasing the minimum cross-sectional areas. In addition, the new mount was fabricated from high-conductivity oxygen-free copper instead of the aluminum of the original mount. This in itself provided around a 50% increase in conductivity, multiplying the original conductance by an estimated factor of 5.

These steps succeeded in significantly increasing the motor life, although after about six months of operation (probably hundreds of hours of scans) the new motors have

begun to display excessive operating noise, which was an early symptom of the overheating problem.

3. Detector assembly

The detector assembly is relatively simple but does include one motorized and computer controlled degree of freedom, angular rotation. The optical detector consists of a Hamamatsu R7311 photomultiplier tube (PMT) with its base and biasing network. The PMT is suspended from a thin arm, which attaches to the shaft of a vertical rotary feedthrough, also from Thermionics. This feedthrough mounts on top of the chamber, directly over the stage assembly and the bottom rotary feedthrough. The detector arm feedthrough only carries a small (though highly eccentric) load. This feedthrough is motorized and computer controlled to allow angle-resolved scans of the scattering signature.

The drop-down arrangement of the detector arm allows considerable freedom in implementing the focusing system since the two components only interfere with each other if the focusing lens and detector come into contact. Their respective mountings should never collide.

The PMT has a dark current of about 0.3 nA and can put out a maximum current of about 10 mA for a 1/1000 duty cycle (0.01 mA maximum average), giving a total dynamic range of about 7½ decades. This is less range than could be achieved with a solid-state detector, but the sensitivity of a solid state detector would be marginally adequate for the scattered powers expected to be encountered, given the low brightness of the source. The incident beam can probably saturate the PMT, but with the microsecond

pulses used it is generally more practical to attenuate the beam to accommodate a more sensitive detector than to increase the useful gain on the back end of a less sensitive detector.

The channeltron electron detector (an Amptek MD-501) is mounted in a tray that attaches to the tilt stage, which keeps it directed toward the sample. This arrangement also prevents the channeltron from directly “seeing” the cold-cathode ion gauge mounted in the light-source direction. The ion gauge of course emits both electrons and ions in large abundance and can actually damage the channeltron with excessive charged particle currents. Even with the unit well protected from the gauge, sample measurements cannot be performed while the gauge is in operation, but the mounting reduces the gauge current to non-damaging levels. As well as protecting the channeltron from accidental damage, this has some slight diagnostic utility in that the channeltron may be switched on momentarily while the gauge is operating to determine whether the channeltron is working.

The channeltron’s 15 V DC power is provided by the same low-noise power supply that the PMT uses, with a separate switch to allow the unit to be turned off at intermediate vacuum levels. In the glow discharge region, the high voltages inside the channeltron will cause extensive arcing and likely damage, so making sure the channeltron is not activated during pump down or repressurization is critical. The switch has a lighted red/green LED to make the channeltron state easy to notice.

The distance from the channeltron to the sample can be varied somewhat by inserting shims between the back of the unit and the bottom of the mounting tray. Earlier

designs also had the aperture about ¾" off center, although the mount has now been modified to center the aperture, which somewhat increased the photoelectron collection efficiency.

A Faraday cup detector was also tried in a number of configurations, but the photocurrents seem to be too low to be detectable without the multiplication effect. If we consider that the channeltron can read a maximum electron flux of around 10^6 pulses per second (per manufacturer specifications), this must correspond to a current of about 0.1 pA. The current electronics cannot detect a current much smaller than perhaps a 10 - 100 nA, although under the right conditions (no apertures, fully-open monochromator slits) the system can generate photocurrents perhaps 100 times the channeltron's upper limit. Even this though puts the photocurrent just under the electronic detection limit, so a Faraday cup probably will not be usable with this system without a much more powerful source and a better preamplifier. The advantage of the Faraday cup would be that it is much easier to calibrate.

4. Optical source train

The optical train must deliver light from the source to the sample, converging and, for wavelength-specific experiments, monochromating the broadband source. Laser sources would be preferable in terms of monochromaticity and brightness, and a few excimer laser sources are available in the VUV range, but they are quite expensive and require special facilities. For the experimental work currently intended in this project, the brightness of broadband sources is adequate, so their lower cost and flexibility make them preferable here. However, nothing precludes the use of other sources, such as 193

nm Kr-F or 157 nm F-F excimer lasers. When the beam is highly stopped, the source provides power on the order of microwatts (picojoule pulses) during the duty cycle, although the full beam can approach milliwatts (nanojoule pulses). By comparison, current DUV pulsed excimer sources can easily provide multi-millijoule energies in the DUV, at many times the pulse rate. Effectively, contemporary DUV sources can provide as much incident power as the sample will bear without damage. While the powers in this experimental apparatus are miniscule, it should be borne in mind that in an industrial inspection system, the powers and flux rates could be a million times larger or more.

a. The VUV transmission problem

Primarily because of absorption by air (chiefly by oxygen and water molecules), the inter-component gaps in the optical train cannot of course lie in an air ambient, as they normally would in a longer-wavelength system. There are several possible approaches to dealing with this difficulty.

First, the train could be constructed entirely within the vacuum chamber. The primary disadvantage to this is in taking up excessive amounts of space within the chamber itself.

Second, the bulkier components could be situated outside the chamber and the light conducted through some non-absorptive medium. This does require though that a highly UV-transmissive window into the chamber be available. Three good possibilities for this medium are optical fibers, which can be somewhat expensive at these wavelengths due to the high quality of the required material, evacuated cavities, or

nitrogen-filled cavities, since dry nitrogen is quite transparent down to wavelengths of 125 nm.[39,40]

The low cost of nitrogen and the minimal engineering difficulties involved with simple atmospheric-pressure enclosures might recommend the last option, however most VUV equipment is designed for vacuum operation, so in practice is it seems to be easier to evacuate the source train.

The maximum allowable pressure can be computed easily enough from the VUV absorption of air and the optical path length, which is approximately 20 cm through the medium vacuum region. Empirically, the required pressure has been observed to be less than around 0.08 mTorr.

Thus the system can be constructed with the source, collimation, and monochromation optics external to the chamber and abutting the UV source window. The final converging lenses are inside the high vacuum region, since the working distances are fairly short, usually from 50 to 7 mm.

The optical source train provides the illumination that probes the sample. It contains several custom-built optical components along with one computer-controlled motorized stage and a manually adjusted monochromator. It is also the section estimated to be the most critical to the success of the instrument, providing the limited available optical power to the sample.

Most of the source train occupies a separate low-vacuum section of the system, divided from the high vacuum by a CaF_2 window. This allows the vacuum in either section to be maintained while the other is brought to atmospheric pressure, facilitating a

number of testing and maintenance tasks. It also reduces the total high vacuum area considerably, since the long-thin optical train has a much higher ratio of surface area to volume than the main chamber, and it isolates the lamp coupling from the high vacuum as well. This allowed considerable simplification of the lamp coupling, which can now be provided with a simple o-ring.

b. The mid-vacuum monochromated collimated light source

The train begins with the EG&G (recently acquired by Perkin-Elmer) 1162 Xe flash lamp which is mated to the optimized source coupling with an o-ring, as described. The source coupling was custom designed by MacPherson to optimize optical throughput into the MacPherson 234/302 Monochromator. It uses high-efficiency and achromatic reflective optics. The monochromator is fitted with a 1200 lines-per-inch grating, yielding a wavelength range from 550 nm down to about 10 nm, although the limitations of the transmission windows in other components only allow the use of wavelengths down to 120 nm. Bandwidth is also selectable from 10 nm to 0.01 nm, allowing both high accuracy/low throughput and low accuracy/high throughput operation. The monochromator is however the limiting term in the optical system's throughput (entendue or optical invariant) so the adjacent optics were carefully designed to ensure its full utilization. While this was expensive (making the optical train the most costly subsystem), the critical nature of the optical train demands that we eschew risky economizations, which are more appropriate to the more pedestrian vacuum system, for example.

The monochromator output passes to the compact MacPherson collimator unit, which is similar to one used in their VUV spectroscopy systems. This uses reflective optics, similarly to the source coupler and monochromator, to produce a collimated beam somewhat less than 1” in diameter.

c. The polarizer

The polarizer used in the HEUDI system is a MgF_2 Rochon polarizer. No absorption polarizers such as dichroic films are usable in the DUV, so the practical choices for a polarizer are essentially limited to prism polarizers and reflection polarizers. Reflection polarizers tend not to have good rejection ratios and usually have significant wavelength dependence in both reflectivity and extinction ratio, as well as being difficult to mount in a confined space, as is true of most off-axis optical elements. However, reflection polarizers can function well enough in the VUV to be usable. Prism polarizers are generally superior to reflection polarizers in most respects, but most prism polarizers are made of strongly birefringent calcite crystals, which are not VUV-transmissive.

Fortunately, one of the most important VUV transmission-optics materials MgF_2 is mildly birefringent, and VUV prism polarizers made from it are commercially available from a few manufacturers. Only two types of prism polarizers are practically important at these wavelengths, the Wollaston and Rochon polarizers. The operational difference between the two is that the Wollaston refracts the two polarization branches away from the optical axis, while the Rochon only refracts one branch and transmits the second branch directly. Thus the Wollaston achieves twice the angle of separation between the two, but at the cost of being difficult to align. The angle of separation varies

with wavelength too, so a Wollaston prism would have to be accompanied by additional beam steering elements, making it a fairly significant challenge to mount. Rochon polarizers also have one less reflection for the directly transmitted polarization, giving greater throughput. Consequently, the Rochon polarizer was used despite the reduced angle of separation.

The particular polarizer used is a CVI Laser RCHP-5.0-MF, with a specified deviation angle of 5 degrees at 193 nm. This specification somewhat oversimplifies the situation, since Rochon polarizers have asymmetrical deviation angles,[41] a fact which is seldom commented upon by manufacturers, who may fail to indicate the direction of a particular component. The deviation angle δ given the prism cut angle S and indices of refraction for the deviated branch in the entrance prism n_1 and in the exit prism n_2 is

$$\delta = \sin^{-1}\left(n_1 \sin(S)\cos(S)\left(1-\sqrt{1+\frac{n_2^{\,2}-n_1^{\,2}}{n_1^{\,2}\cos^2(S)}}\right)\right) \tag{3}$$

The asymmetry arises because n_1 and n_2 may respectively be the ordinary index of refraction n_o and the extraordinary index of refraction n_e or *vice versa*. Changing the entrance and exit sides around can alter the magnitude of the deviation angle by 30% or more with MgF_2, which can have a significant impact on the design.

This expression may often be approximated by

$$\delta \cong \sin^{-1}\left(\pm\,\Delta n \tan(S)\right) \tag{4}$$

where Δn is the birefringence, (n_e- n_o), however this number usually fails to capture the full impact of the asymmetry and roughly reflects the mean magnitude of the two deviation angles.

The inter-prism angle for the polarizer used was measured to be 79.6° and using tabulated MgF_2 index of refraction data, we can compute the deviation angles, FIG. 7.

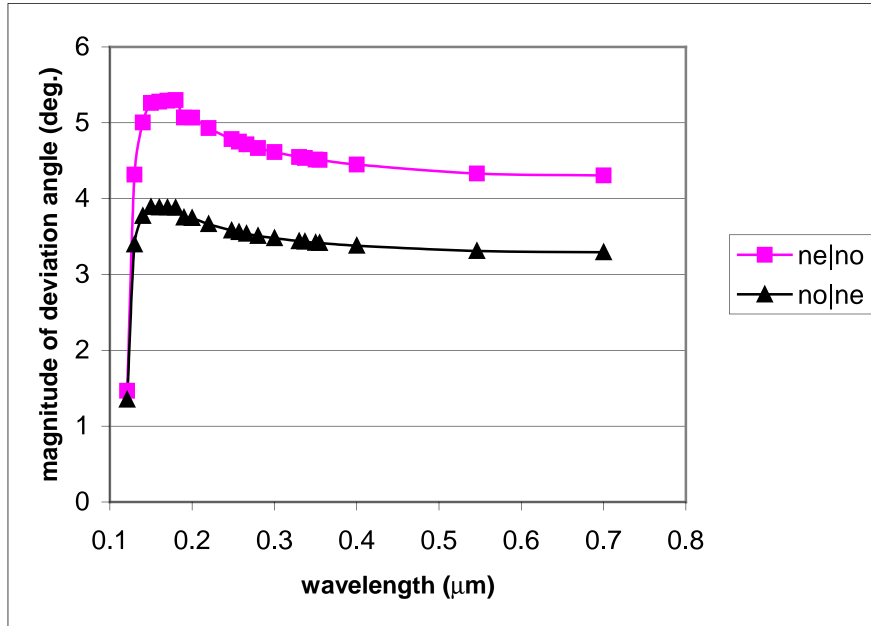

FIG. 7. MgF_2 Rochon polarizer characteristics.

Determining the orientation of an unmarked polarizer is an experimental problem.

The quoted extinction ratio is 1000:1 and the prism has a roughly square clear aperture 9 mm on a side. Because of the restricted aperture, the beam must always be stopped down to less than 9 mm in diameter when using the polarizer. The required distance to separate the polarization branches cleanly is also beam-diameter dependent,

$$D_p = \frac{w}{2\tan(\delta)}\left(\frac{1}{\cos(\delta)}+1\right) \cong \frac{w}{\tan(\delta)}, \tag{5}$$

where w is the beam diameter and δ is the separation angle, so that for a typical 2 mm beam, the required distance is 46 mm or more. The total available length between the chamber entrance aperture and the focusing optics is somewhat less than 250 mm, so a 5-

mm beam is about the maximum size that can be polarized. It is also desirable to exceed the minimum separation distance somewhat to ensure a pure linear polarization of the incident beam.

The polarizer also attenuates the beam (beyond the 50% expected from simply removing one polarization), since although MgF_2 has fairly low VUV absorption until about 130 nm, the path length is nearly 60 mm. Even slight absorption can be significant with such a thick optical element, so the polarizer is effectively limited to wavelengths of 150 nm and longer.

The two polarization branches, *s* and *p*, are selected simply by rotating the polarizer 90°, which is done manually in the current design.

d. The focusing system

The focusing system is mounted on the high vacuum side of the system because its stage motor must be operated outside of the "glow discharge" vacuum region (~0.1 – 0.001 Torr), at which some electronic components will not operate correctly and may be damaged if energized. The focusing system occupies a rather long tube on the nose of the chamber. This length accommodates the stage motor and also provides space for a polarizer, which requires a long distance to diverge the separated polarization components.

Several approaches to focusing, a particularly difficult and critical operation, have been tried. One approach is to scan a feature of small size relative to the smallest possible beam size. Usually, a feature less than 5 µm in extent is preferable. This allows fairly accurate direct measurement of the beam size by scanning the beam over the

feature (which effectively gives a convolution of the beam shape by a quasi-delta function).

Additionally, the feature can then be centered under the beam while the focus is adjusted. The scattering (or photoemission) signal from the feature will be proportional to the irradiance at the beam center, and this irradiance is maximized when the beam is focused. By this procedure then, we can acquire the focus simply by maximizing a scalar value.

Practical limitations to this centered beam approach though are that it can be difficult to find a small feature when the beam is not yet focused (or when background noise makes such small features impossible to distinguish) and that the converging lens and stage must be well centered and aligned. Misalignment will tend to cause the beam to drift in the X-Y plane, producing signal variations associated with not only the tightness of focus but also the relative position of the feature with respect to the beam center.

A slower but usually less restricted method is to scan features with sharp edges and analyze the maximum spatial frequencies contained in the scan. This is in effect how human observers normally focus on a visual scene, by changing the focus to maximize the sharpness of the image. Sharpness may be determined by autocorrelation of the image, Fourier analysis, or even by inspection (human vision is of course quite good at determining image sharpness for obvious reasons). The method is slower because the same region must be scanned multiple times to acquire a focus, but it is quite robust and

almost always manages eventually to find the best possible focus, even if the scene contains no distinguishable small features.

With a wide-spectrum system such as the HEUDI, the focus must be adjusted with each wavelength, which makes the focusing problem quite time consuming if it becomes necessary to repeat either of the above focusing procedures for each wavelength (the system has more than 100 effectively distinct possible wavelength settings). The preferred solution to this is to characterize the focal length change of the particular lenses in use and then move the stage to account for this change. The absolute stage position reading relative to distance between the sample and the stage varies depending on the experimental setup, but the changes in distance between wavelength foci do not. Therefore once a focus is acquired at wavelength A, we know to within a few percent how far the stage should move relatively to get a focus at wavelength B, from pregenerated focus formulas, FIG. 8.

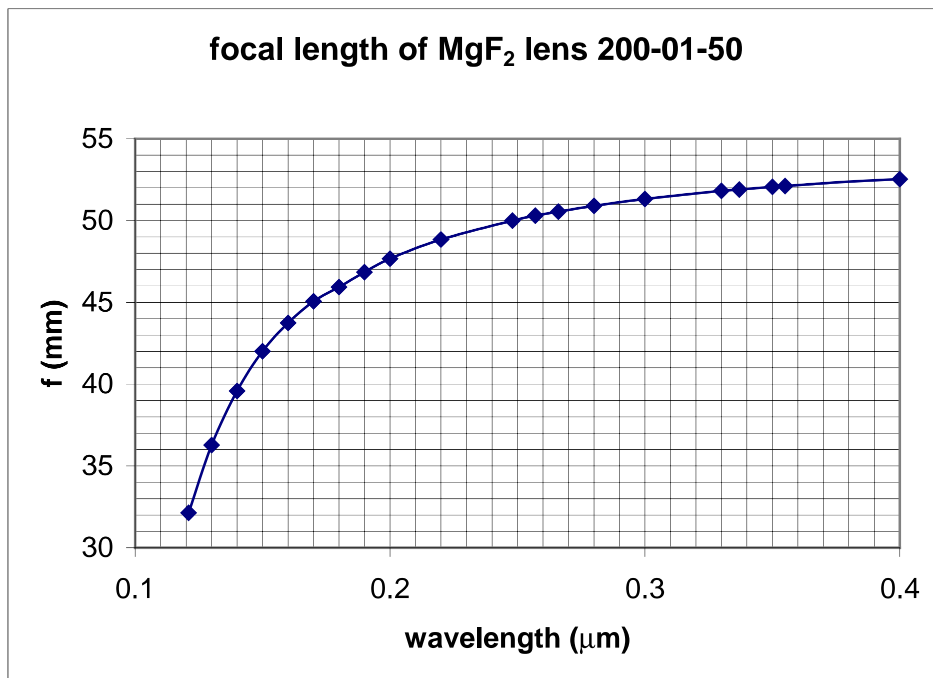

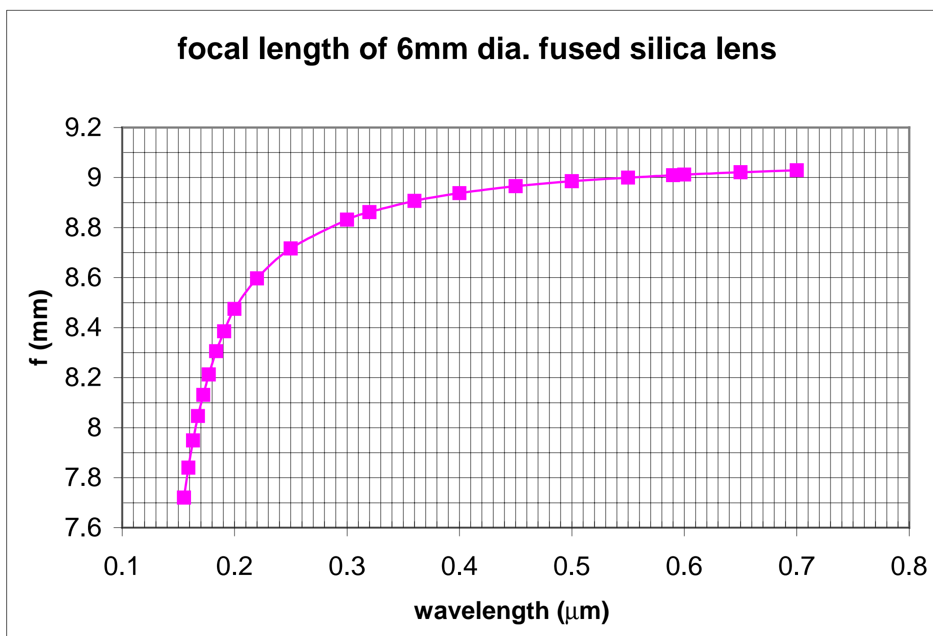

FIG. 8. Lens focal lengths (index data from Crystran Optics[42,43]).

The focal length dependence on wavelength also reveals the fortuitous fact that shorter wavelengths give shorter focal lengths and thus the power of the lens improves considerably in the DUV and VUV.

The fused silica lens shows some focal length variation as well, though not so dramatically. The effective focal length of the combined lens system (used in longer wavelength scattering experiments) has been calculated as well for this purpose.

Because of the short wavelengths, the width of the beam, and the limited availability of specialized optics in the VUV, the ultimate spot size tends to be limited most by demagnification power and then probably by aberrations or diffraction. While the diffraction-limited spot size decreases with decreasing focal length, the aberration-limited spot size generally decreases with increasing focal length. When the HEUDI system uses the longer working distances of the MgF_2, diffraction is more likely to be limit the size than aberration, but the primary limit is simply demagnification due to the weakness of the lens.

The distance from the beam entrance point to the sample is around 20 inches (~500 mm), varying a few inches depending on the stage Z-height. The MgF_2 lens has a nominal focal length of 50 mm (at 248 nm), with an actual range from 32 to 52 mm as in FIG. 8, but we shall use 40 mm for rough design calculations. Thus this lens should provide a total demagnification of 500/40=12.5 for imaging an aperture at the beam entrance point, given the collimated beam. The effective distance of the source after collimation appears to be around 4 m, so using the “lens maker’s equation”

$$\frac{1}{f} = \frac{1}{d_i} + \frac{1}{d_o}, \quad (6)$$

it is readily apparent that the source image and the beam entrance aperture come to a focus several millimeters away from each other, 3.1 mm apart with the 40 mm focal length. This makes the focusing somewhat complicated since it is sometimes not clear which object plane is in focus, but generally it is preferred to focus the aperture, which has less irradiance variation and a smaller spot size.

Of course, since the lens is translated to change the focus and the object planes are stationary, finding the actual lens position to achieve a focus involves a little more than the lens maker's equation. The exact expression turns out to be

$$\Delta l = \frac{d_o}{(d_o - f)}\left(f - \frac{d_0}{2} + \frac{1}{2}\sqrt{d_o^{\ 2} - 4f'(d_o - f)} \right). \tag{7}$$

The fused silica lens can increase the demagnification by approximately a factor of 5, to get a demagnification of about 60. With some of the smaller apertures and longer wavelengths, this might brush up against the diffraction limit, but diffraction is again unlikely to be an issue. Aberration is unlikely to come into play here as well, with a small aperture at the beam entrance, since the spherical aberration blur spot strongly increases with diameter.

If we do not use an aperture at the beam entrance, the full 20 mm monochromator output beam can be collected and focused by the 1-inch MgF_2 lens, providing maximum power throughput. In this case, we should consider the real divergence of the naturally imperfect collimated beam (or equivalently the finite effective source distance) to determine to the ultimate spot size. This is more easily measured than calculated, and the size comes out to a few hundred micrometers (FIG. 9), an effective demagnification of approximately 100. Such demagnification implies that the effective object distance is on

the order of 4 meters and the full-angle divergence is about 5 mrad, only somewhat larger than that for a low-quality laser, albeit with an enormous beam diameter. The product of these two quantities, divergence and beam diameter, is of course constrained by the source brightness, which clearly shows the advantage of laser sources for this application.

Not until we attempt to demagnify the full beam with the fused silica lens are we likely to run into diffraction or aberration spot size limits, the latter particularly likely given the large input beam diameter. In practice, that spot size does in fact seem to be limited by more than the total demagnification (expected to be on the order of 600) since it appears to be around 150 um.

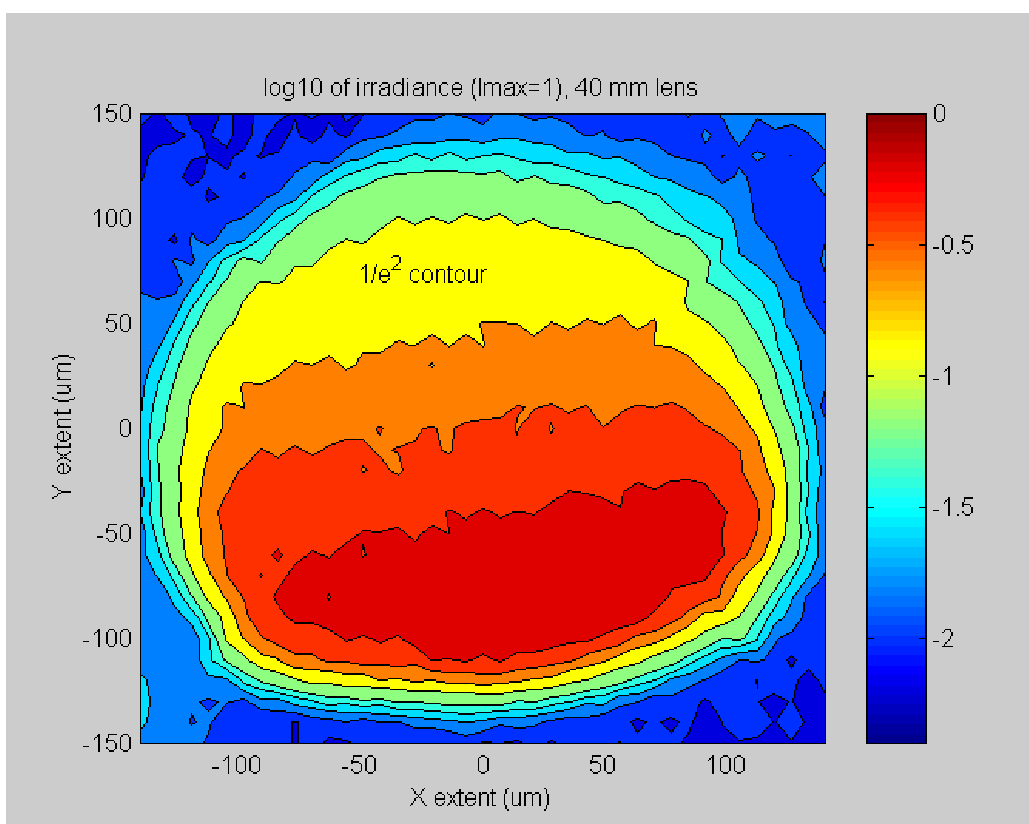

FIG. 9. 50-mm MgF_2 lens focal spot.

20 μm spot sizes (and usable power levels) should be achievable with the current optics, though this has not yet been demonstrated.

The longer working distances obviate many problems with mechanical interference between the focus and detector components often encountered in scattering measurements. This is especially useful for the photoemission experiments, in which the channeltron must be mounted close to the illumination spot between the converging lens and the sample.

To get smaller spot sizes, aberration-corrected refractive systems are available for wavelengths greater than 190 nm or a reflection objective might be used for shorter wavelengths. The latter component is particularly bulky however and has very short working distances, which would make its use in scattering measurements difficult. Reflection objectives have been used frequently by previous investigators, although observations of interference with photoemission signal by bulky short-working-distance focusing elements reported in Chapter IV would suggest that these should be used with care. Reflection objectives are also achromatic though, which would be an especially useful property in the photoemission mode.

Besides reflection objectives, previous scanning photoemission investigators have also used zone plate focusing elements, particularly for sub-100 nm experiments. The current work is the only example of the use of refractive focusing elements for VUV photoemission known to the author.

5. Interfacing electronics

The interfacing electronics transfer and process signals between the instrument and the control computer. The main signal input may be connected (by a BNC connector) to either the optical signal output or the electron signal output from the chamber. The data signal is then transferred from the selected feedthrough output port over a shielded 50 Ω coaxial cable to a Stanford Research SR250 Gated Integrator (GI). The GI integrates the data pulse over a programmable gate period, triggered by same pulse which fires the lamp. This allows a high degree of rejection of background noise. The flash duration and hence the data pulse width are approximately 5 μs in length, making the duty cycle around 1/1000 in normal 50 Hz operation.

The sensitivity (essentially gain) of the GI and the gate timing are selected manually on the front panel of the GI. The optimal settings differ somewhat depending on whether the optical detector or the electron detector output is used, although the timing is similar.

The GI output signal is passed to the Intelligent Instrumentation PCI-20428-1A interface board where a 12-bit analog-digital converter (ADC) digitizes the signal. The ADC has software-selectable gains of 100, 10 or 1, allowing software-controlled dynamic range of about 5½ orders of magnitude. Signal variation of greater magnitude must be compensated for manually at the GI, but variation over a particular sample does not normally exceed this range. Since the GI allows a factor of 200 between its minimum and maximum sensitivities, the electronics can thus be adjusted to accommodate the entire 7½-order dynamic range of the PMT.

The interface board also provides 8 bits of digital input and 8 bits of digital output. The highest output bit enables (high) and disables (low) the lamp pulse, so that the data acquisition trigger may be issued without firing the lamp.

The lamp trigger pulse is generated by a 555-compatible clock chip, which ensures that the pulse has the minimum 20 μs width required to trigger the lamp. This long pulse is triggered by a counter output from the data acquisition board, which also acts as the GI trigger. All the buffering, gating, and external timing functions for the interface are provided by a small interfacing unit that shares the Nuclear Instrumentation Module (NIM) bin with the GI module.

Four bits of the digital input bus are used to receive real-time signals from the motor controllers (using two bits apiece) and four bits of the digital output bus are likewise used to carry real-time signals from the PC to the controllers. Each controller has its own RS-232 serial line to the PC which allows bidirectional communication for uploading code to the controllers and initiating motor control procedures.

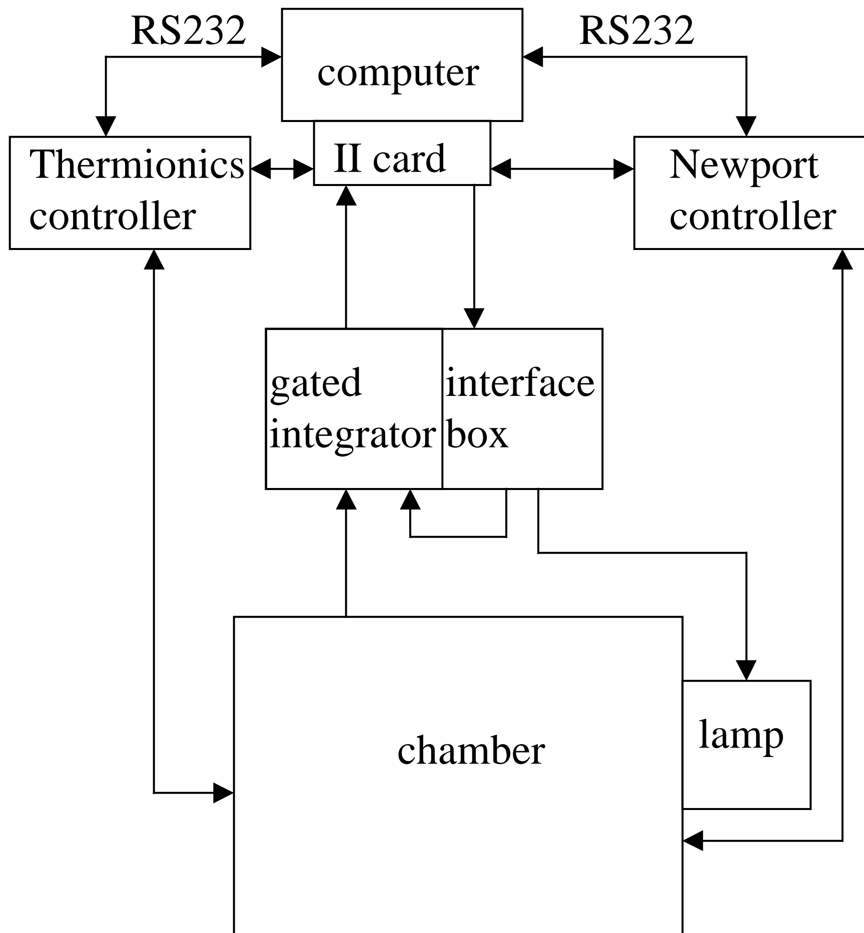

FIG. 10. Interfacing system.

C. Software

The HEUDI control software is designed to achieve two main goals, to navigate the stage easily to surface features of interest and to collect data on those surface features. The code is written in Microsoft Visual C++ 5.0 (easily portable to later versions) and uses the Microsoft Foundation Classes to provide a time-tested and widely used graphical user interface (GUI) framework. Hardware access is supported by a commercially available application program interface (API) provided by the vendor of the interface

card. The code runs under most Win32-based operating systems but is primarily intended for use with Windows NT.

The application design uses the Document-View model, supporting two different but related document types, angle scan and X-Y scan documents. The view windows associated with these two document types display data in graphical formats appropriate to the scan type (FIG. 11).

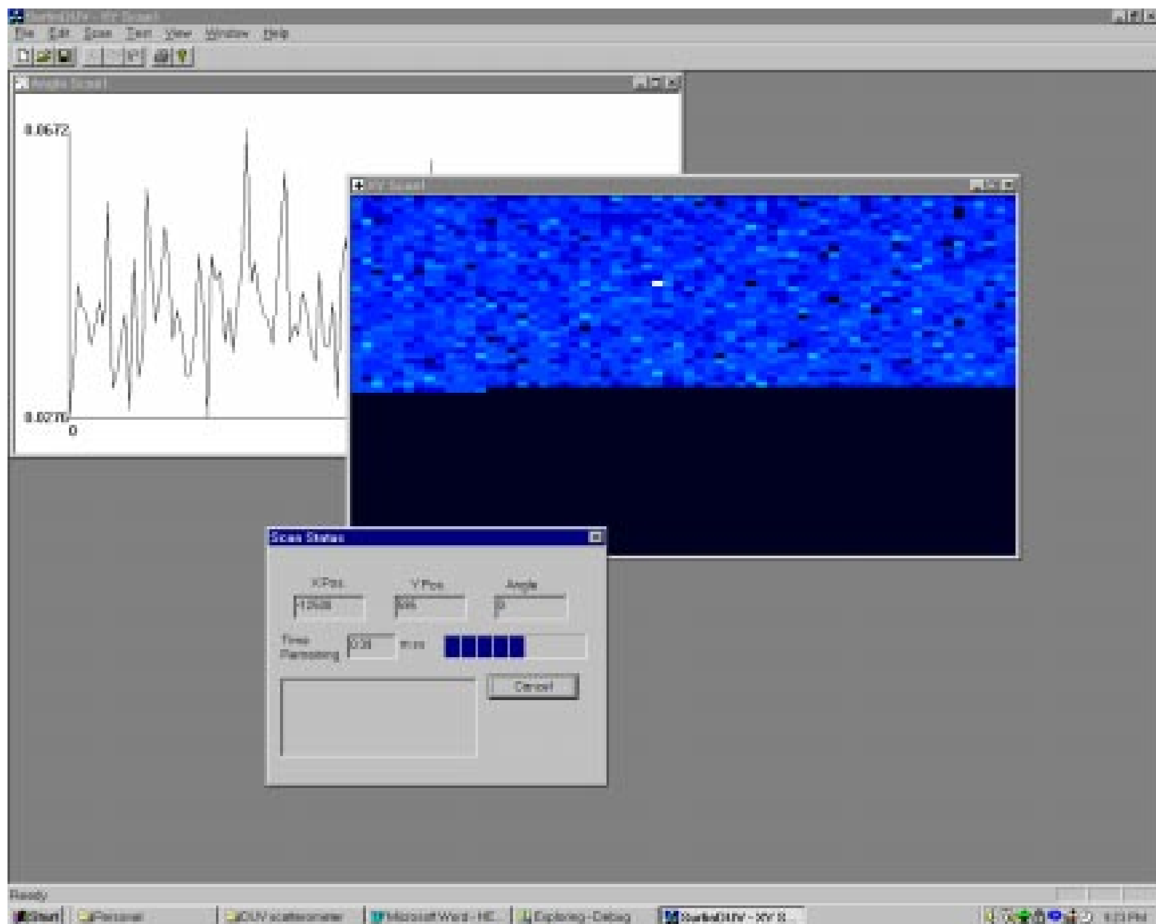

FIG. 11. Screen shot of control software (electronic noise).

The X-Y scan document supports navigation and collects data for fixed optical detector angles over the sample surface. This scan type is also used for photoemission data collection.

Normally, data collection will begin with an X-Y scan. For searching large areas, a high-speed scan may be performed, in which hardware-based timing is used to pace data collection while the stage motors execute a long constant-velocity translation. For smaller areas, a slower stepping-mode X-Y scan may also be performed, in which the motors stop at each data collection position. This stepping mode has greater positioning accuracy.

If a point of interest is located during the X-Y scan, that point may be selected for an angle scan simply by double clicking the data map of that point in the window, whereupon a new angle scan document is created. Rectangular regions of an X-Y scan may also be selected for higher-resolution scanning. Multiple document interface (MDI) support allows a large number of these data sets to be open at a given time, which greatly facilitates experiments.

D. Experimental setup

Scattering measurements are conducted in plane, unless otherwise specified. The PMT active area is circular and 4.5 mm in radius, and the PMT is usually positioned at a minimum distance of 7 cm from the focal point, and is typically farther away, so the detector only extends a few degrees out of plane, subtending less than 4 degrees of arc. At maximum distance, the detector subtends about 2 degrees, which sets the angular

resolution limit. Angle scans are typically made with 1 or ½ degree motor position resolution.

The coordinate system used is illustrated in FIG. 12. When the detector coincides with the incident beam, it reads at 90°, while 0° is the direction of the chamber access door.

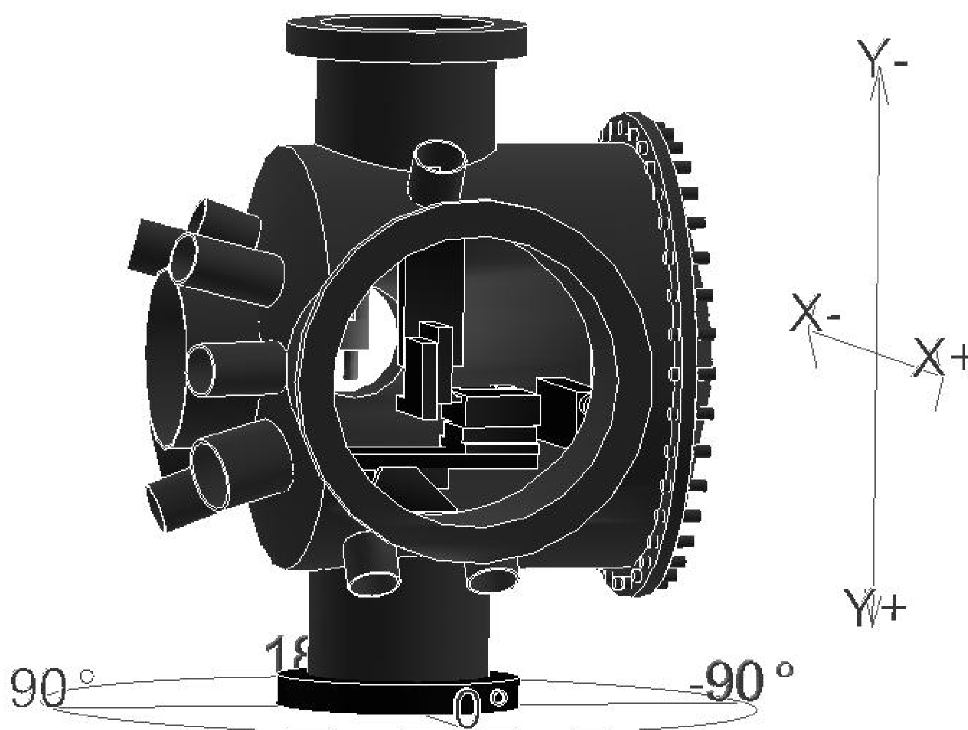

FIG. 12. System coordinates.

Stage rotation is reported as the angle of the stage normal vector, towards the incident beam, so that a 90° stage angle indicates normal incidence, and 0° indicates edge-on incidence. The stage is always rotated so that it faces toward the chamber access

door for angles less than 90°. Thus since this is a reflection geometry, angular scattering measurements may be conducted at angles 0° to 180° for normal incidence (stage angle 90°), -45° to 135° for 45° incidence (stage angle 45°), and -90° to 90° for edge-on incidence (stage angle 0°). Stage angle corresponds therefore to elevation angle of the beam in the incident plane. Not all of these angles are useful, due to physical obstructions such as the focusing optics, but they are the schematically available angles.

The X-Y position of features relative to the stage is reported and mapped with the Y axis vertical and the X axis horizontal. High is more negative, low is more positive; left is more negative, right is more positive (following the more frequently encountered convention in computer graphics). SurfinDUV maps are oriented as if the observer were standing in front of the stage, in the intuitive perspective.

The channeltron is stationary with respect to the sample (being attached to the rotation stage), but the tilt mount and the fixed-attitude 8" wafer mount place the channeltron aperture at different positions.

The focusing system (FIG. 13) consists of a primary focusing lens, usually a 1" diameter MgF_2 biconvex lens with 50 mm nominal focal length and an optional secondary focusing lens approximately 1" from the primary lens. The secondary lens, if present, is typically a smaller more powerful lens, usually a 6 mm diameter, 9 mm focal length plano-convex fused silica lens.

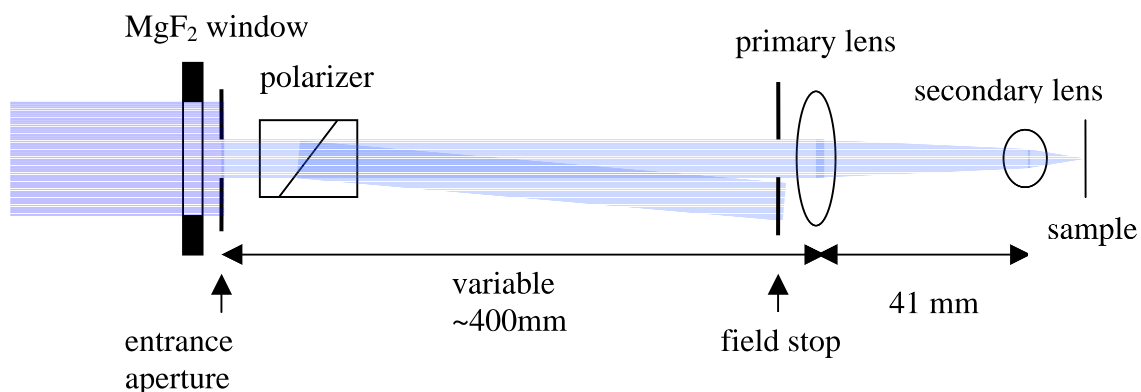

FIG. 13. General optical configuration and focusing system.

The primary focusing lens mount can be fitted with three sizes of apertures (field stops), 2 mm, 1 mm, and 0.5 mm. Without this aperture, the collimated input beam is approximately 20 mm in diameter. With the 0.5 mm aperture and the 6 mm diameter secondary lens (*f*=9 mm), a spot size of approximately 65 μm has been achieved.

Several other optical configurations have been used, most successfully one with an aperture a few millimeters in diameter placed just after the window between the medium and high-vacuum sections. This decreases the effective beam width going into the focusing lens and can achieve $1/e^2$ spot sizes of around 200 μm with the 50 mm lens. This arrangement generally seems to have somewhat better throughput than demagnifying the whole beam and using a field stop. This allows a spot size of around 40 μm or less with the 9 mm lens (since the focal length is around 5 times shorter with the secondary lens), or somewhat larger with the combination of the two. The spot is also not really Gaussian, so the commonly used $1/e^2$ spot size parameter only imperfectly captures the influence on scanning resolution though. The beam energy is concentrated

strongly in the lower portion of the beam, so that the 50 mm lens spot tends to be closer to 200 μm wide and 80 μm high. The larger beam is actually the image of the circular lamp aperture, which is filled in with stray light reflected inside the flashlamp, while the bright core is the image of the flashlamp arc itself.

The diffraction limit for spot size is fairly easy to characterize, using the Airy limit since the beam overfills the apertures,[44]

$$d_0 = 2.44\frac{\lambda f}{D}. \tag{8}$$

For the 50 mm lens (f=48 mm, λ=0.2 μm) and a 1 mm aperture, this is about 23 μm. For the 9 mm lens (f=9 mm, λ=0.2 μm) and the same aperture it is about 4 μm. Thus the spot sizes achieved are fairly far from the diffraction limit with either lens.

An aberration limit to the minimum spot size could also apply with the simple uncorrected spherical lenses used here, but generally the aberration limit will not apply either.

The 9 mm lens alone yields a smaller spot size than the 50 mm and 9 mm lenses in combination of course, since the effective focal length of this compound lens system with a separation of d is given by[45]

$$\frac{1}{f} = \frac{1}{f_1} + \frac{1}{f_2} - \frac{d}{f_2 f_1}, \tag{9}$$

by which it appears that this gives an effective focal length of around 31 mm. Obviously this would seem to be an inefficient use of the 9 mm lens in terms of achieving a small focal length. However the purpose of the compound lens is to provide more focusing power for a large beam. High-power MgF_2 lenses are hard to obtain and quite

expensive, while fused silica lenses do not have much transparency below 200 nm. A 25 mm diameter fused silica lens of similar focal length is typically more than 7 mm thick, while the fused silica lens with 6 mm diameter, and 9 mm focal length is only 2.5 mm thick, so this lens combination provides greater focusing power for a large beam without excessive absorption, which is well suited for experiments requiring high throughput with less critical spot-size demands. It also allows the flexibility of an intermediate step in the working-distance/converging power tradeoff, which is useful in some experimental situations.

III. DUV SCATTERING MEASUREMENTS

Scattering measurements constitute a major *raison d'être* for the HEUDI system. Scatterometry at visible wavelengths is a well developed field,[10] however little work has been done in scattering measurements in the deep ultraviolet portion of the spectrum and even less is readily found in the literature. As discussed earlier, the primary motivation for these measurements is for the predicted potential benefits in defect detection. Secondarily, scattering is also an important factor in optical design, and with DUV optics playing an ever-larger role in photolithography, measurements of scattering effects at these wavelengths are of interest in areas beyond surface inspection.[8]

Scattering in a reflection geometry may be simply described as a deviation from simple specular reflection so it is often described as a distribution of reflectance over the angles θ and φ in a spherical coordinate system centered at the point where the illuminating beam falls on the sample. This distribution function is termed the bidirectional reflectance distribution function (BRDF), a concept introduced in the 1960s-1970s, principally by the tireless advocacy of Nicodemus.[46,47] Another way to view BRDF is as a linear modulation of the reflectance of a perfect Lambertian surface, one which scatters power evenly into all solid angles, which has a constant BRDF = 1. In contrast, the BRDF of a perfect specular reflector has the form of a unit-area delta function.

BRDF is defined as[10]

$$BRDF(\theta,\varphi) \equiv \frac{d^2 P_S(\theta,\varphi) / dA_S d\Omega_S}{dP_I / dA_I}, \qquad (10)$$

where $dP^2_s/dA_s d\Omega_s$ is the differential radiance of the reflected (or scattered) light and dP_I/dA_I is the differential irradiance of the incident beam. A finite-area estimate of the BRDF can be calculated as

$$BRDF(\theta,\varphi) = \frac{P_D(\theta,\varphi)}{P_I} \frac{1}{\Omega_D \cos(\theta_s)}, \tag{11}$$

where P_D is the power detected, P_I is the incident power, θ_S is the scattering angle, and Ω_D is the solid angle subtended by the detector. We should note that a finite spot size (as well as a finite detector extent) allows only an approximation of the true BRDF. In fact, finite spot size introduces a certain angular frequency limitation on the calculated BRDF estimate, essentially requiring us to keep in mind that in some cases, our measured BRDF will show dependence on spot size.

The definition of BRDF also assumes a collimated incident beam rather than a convergent incident beam, which is the norm in most scatterometric systems, but this seldom presents a significant problem.

A number of alternative forms for describing light scattering have been used, particularly for scattering by surfaces. For one, it is not uncommon to drop the cosine term from the BRDF definition, which is then called “cosine-corrected BRDF,” “BSDF” (bidirectional scattering distribution function), or even just “BRDF.” This form tends to be preferred for generalized or transmissive scattering problems, but it also removes the simple relationship between the ideal Lambertian scattering profile and the BRDF.

The second alternative that bears mentioning for the present work is the differential scattering cross-section. Differential (with respect to solid angle) scattering cross-section (DSC) is defined as

$$\frac{d\sigma(\theta,\varphi)}{d\Omega} \equiv \frac{dP_s(\theta,\varphi)/d\Omega_s}{P_I/A_I}, \tag{12}$$

using the scattered radiant intensity rather than the scattered radiance, as with BRDF, and replacing the incident differential irradiance with power delivered into a finite probe area (which is conceptually not quite the same thing as irradiance).

If a localized scatterer is centered under a Gaussian beam (at the point of maximum incident irradiance), we can calculate the finite-difference estimate of this from[48]

$$\frac{d\sigma(\theta,\varphi)}{d\Omega} = \frac{A_I P_D(\theta,\varphi)}{2P_I\,\Omega_D}. \tag{13}$$

This relates to measured BRDF by the expression

$$\frac{d\sigma(\theta,\varphi)}{d\Omega} = BRDF(\theta,\varphi)\cdot 0.5A_I\cos(\theta_s), \tag{14}$$

where A_I is the area of the spot. This assumes also that the scatterer is small compared to the scale of variation of the beam irradiance. The 0.5 coefficient in Eqn. 13 arises because the maximum irradiance is twice the mean irradiance for a Gaussian spot defined with the spot boundary at the $1/e^2$ (that is, where the beam irradiance is $1/e^2$ the irradiance at the central maximum). Note that this relation only holds necessarily for Gaussian beams. The HEUDI spot is not quite Gaussian, though the computed irradiance relation

for the beam profile is typically close to the Gaussian value, 0.43 for the case illustrated in FIG. 9, which should be taken is the default value for the HEUDI system.

The inclusion of the spot size information (and thus irradiance information) makes DSC somewhat more attractive for reporting scattering by single small (relative to the spot size) localized features, because the BRDF of such features is spot-size dependent while the DSC is not. However, the common literature convention of reporting the BRDF is followed herein, even for localized scatterers.

A. Measurement and calculation of BRDF

The discussion of BRDF measurement should begin with the reminder that BRDF, as a differential quantity, can never be measured directly in truth and can only be estimated from observing sufficiently small finite differences. The HEUDI UV detector moves through angular space and measures power incident over the detector active area at certain discrete points in the sphere of angular space, which is centered on the point where the incident beam strikes the sample. The output of this detector is observed as a voltage, presenting the chief calibration task associated with the instrument, associating voltage levels with received power levels, and particularly the power (or irradiance and spot size) of the incident beam. We can note that if the detection electronics give a linear relationship between detector power and voltage (usually the case, provided the PMT is not being driven too hard), then we may simply replace the power terms with voltages, if we measure the incident beam power on the same scale,

$$BRDF = \frac{V_D}{V_I}\frac{1}{\Omega_D}. \tag{15}$$

This approach allows us to measure BRDF without having to calibrate the system to absolute power, which can often be very challenging.

Unfortunately, limitations of the electronics make this procedure difficult. The main obstacle is that the incident beam power is often six decades or more greater than the scattered power, so the response of the sensitively tuned electronics used to measure extremely low scattering levels is typically saturated by the full brunt of the focused incident beam. This problem is typically solved by attenuating the incident beam in a quantifiable way and then multiplying the resulting voltage reading by the attenuation factor. The particular scheme found most suitable for the HEUDI system with the PMT detector is to measure relative wavelength response of the system and then to tune the monochromator to low-responsivity wavelengths for the incident beam measurement.

Measuring the wavelength response is fairly simple, although it must be performed for several separate configurations. The incident beam for this experiment was fed through a small aperture (a few mm in diameter) in the collimated beam path, just in front of the focusing lens. The much larger PMT active area can be placed to subsume this small beam entirely by rotating the PMT to face outward from detector's revolutionary axis. Even this small aperture allowed enough light to saturate the PMT at peak-response wavelengths though, so the monochromator slits were also used to develop three series of overlapping measurements with different slit openings and integrator sensitivity settings. These three series of data were then pieced together to form a wide-spectrum curve with large dynamic range, (FIG. 14).

It should be noted that the maximum atmospheric pressure system response for the present source (Xe flash lamp) and detector (Hamamatsu R7311 PMT) lies in the 190 nm – 230 nm range, which was expected in the system design. For low pressures, the vacuum ultraviolet response stays sufficiently high for sensitive scattering measurements down to around 160 nm. The visible light response is quite weak but can still be useful for the measurement of strong scattering in the visible range, which is an unexpected advantage of the system for performing widely multispectral measurements. The 300 – 400 nm range is useless for most purposes.

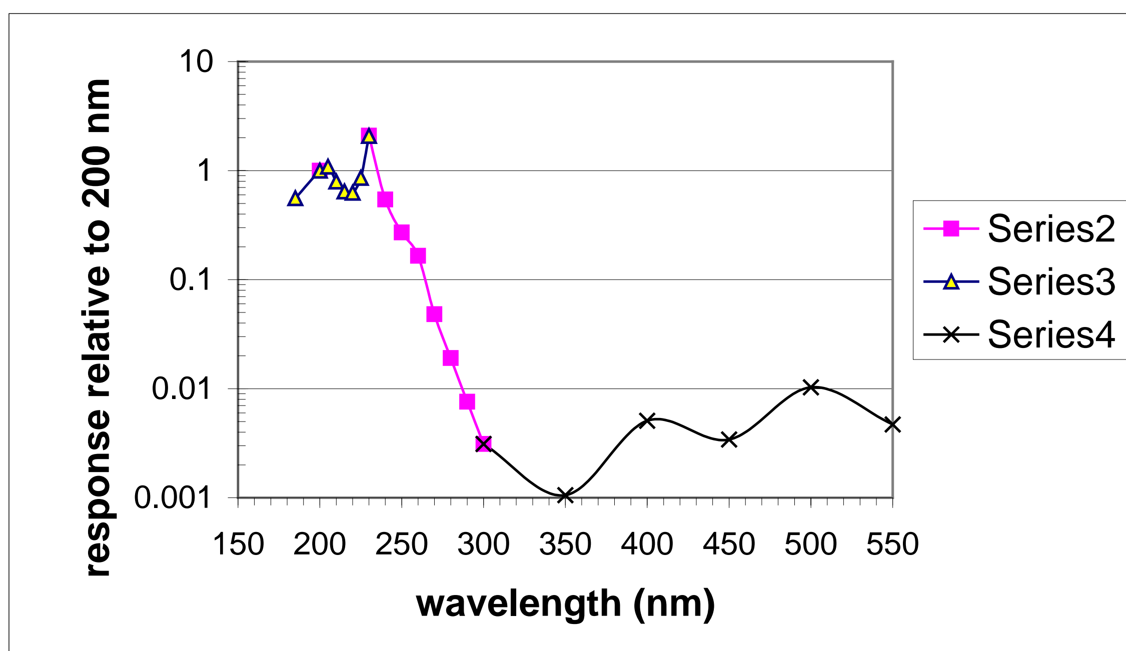

FIG. 14. Relative wavelength response at atmospheric pressure with Hamamatsu R7311 PMT and Xe flash lamp.

A similar curve was developed for the vacuum environment (FIG. 15), with special attention to the shorter wavelengths.

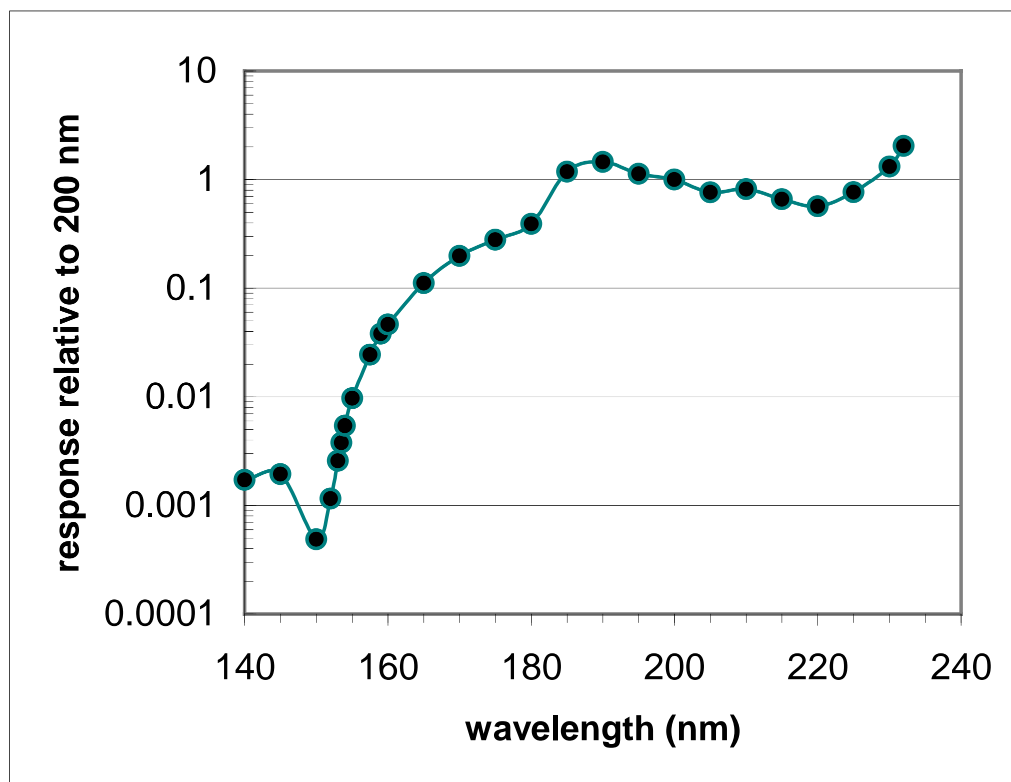

FIG. 15. PMT response curve at high vacuum.

The system response was also measured with a calibrated reference detector. Since the reference detector comes with documented calibration curves, this latter data set may be used to determine the spectral power output of the optical train (FIG. 16), which is also necessary in the photoemission experiments to estimate photoemission yield (Chapter IV).

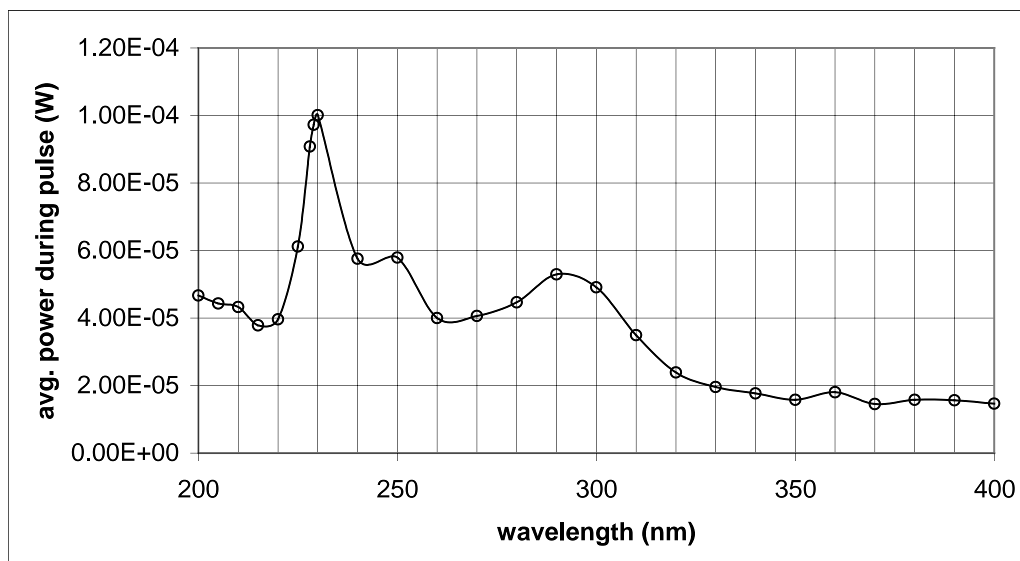

FIG. 16. Full-throughput avg. power during pulse - MgF_2 lens, atmospheric pressure, 3 nm bandwidth.

This part of the calibration may be achieved with relatively low random error, since we can fairly easily take as many data points as necessary to reduce random error due to noise in the signal.

As described earlier, if we do need to relate the BRDF to scattering cross-section, we need to determine local irradiance of the incident beam on the scatterer. The incident beam spot size, typically reported in terms of the $1/e^2$ radius, ω_0, is a convenient parameter for Gaussian beams, since it (or at least the major and minor beam diameters for elliptical beams - equivalently the spot size and some parameter of ellipticity) relates in a known way to the irradiance at the central maximum of the beam. Unfortunately, as described earlier, the HEUDI spot deviates somewhat from Gaussianity, due mostly to coma from the collimation optics, which consist of off-axis reflective elements.

This deviation is ameliorated for small apertures, but it still demands consideration. The beam profile may be measured several ways, but the most convenient is to profile it with a small localized scatterer, such as a particle. For a particle much smaller than the beam itself, the X-Y scan of the region around the particle will produce a signature that reflects the beam irradiance profile. Generally, the X-Y scan of a localized scatterer is a convolution of the beam profile and the spatially varying scattering cross-section of the scatterer. In the case of the very small particle, the particle acts as a sharp impulse that convolves the beam profile, and thus the X-Y scan map is simply the beam profile scaled by a constant. We can then integrate this profile to determine the total power in the profile and relate that to the measured incident beam power, which then can be used to determine the beam's absolute irradiance profile. When particles are subsequently measured, the X-Y stage is positioned at the scattering signal maximum for the scanned profile, which point has a calculable irradiance.

B. Unpatterned silicon sample

The sample is a 2-inch single-side polished CZ-grown <100> silicon wafer purchased from Virginia Semiconductor (FIG. 17), with a suspension of 25.09 ± 0.12 μm polystyrene latex spheres from Duke Scientific deposited on the surface. Attempts were made to deposit 40 nm spheres, but the high surfactant levels required to keep such small particles from clumping will require more work on deposition methods.

The deposition of the 25 μm particles did leave some surfactant residue, but not in sufficient levels to interfere with measurement of scattering from the larger spheres.

The focal spot size for the experiment was fairly large at approximately 150 µm, although this can be reduced considerably in future measurements with better lenses. Scans were conducted at 45° incidence with incoherent unpolarized 200 nm illumination (3.4 nm bandwidth).

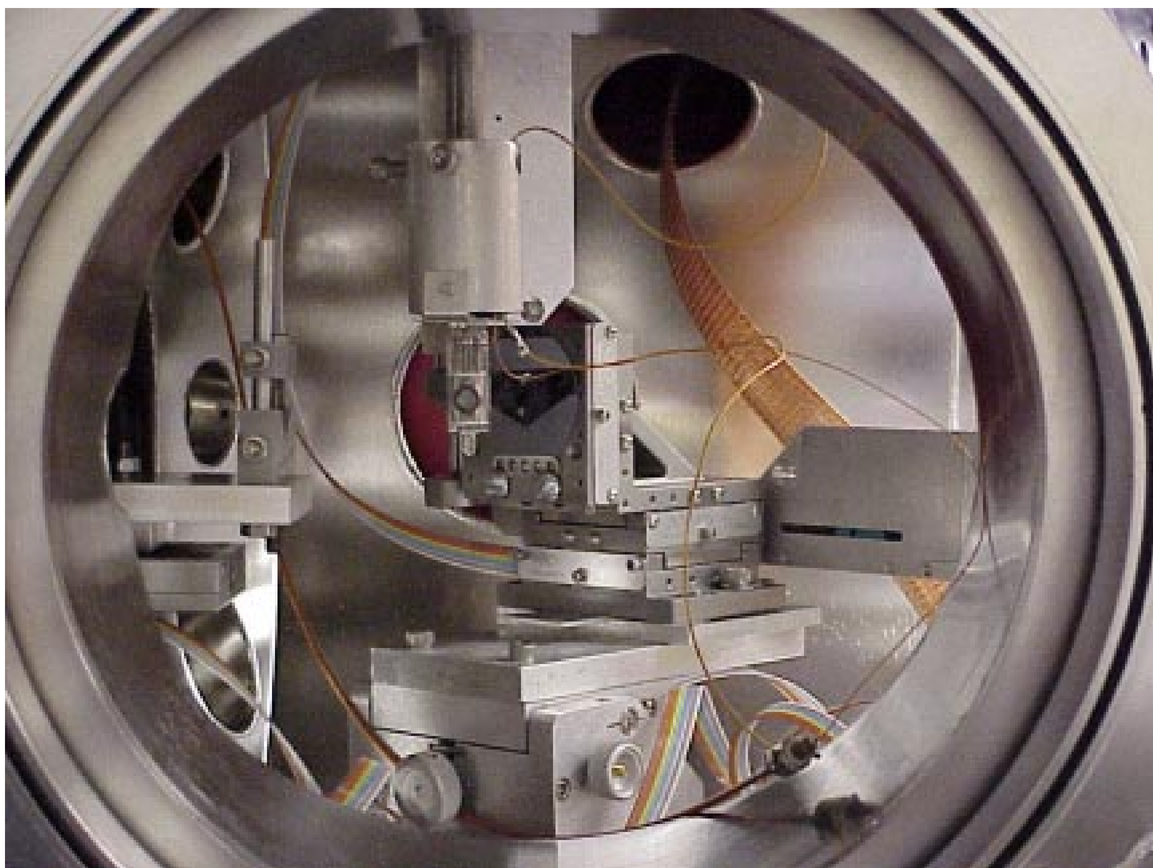

FIG. 17. Sample mounted in chamber (PMT tube has been rotated to face the camera).

Initial low-resolution scans with 500 µm spot size and 550 nm illumination (which allows easy visual determination of the spot position) were conducted to locate deposited particles (FIG. 18).

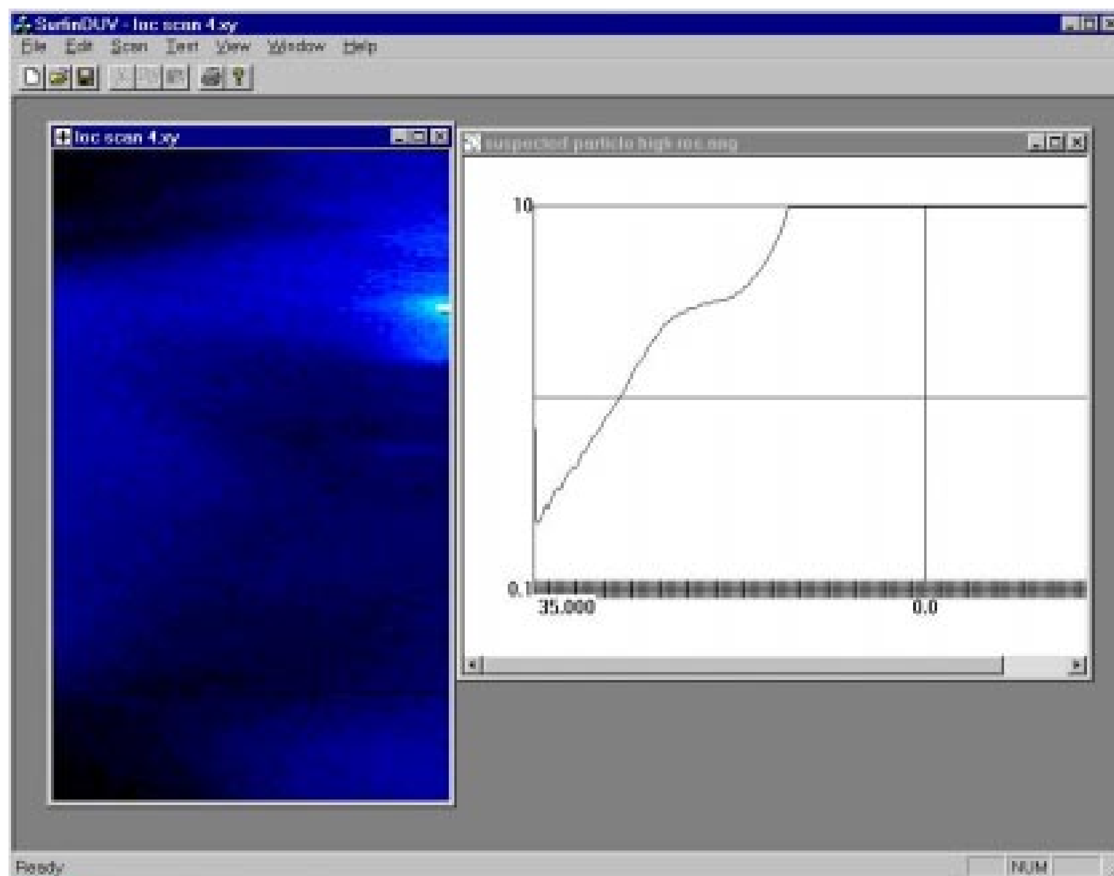

FIG. 18. Initial 550 nm large spot scan to locate deposition region (bright spot at upper right).

Once candidate regions were found, the spot size was reduced and the system dialed down to the 200 nm wavelength. Preliminary angle scans were performed to determine good detector angles for particle detection against scattering from the surfactant residue. Scans of the candidate regions then revealed individual particles and clusters, as well as a few broad bright areas which were areas of high surfactant deposition or particle “rafts”. 1-degree resolution angle scans were then performed on

areas tentatively termed “particle 1” (a very bright localized feature, undoubtedly a cluster) and “particle 2.” “Particle 2” is believed to be a single 25 μm particle, on the basis that nearly identical profiles were found repeatedly and that these were the smallest particle-like signatures in the deposition area. Microscopic examination of the region confirmed the presence of single particles, although the precise particle could not be relocated. FIG. 19 shows large-scale and close-up maps of this area under the 200 μm spot/200 nm illumination configuration.

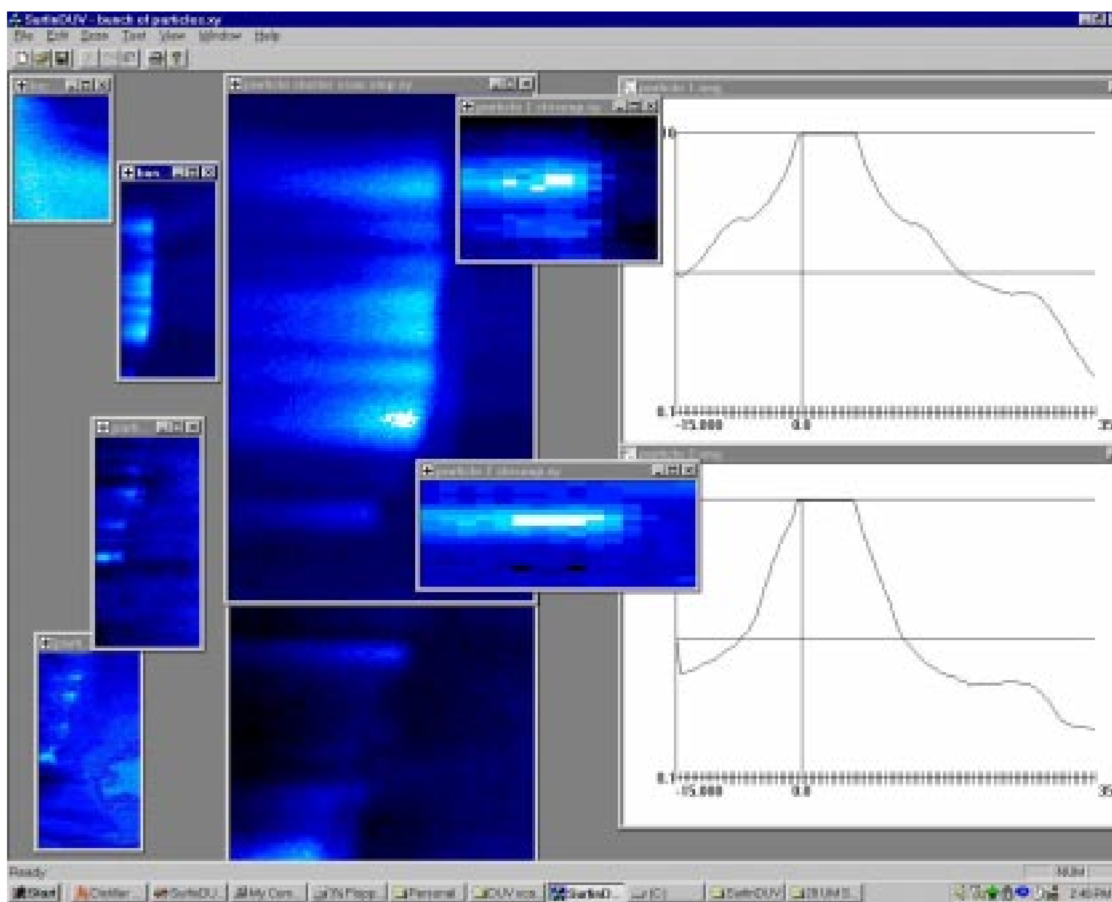

FIG. 19. HEUDI control software screen shot. 200 nm wavelength scans with 200 μm spot size.

Several peculiarities of the above scattering map merit comment. First, the "streakiness" of the localized structures is a result of elongation of the incident beam by the 45° angle of incidence and the somewhat comatic nature of the beam profile. This coma results from off-axis reflective optics in the monochromator and collimator and has been considerably reduced in later experiments. The second peculiarity is the tendency of the clusters and particles to lie along a curved path on the wafer surface. This arrangement is simply the result of the particles being deposited preferentially near the

edge of the solution droplet. The curvature of the round edge of the watermark is discernable.

After these data were acquired, it was necessary to measure the incident light to express the measurements in terms of BRDF via the previously described procedure. Using the relative response curve and incident beam measurements at 6 different low-response wavelengths, the incident beam power was determined to have an equivalent voltage of 4.32 V.

Using this calibration data, the BRDFs are plotted in FIG. 20.

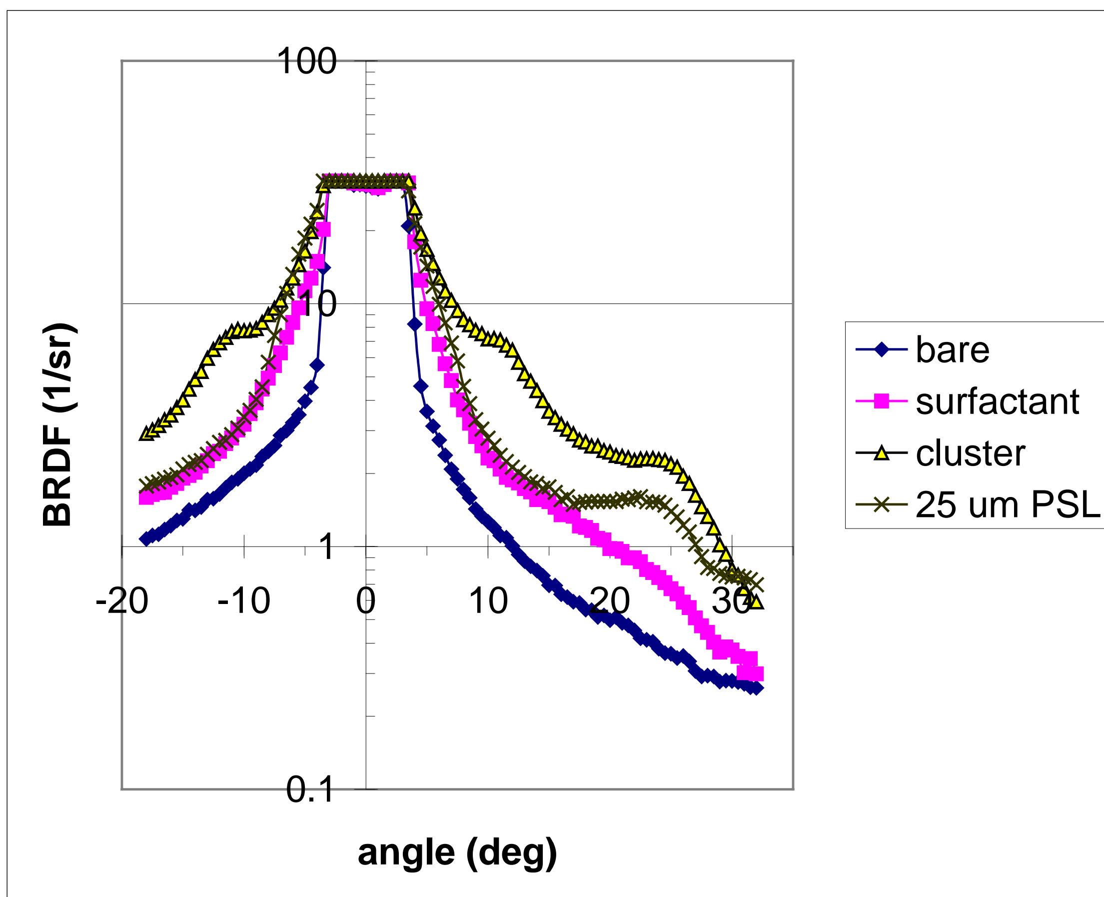

FIG. 20. BRDFs of sample features at 200 nm wavelength. Bare silicon substrate, 45° incidence angle, spot size approximately 200 μm. Specular beam at 0°.

It may be noted that the origins of these plots are shifted slightly from those in the screen shots. The relative angle indicator for the detector positioning system was a few degrees off from the beam axis, so this was corrected in the BRDF plots.

The curves show a clear scattering signature for the particle (certainly not unexpected for this size), contrasting it against the bare silicon surface, the surfactant covered surface (a side effect of the particle deposition), and a particle cluster.

The surfactant layer added a significant amount of background scatter in excess of that from the bare surface, which should be taken into account when considering the data. The large size of the beam contributes to the comparatively strong surface-originated background in these particular measurements. A 20 μm spot would be expected to give particle and cluster signatures that exceed the surfactant and bare surface backgrounds by a factor of 100 more. Some background, particularly in the angular neighborhood of the specular reflection, is also probably the result of Rayleigh scattering by the ambient atmosphere, which is quite strong at such short wavelengths. This effect can be attenuated at vacuum.

Some parts of the deposition area also featured “rafts” of closely packed particles, which gave a flat, nearly Lambertian BRDF. Such a scattering signature is often encountered with closely packed arrays of micro-scale spheroids such as bacteria colonies.

The cluster BRDF is, not surprisingly, both stronger than and qualitatively different from the single particle signature.

The greatest source of absolute inaccuracy in the foregoing measurements probably lies in the non-Gaussianity of the beam shape in early experiments and uncertainty in the detector area, on the order of about 10%. The total absolute inaccuracy is estimated to be in the 30 - 40% range. Random error, as should be apparent from the smoothness of the curves, was quite small, due to the high power levels and the fact that the sample sizes were adjusted upward until the random error in the signal means had dropped to insignificant levels. Unfortunately, a defect in the software that went

undiscovered until after the completion of these measurements prevents exact specification of the confidence interval, but a large estimate would be 5% of the mean for the data presented.

C. 700 nm PSL sample

While the early 25 mm PSL sample measurements were unsatisfactory in many respects, particularly in that the particle size is too large to allow numerical scattering computations with current methods, later experiments with smaller particles have had more success.

An 8-inch Si wafer was obtained from Brumley South, Inc., with 700 nm diameter standard PSL spheres from Duke Scientific deposited on half of the surface. This half-wafer deposition allows for more certain identification of the particles. For these experiments, the spot size was measured to be 100 μm ± 10 μm. The sample was rotated in the 8-inch wafer mount to place the deposition region boundary under the scanning field of the instrument, with the boundary line tilted to about 45° from the horizontal. FIG. 21 shows a scan of this area, with the bare region in the lower left corner.

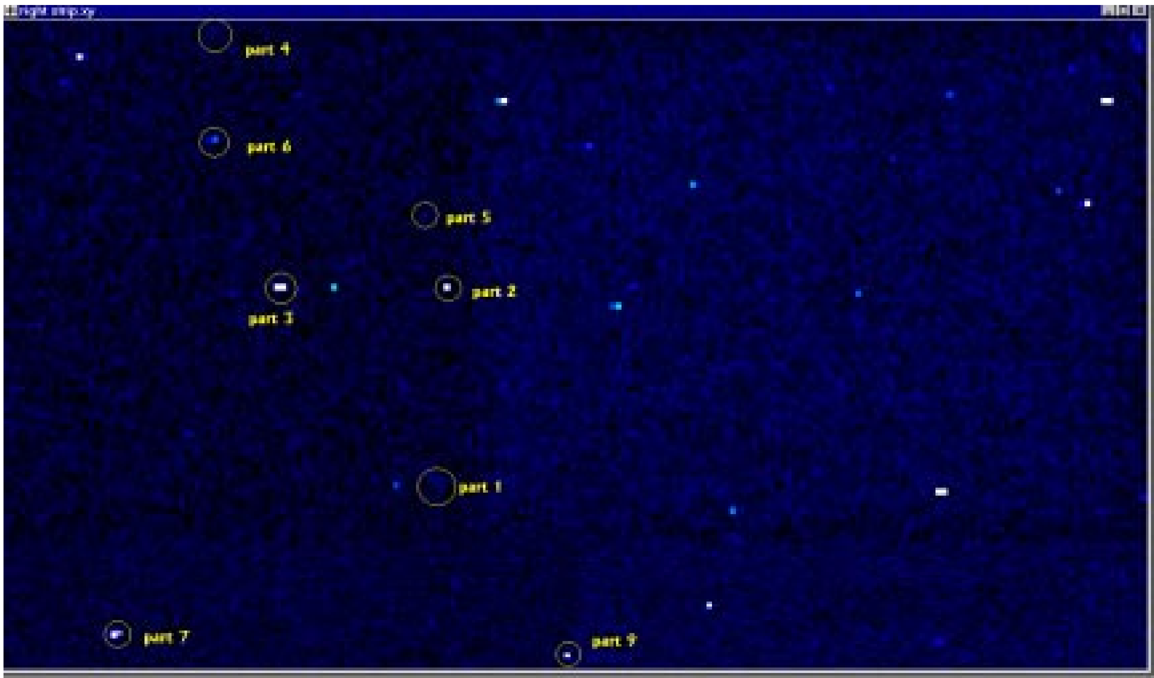

FIG. 21. 20 × 10 mm map of deposition boundary area, 230 nm unpolarized light at 40° incidence, scan angle 30°, spot size 100 μm.

The particles are specified by the manufacturer (from knowledge of the deposition conditions and an independent visible wavelength scan) to have a deposition density of 0.23 mm^{-2} or approximately 34 ± 11 (95% confidence) expected particles in the 150 mm^2 area of the scanned deposition region (about 50 mm^2 of the scan is in the undeposited region). The powers of the particle signals vary somewhat, partly due to the random position of the particles with respect to the discrete scan steps. Scanning the particles individually at higher resolution, some variation is still seen, but scattering signals even for standard particles are also known to vary significantly due to size variation and (probably) variations in the adhesion of the particles to the surface.

FIG. 22 shows angle scans for the particles circled in FIG. 21, which are generated by subtracting the local background scans from the particle scans. This plot is most useful for discerning the general similarities of the particles, due to the number of superimposed plots, but this is a necessary step to ensure that contaminant particles are not being measured.

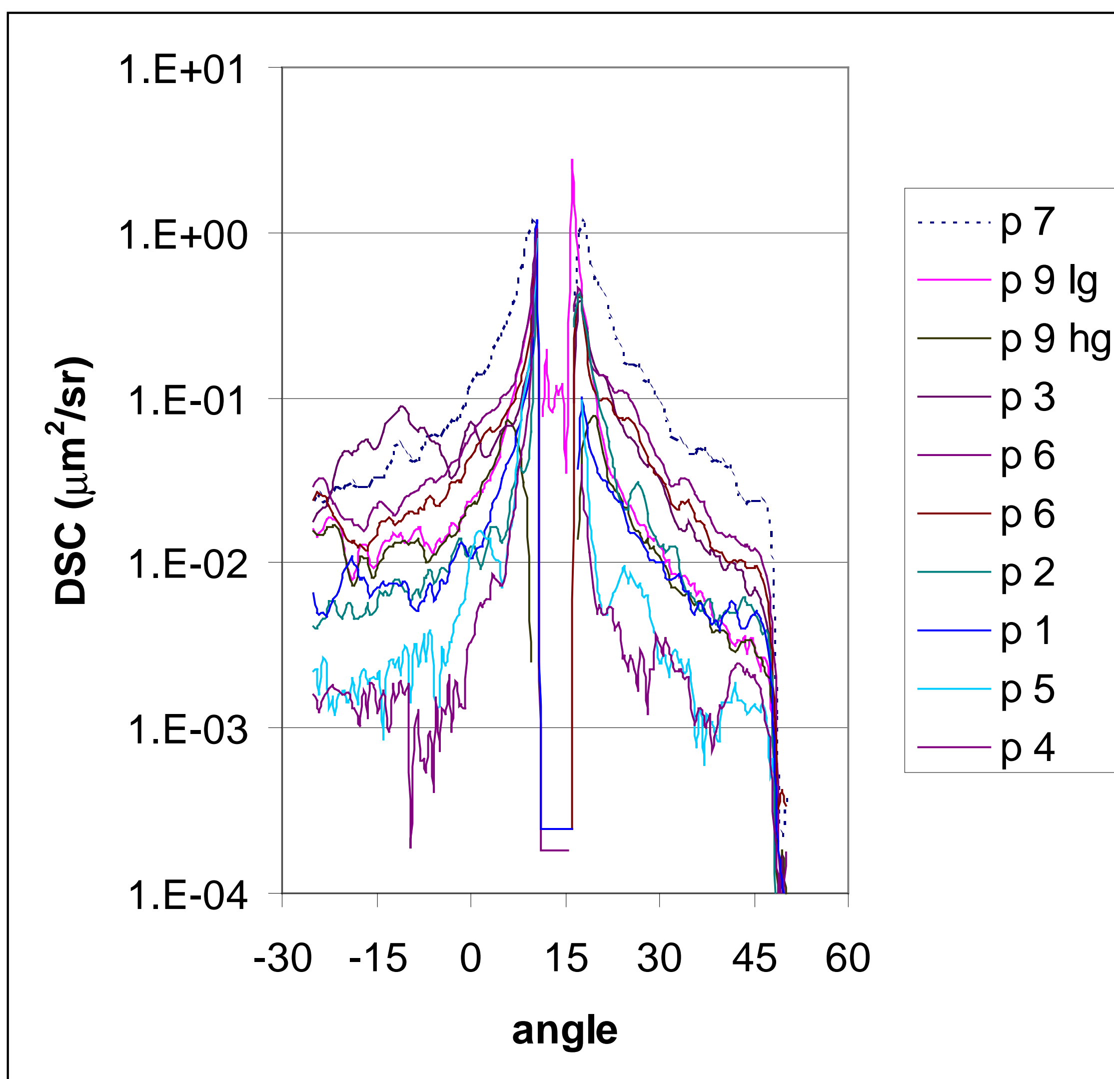

FIG. 22. Angle scans from suspected 700 nm PSL spheres.

The gap in the central region from 10° - 15° is the range of values where the detector is saturated.

Particle 7, lying outside the deposition region and several times the magnitude of the others, is most likely either a contaminant or a PSL sphere that came dislodged from the deposition area. Its general similarity to most of the other plots, albeit increased by a factor of 3, suggests that it does represent such a dislodged particle, but it will be assumed to be a contaminant.

Particle 9-lg and particle 9-hg are the same particle, measured at 0.1 and 10 times the gain used for the other particles, to test for saturation problems and possible cancellation error near the center of the peak and to test for noise problems in the low-power tails. At low gain near the center, this particle bears strong similarities to particle 6 (scanned twice) and partly to particle 3, though on the far left side of the central peak particle 3 displays a peak at about –10°, unlike the others. This deviation might represent some kind of disturbance during the scan process. At high gain and through the lower part of the low gain scan, particle 9 is quite close to particles 1 and 2. This behavior displayed by the particle 9 scans suggests that some of the plots do suffer from cancellation error near the forward scattering (circumspecular) peak between 10° - 15°, though the low-gain particle 9 values will be good down to 16°.

Particles 4 and 5 are quite dim compared to the others and show some angular features which are not seen in the others scans. Thus 4 and 5 may be contaminants. Consequently, particles 1, 2, 6, and 9 will be considered to belong to the range of normal variation for the 700 nm particle scattering signatures, with the variation of about half a

decade probably arising from size variations or from the individual adhesion conditions, as mentioned, though some part of the variation may also arise from errors in centering the beam. This centering area could introduce as much as 30% error, though the particle 6 scan was used in the the non-Gaussian beam profile correction (FIG. 23), so the particle 6 signal should be considered to be the most reliably calibrated. The second particle 6 scan was taken 12.5 μm to the left of the first, showing the typical effects of centering error, FIG. 27.

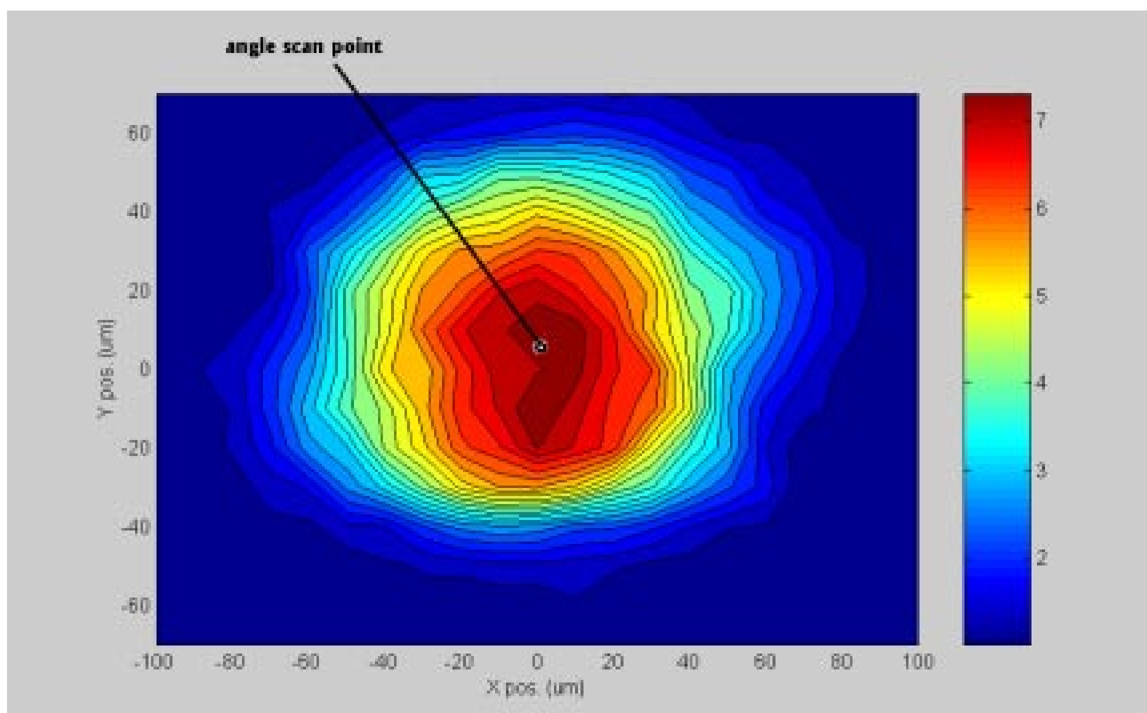

FIG. 23. Particle 6 beam profile (used for calibration), 230 nm, 45° inc., 30° detector.

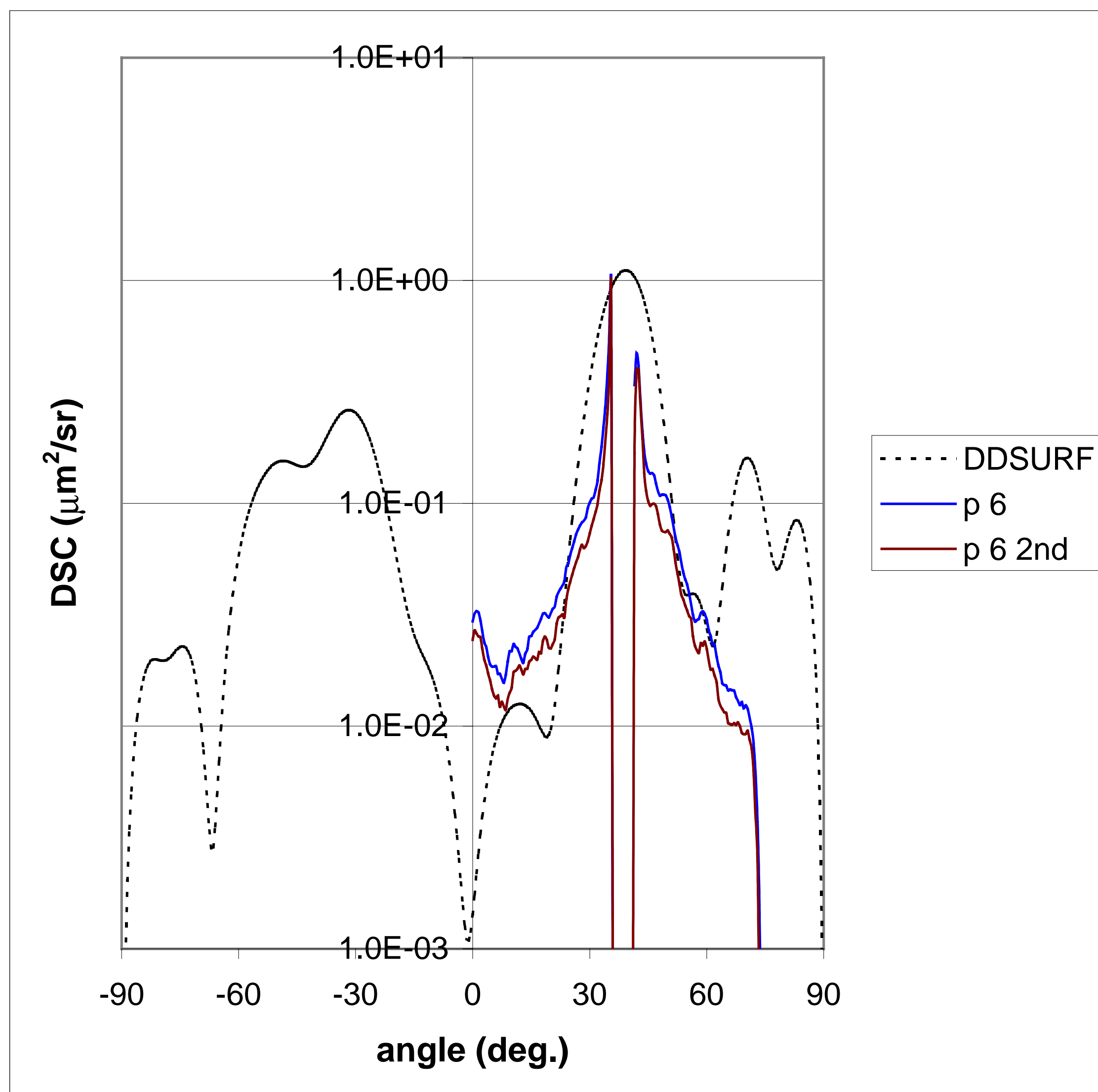

FIG. 24. Particle 6 scans compared with DDSURF simulation for n=1.55.

FIG. 24 also plots a numerical model of the differential scattering cross-section generated with the electromagnetic scattering simulation package DDSURF,[28] assuming a refractive index of 1.55 for PSL. This plot uses the DDSURF coordinate system, with the specular beam at 40° and the back scattering direction (near the incidence angle) at negative angles.

The particle 6 DSC agrees roughly with the model in magnitude, certainly within the factor of 3 variation seen among the measured 700 nm PSL sphere signals. The major point of disagreement is in the width and slope of the forward scattering peak, which is shorter and broader in the experiment than in the prediction. Much of this disagreement undoubtedly lies in the estimate for the refractive index n of PSL, which is unknown at this wavelength. 1.55 is estimated from the visible-light value, decreased slightly since most materials seem to display a trend of decreasing real refractive index in the DUV, at least until an absorption resonance occurs.

FIG. 25 shows predicted DSC plots for five different values of n at 45° incidence (which is nearly identical to the measured 40° case).

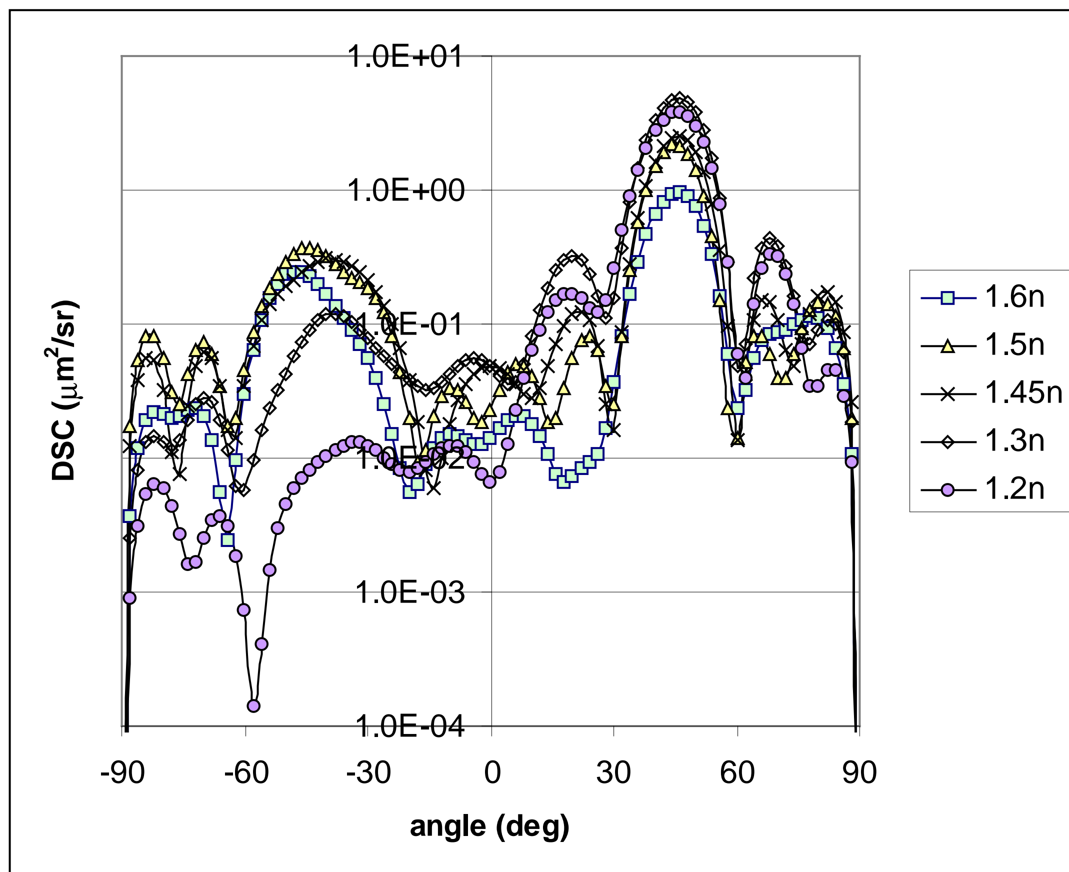

FIG. 25. Predicted DSCs for 700 nm spheres of varying *n*, 45° inc., 230 nm unpolarized light, on Si.

This range of values is fairly likely to bracket the true refractive index, although there is some possibility that it lies outside this range. Limitations in the software prevent simulations for larger indices at present.

These plots show that the magnitude of the forward scattering peak (right, at 45°) can vary by half a decade and does not change in a monotonic manner with respect to *n*. Thus some disagreement with the experimental values may arise from an error in the

choice of *n* as well, although this degree of agreement indicates that the model is at least roughly accurate.

The shape of the forward peak is quite uniform for all five index values, suggesting that the variation in the real part of the refractive index is unlikely to account for the disagreement in central peak shape. The variation of *n* though can apparently account for disagreement in the subsidiary peak positions and valley positions. Indeed, it might be possible to fit a series of simulations sufficiently closely spaced in *n* to the experiments in order to determine the unknown refractive index.

One other parameter which could help explain the forward peak discrepancy is the imaginary part of the refractive index *k*, which was assumed to be 0 in the above simulations. Polystyrene has an absorption peak reported by Nakai *et al.*[49] to be at 185 nm but another Fozza *et al*.[50] reports this peak to be closer to 195 nm, with the absorption at 230 nm measured to be around 10% of the peak value. The latter authors indicate that with the investigated polymers (including polystyrene) a "reasonable" value for the attenuation length for VUV light would be about 100 nm, which would correspond to a *k* value of 0.18 for 230 nm light. The 230 nm value for polystrene is likely to be somewhat less than a typical VUV value, though still close to the same order of magnitude, so an estimate of 0.1 would not be unreasonable. Changes in the values of *k* over this range (for $n = 1.5$) however do not seem to affect the form of the forward scattering peak strongly, though they do have significant tendency to reduce the subsidiary peaks and especially on the back scattering peak.

Using the 0.1 estimate of *k* might improve the agreement of the details of the scattering signature, but given the current uncertainty in both *n* and *k*, the observed agreement is as good as could be expected.

D. HARI sample

Scattering measurements were also conducted on a high aspect ratio inspection (HARI) defect standard. This standard is a Si wafer with 1 μm of oxide grown on the surface and 210 nm diameter via holes etched in rectangular patterns (an aspect ratio of approximately 1:5). Selected via holes were intentionally underetched to simulate a common defect in the fabrication of small via holes.

Preliminary scans of this wafer revealed that the via arrays were fairly easy to detect, as expected, but off-normal angular scattering profiles have produced unexpected results in the bare oxide areas. For DUV scattering (230 nm and shorter wavelengths) and 45° incidence, the bare oxide region gives strong scattering peaks at regular angle intervals. The position of this train of peaks seems to vary slowly with position on the wafer surface, which probably indicates a very strong dependence on oxide thickness or possibly incidence angle, since the wafer probably bows somewhat in the wafer mount.

These oxide scattering peaks are a considerable nuisance in DUV measurements of the wafer since they tend to obscure the via scattering peaks, however only normal and near-normal incidence is of real interest for detecting under-etched vias. It is expected that near-normal incidence will be required to penetrate the via holes, due to the high aspect ratio, and fortunately, these oxide peaks seem to be absent at normal incidence.

The via arrays themselves produce a strong scattering peak, the location of which, as would be expected from diffraction theory, depends on wavelength.

High aspect ratio vias are known to be particularly difficult to inspect. This difficulty is believed to arise from a combination of the small lateral area of the feature and the comparative depth. Previous work has suggested, from simulations of the scattered near field within the via, that this relative depth and small diameter severely restrict the ability of incident light to penetrate to the bottom of the via, where the evidence of the common underetch defect lies. These simulations also suggested that short illumination wavelengths would ameliorate this difficulty, since shorter wavelengths appeared to penetrate more deeply into the via.[19]

Given the interest in HAR via inspection, it was therefore proposed to apply the unique deep and vacuum ultraviolet angle-resolved scattering measurement capabilities of the Hybrid Emission Ultraviolet Defect Inspection apparatus developed as a part of the current task to determining whether these suspected advantages short-wavelength inspection might prove useful.

The sample wafer is one of a set of test samples/standards fabricated by SEMATECH to support tool evaluation and research into methods of HAR inspection and is described below.

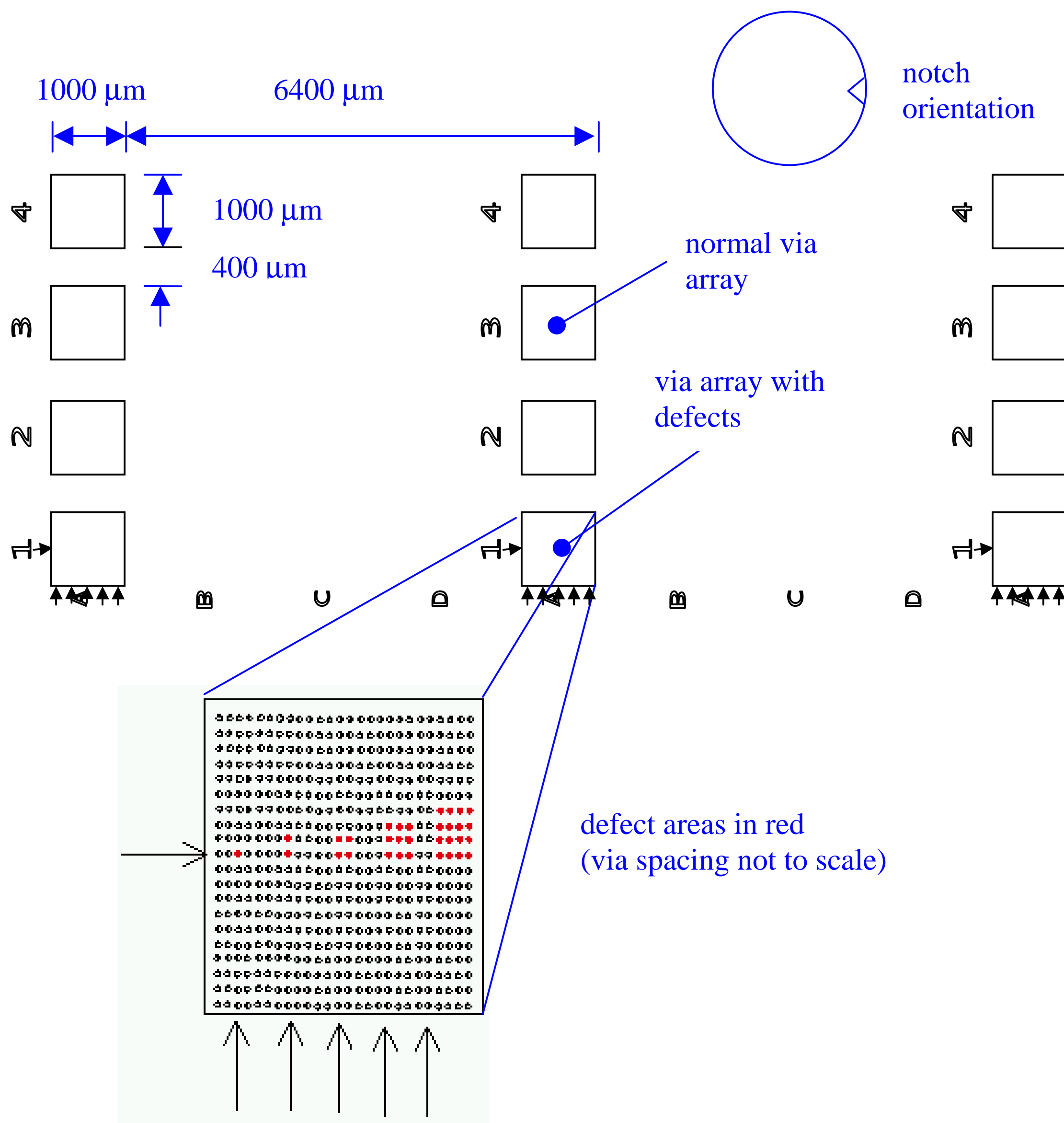

FIG. 26. Diagram of HARI wafer via arrays. (Inset courtesy of Rick Jarvis of SEMATECH.)

FIG. 26 shows a schematic layout of the SEMATECH HARI wafer. The particular sample used here has 210 nm diameter vias through 1 μm of SiO_2 (approximately a 1:5 aspect ratio). In the present experiments, the wafer is oriented with

the arrays lined up vertically. The via pitch is 0.5 µm, giving around 4 000 000 vias per array, and the programmed defects are 500 Å of SiO_2 in the bottoms of the defect vias. A wide-area scattering scan is shown in FIG. 27.

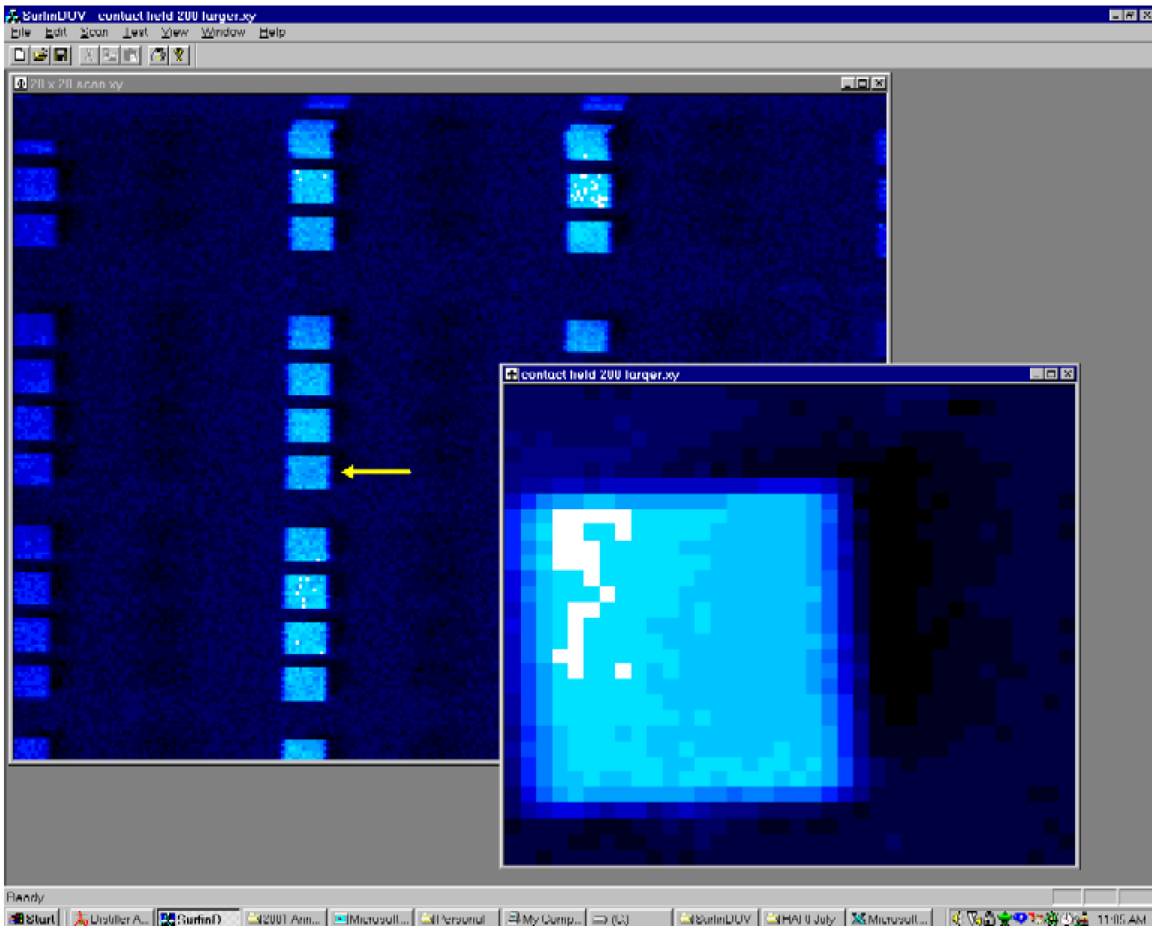

FIG. 27. Large-area scatter map of HARI wafer. 200 nm, 45° inc. Arrow shows A1 array with defects (inset, 50 µm resolution).

With these DUV scattering measurements, it should be noted that the optical properties of the materials are qualitatively rather different from those in the visible spectrum, FIG. 28, so that the reflectance of the SiO_2 sometimes behaves oddly.

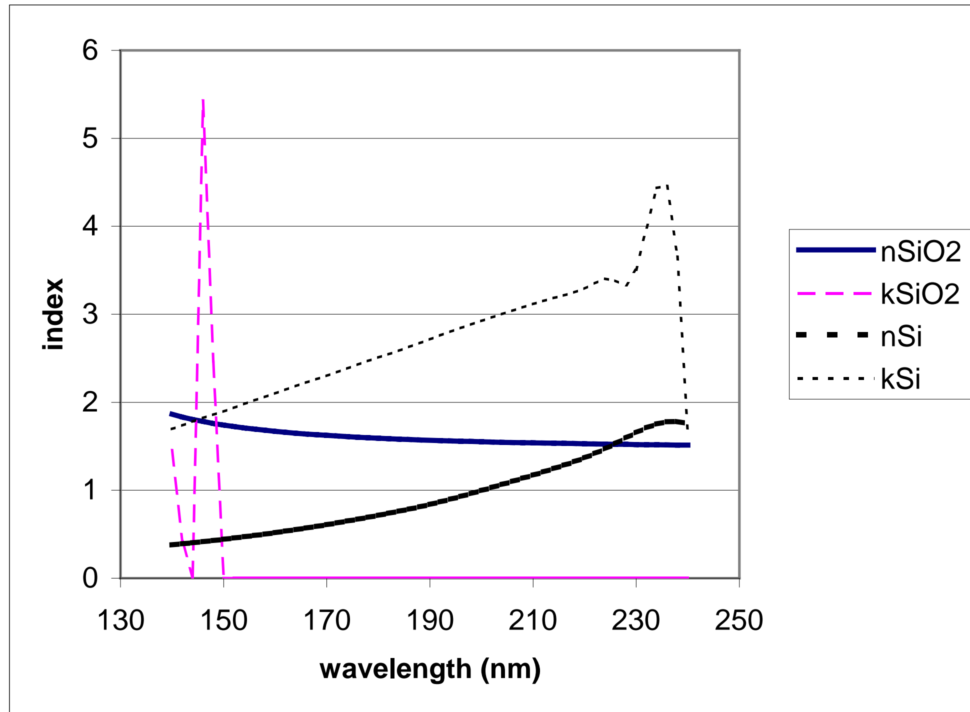

FIG. 28. DUV real and imaginary indices of refraction for Si[51] and SiO_2.[52]

1. S-polarization measurements

The first series of measurements performed were made with the *s* polarization. In this polarization, scattering by the via arrays is quite distinct, though unfortunately no clear contrast was found between the programmed defect regions of the A1 field and normal regions. Specular reflections from the wafer surface were also fairly strong, as is theoretically expected in this polarization.

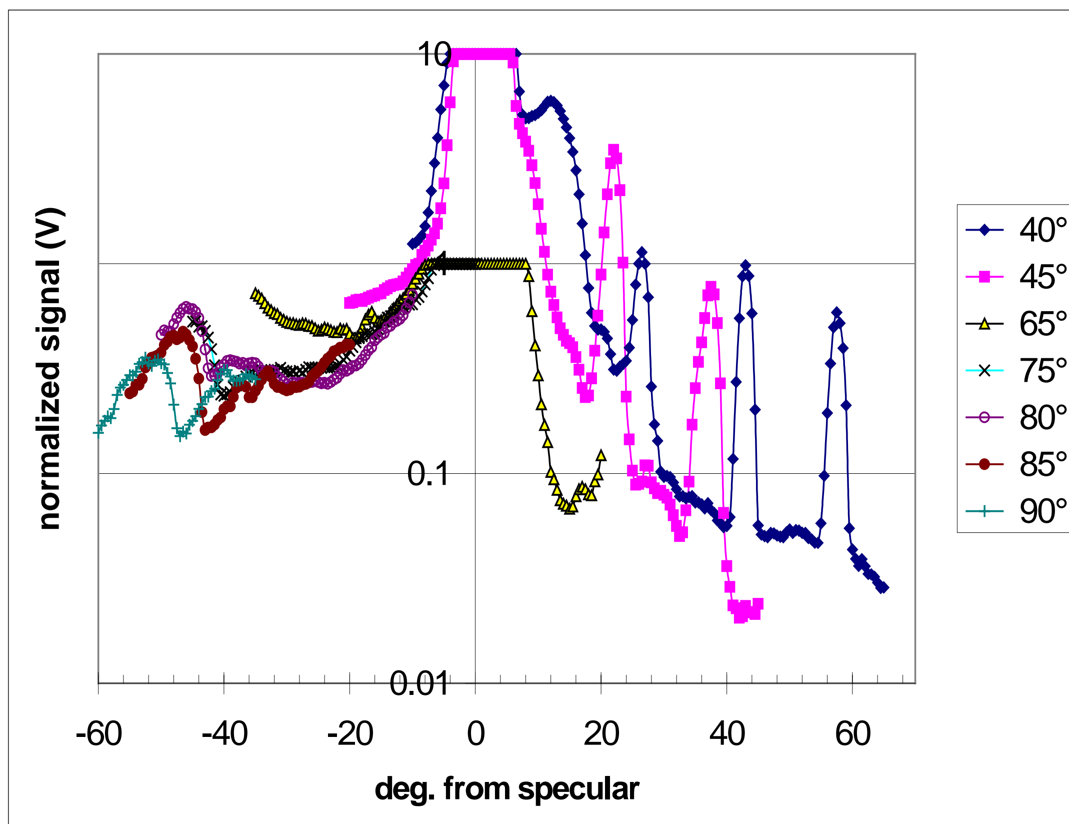

FIG. 29. Scattering by HARI via array for various angles of incidence, *s*-pol. 180 nm, beam width approx. 0.3 mm at normal.

FIG. 29 shows angle resolved scattering for 180 nm light at varying incidence angles (90º is normal incidence). In this plot, the specular angle has been centered, allowing clearer discernment of angular trends. In general, scattering tends to increase as grazing incidence is approached, though this trend is less clear with the intensities of the via diffraction peaks.

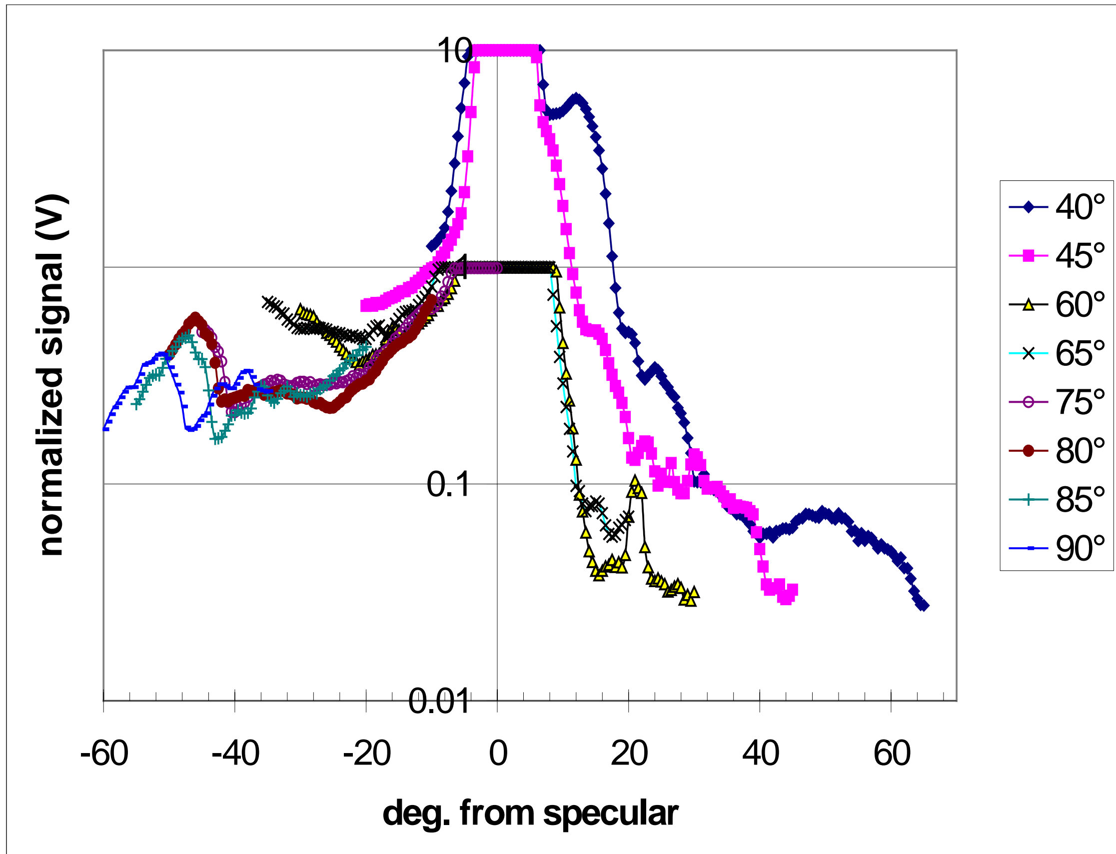

FIG. 30. Scattering by HARI oxide background for various angles of incidence, *s*-pol. 180 nm, beam width approx. 0.3 mm at normal.

FIG. 30 shows angle-resolved scattering from the background SiO_2 field (around 1 μm thick) around the via arrays for most of the same incidence angles shown in FIG. 29. Note that the peaks near -50º are present in either case, although they exhibit the same tendency to move toward the specular with shallower incidence as seen in the via array diffraction peaks.

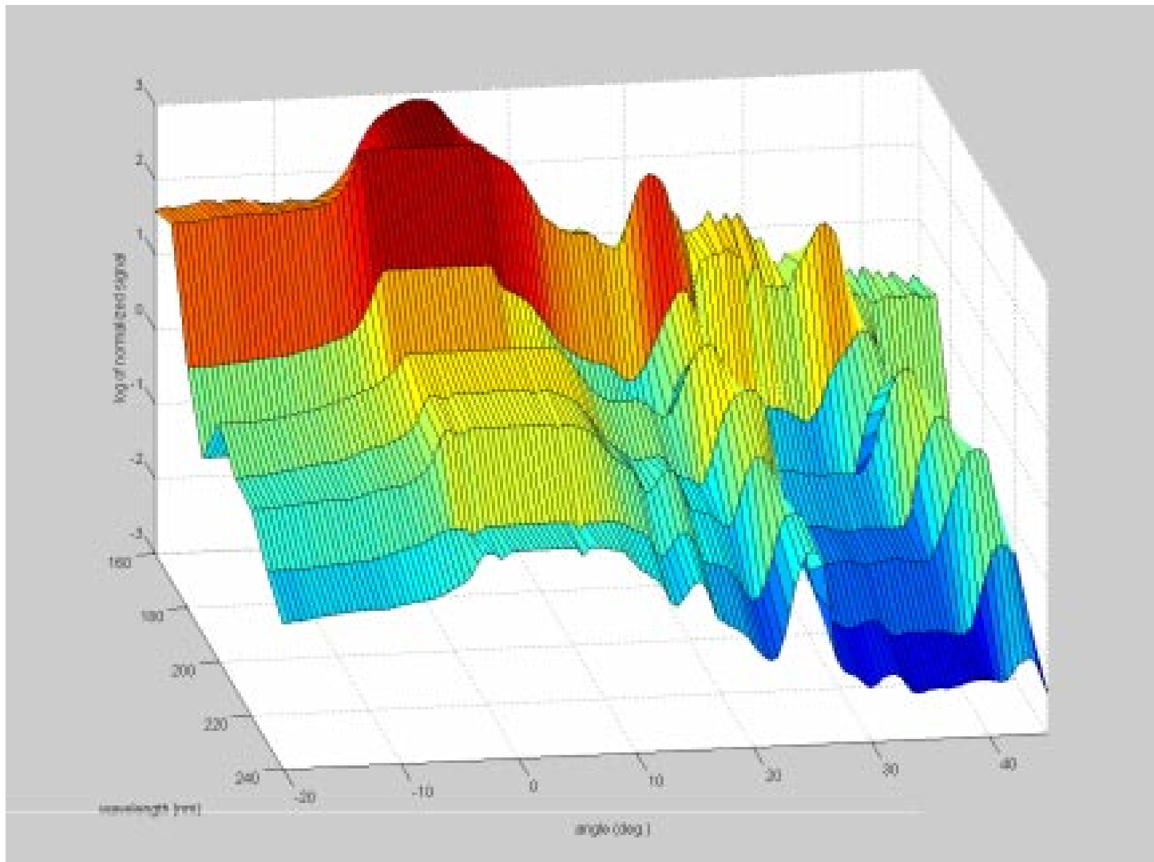

FIG. 31. Surface plot of spectral scattering by a via array vs. angle, *s*-pol., 45º inc.

FIG. 31 shows via array scattering measured over the DUV spectrum from 160 nm to 240 nm for the same vias studied in FIG. 29. Here the increase of via scattering with shorter wavelength is quite marked, though neither perfectly linear nor quite monotonic. The 160 nm measurements are unfortunately quite noisy and need to be repeated.

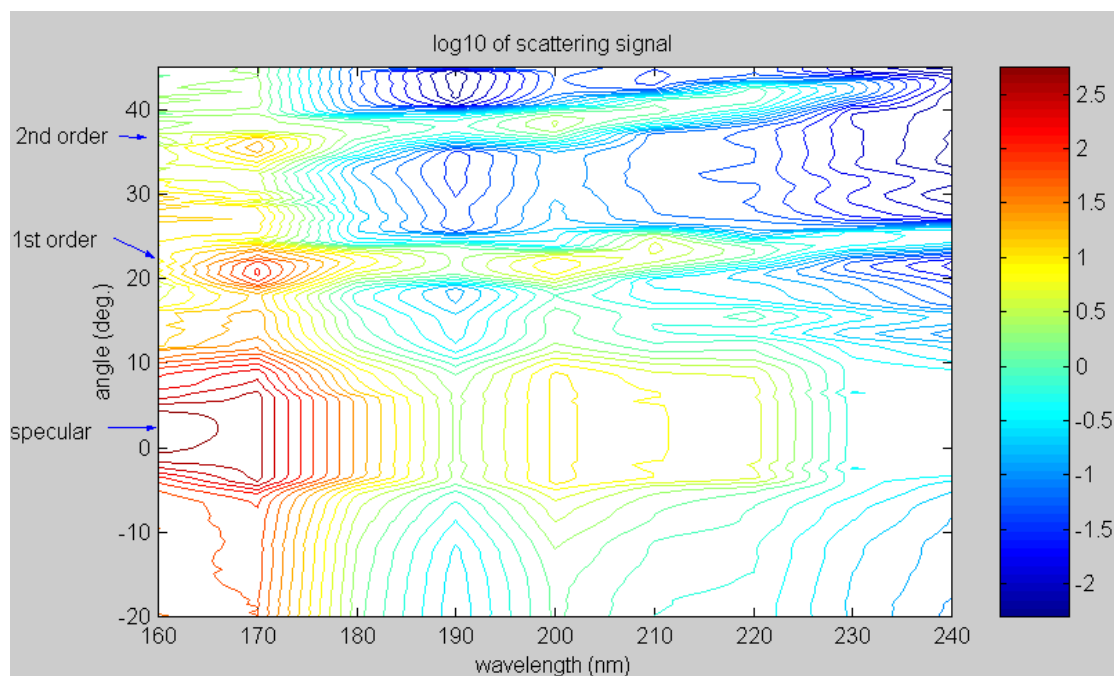

FIG. 32. Contour map for FIG. 31.

A contour map (FIG. 32) serves better to illustrate another feature of the spectral scattering data, the gradual motion of the via diffraction orders inward toward the specular, a property which expected from basic diffraction theory.

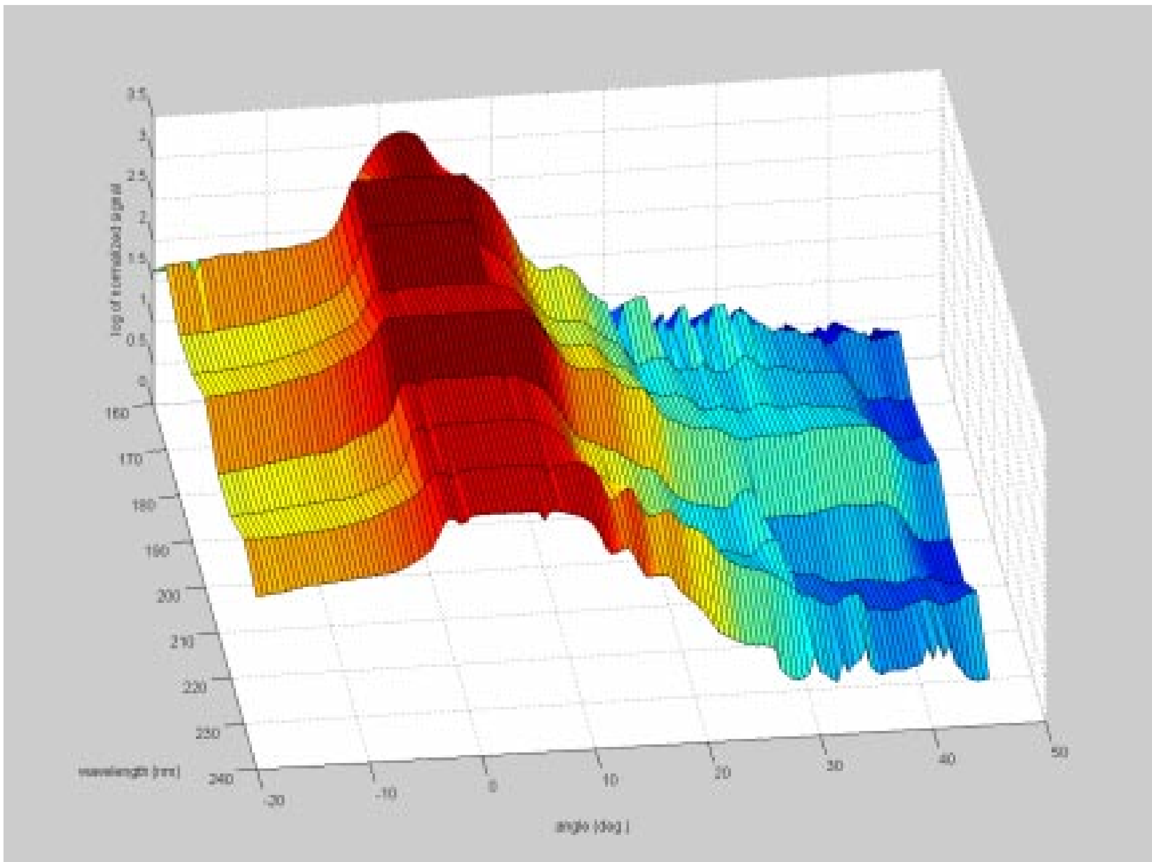

FIG. 33. Surface plot of spectral scattering by background oxide vs. angle, *s*-pol., 45º inc.

In FIG. 33, we see the spectral scattering for the oxide background, without the vias. A few things are notable here, first that the background scatter only weakly increases with shorter wavelength compared to via scattering, and second that the minimum scattering levels from the oxide are considerably higher than the minima with the via arrays. The former observation suggests that shorter wavelengths will tend to increase relative brightness of the via arrays.

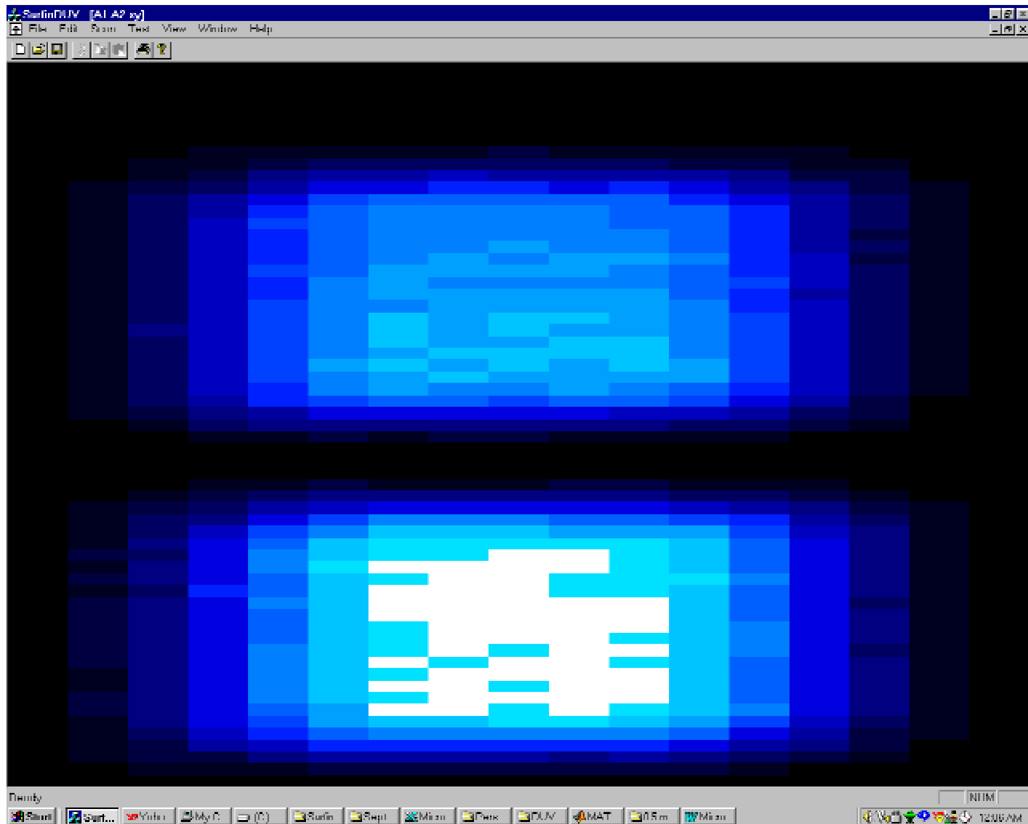

FIG. 34. X-Y scan of via arrays A1 (with programmed defects, upper) and A2 (without defects, lower) at 180 nm, 45º incidence, *s*-pol., detector at 37º.

FIG. 34 illustrates a typical X-Y scan of a pair of via arrays, used to locate the arrays for angle resolved measurement. The arrays are about 0.9 mm square, with the horizontal elongation due both to the aspect ratio of the image and the angle of incidence. The focus was set to maximize via scattering and this seems to give a spot size larger than the minimum, which results in the fairly low spatial resolution seen here. While the difference in intensity levels between A1 and A2 might suggest that the underetched vias in A1 are being observed, this intensity difference (approximately 10%) is within the level differences often observed between neighboring via arrays. These differences

probably result from a combination of bowing of the wafer, lack of perfect flatness in the wafer mount, and slight process variations in the oxide thickness, which are suspected to be particularly noticeable with DUV illumination.

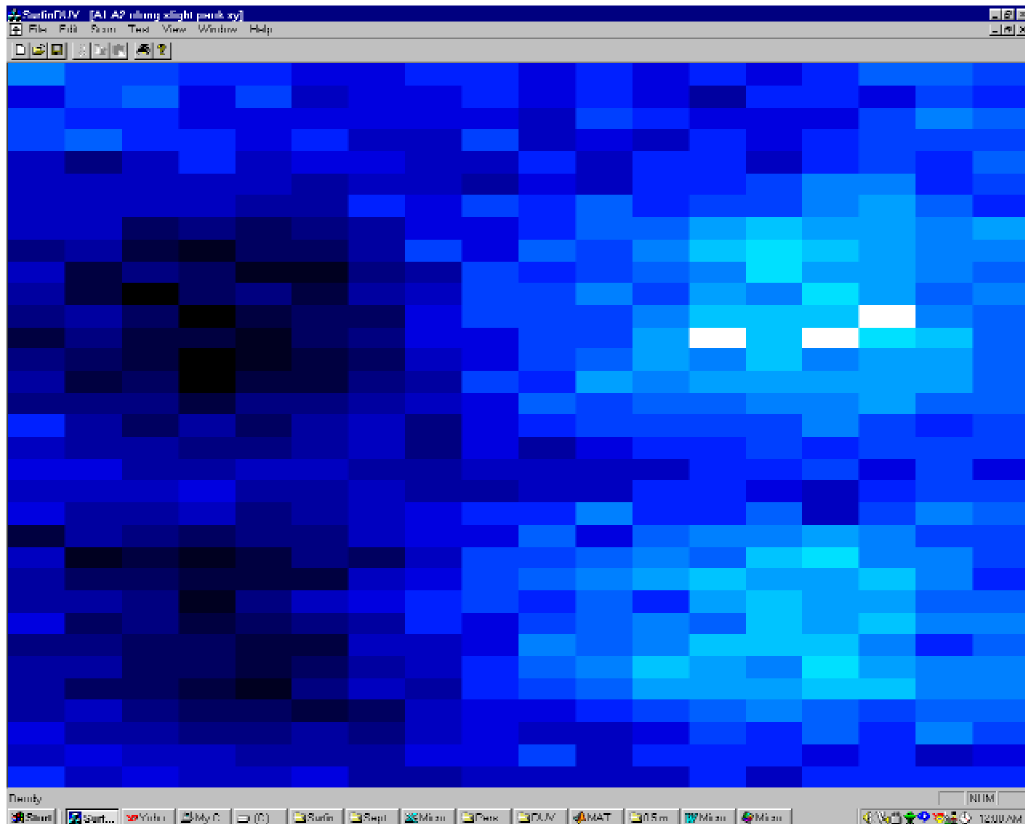

FIG. 35. X-Y scan of arrays A1 and A2, 190 nm, 45º incidence, *s*-pol., detector at 32.5º.

This X-Y scan (FIG. 35) shows an interesting phenomenon observed when scanning along a small via scattering peak between the regular diffraction orders. The position of this peak changes considerably between the left and right halves of the via area. This illustrates the contrast that may be found by observing what might at first

seem to be insignificant features in the angular scattering profile. Such subtle features are most likely to allow detection of underetched vias by scatterometry.

2. P-polarization measurements

The *p*-polarization measurements give qualitatively different results. The major difference is the distinct reduction in scattering by the via arrays. Strong scattering in this polarization was only detectable directly at 460 nm (and at longer wavelengths in general), although the vias were detectable in bright field scans at all measured wavelengths and incidence angles (FIG. 36), due to the reduction in specular reflectance they produced (as high as a factor of 40 in some cases).

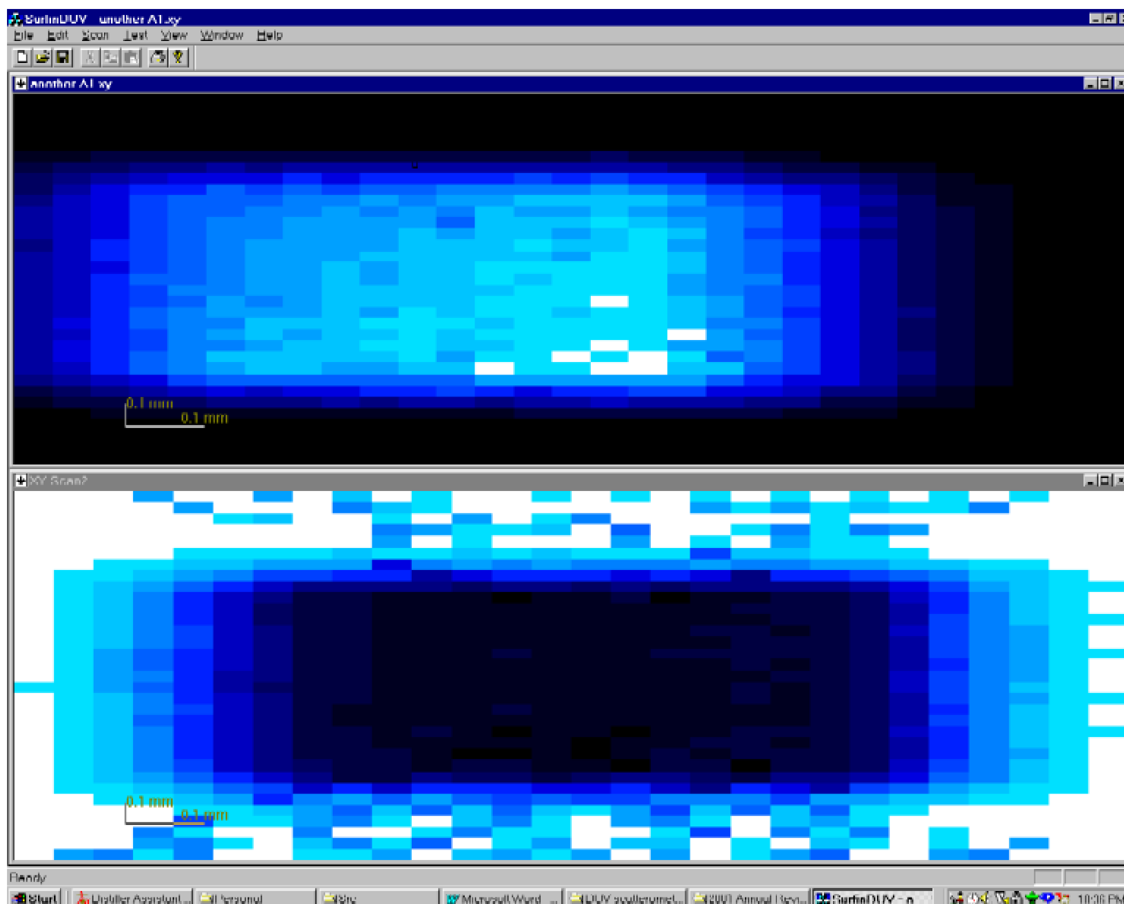

FIG. 36. Dark field (upper) and bright field (lower) scans of A1 at 460 nm, *p*-pol., 45° inc. Both scans cover a 1.4 × 1.6 mm area. The apparent shift in position is reproducible and may be an optical effect of the underlying SiO_2 layer.

FIG. 37 and FIG. 38 show angular measurements (quite noisy in the low signal regions) of via areas and bare oxide areas. Some variation may be observed in the profiles, mostly in the specular reflectances, but the via areas do show somewhat broader peaks due to weak scattering. The disconnected points of the two plots are points of very weak signal where electronic fluctuations have produced negative signal levels.

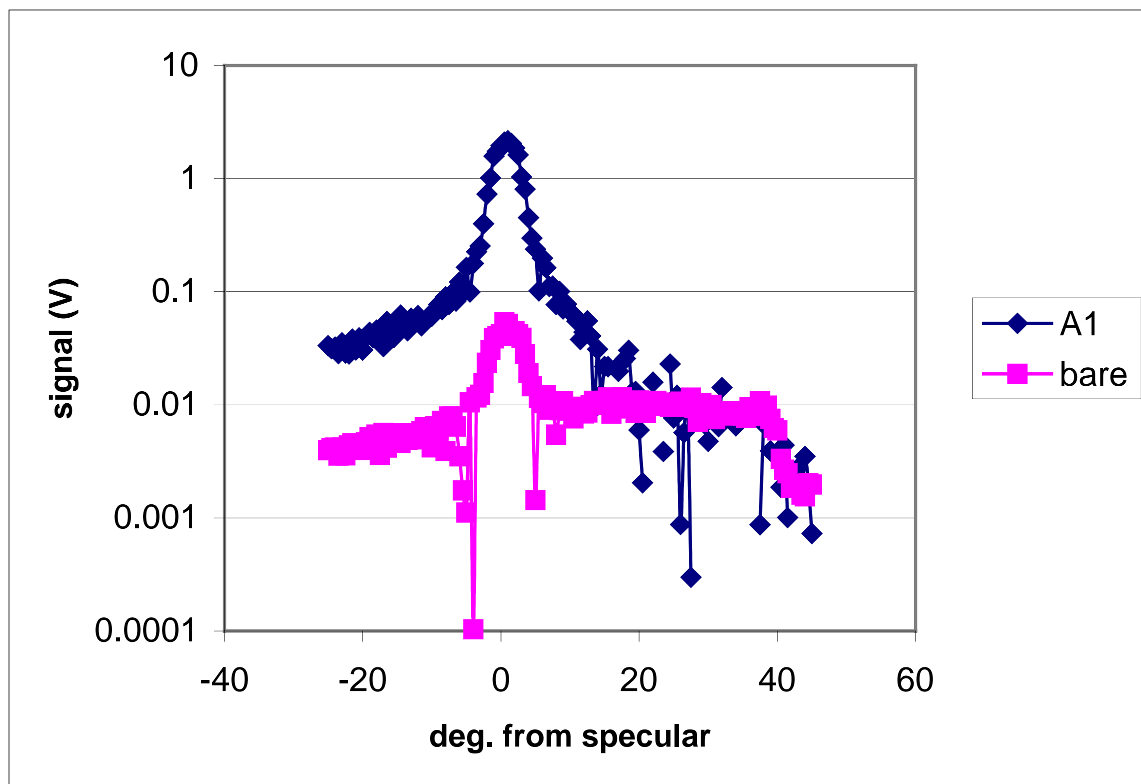

FIG. 37. Scattering from A1 area and bare area, 220 nm, *p*-pol., 45º inc.

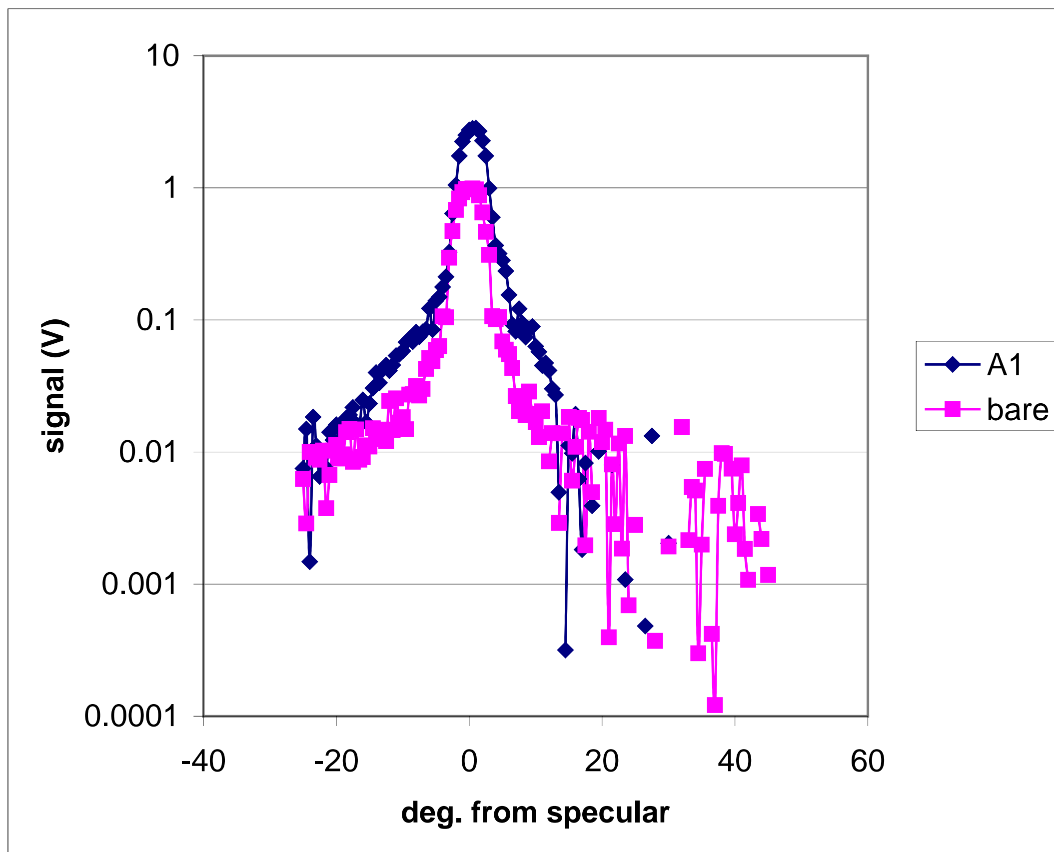

FIG. 38. Scattering from A1 area and bare area, 200 nm, *p*-pol., 45º inc.

These observations imply that in the DUV *p*-pol. the via fields either scatter light to angles that were not accessible (due to geometric limitations of the scatterometer) or absorb light quite strongly. It was evident as well that in the *p*-polarization scans that the *p*-specular reflections tended to be quite weak compared to the *s*-reflections, which is theoretically expected to some degree. Absolute measurement of this decrease in reflectance with the instrument is possible but has not been performed.

3. Comparison with Diffraction Theory

The grating equation may be used to give the expected peak positions for the via arrays, although it does not give the relative peak intensities.

The grating equation for oblique incidence is

$$a(\sin(\theta) - \sin(\theta_i)) = m\lambda \,, \tag{16}$$

where a is the spacing, m is the order, λ is the wavelength, θ_i is the angle of incidence, and θ is the angle of diffraction. The HAR vias are specified to be tiled on the surface with a 0.5 μm pitch, which, with the 45° angle of incidence, gives us predictions for the angular positions of the first two orders relative to the specular beam. These predictions are compared with the measured positions in FIG. 39. The curves are obviously mismatched by several degrees, however this mismatch could be explained as a positioning error in the angle of incidence, since modeling an incidence angle of 55.1° rather than 45°makes the curves fit well, considering that the measured values are only accurate to within a degree or two.

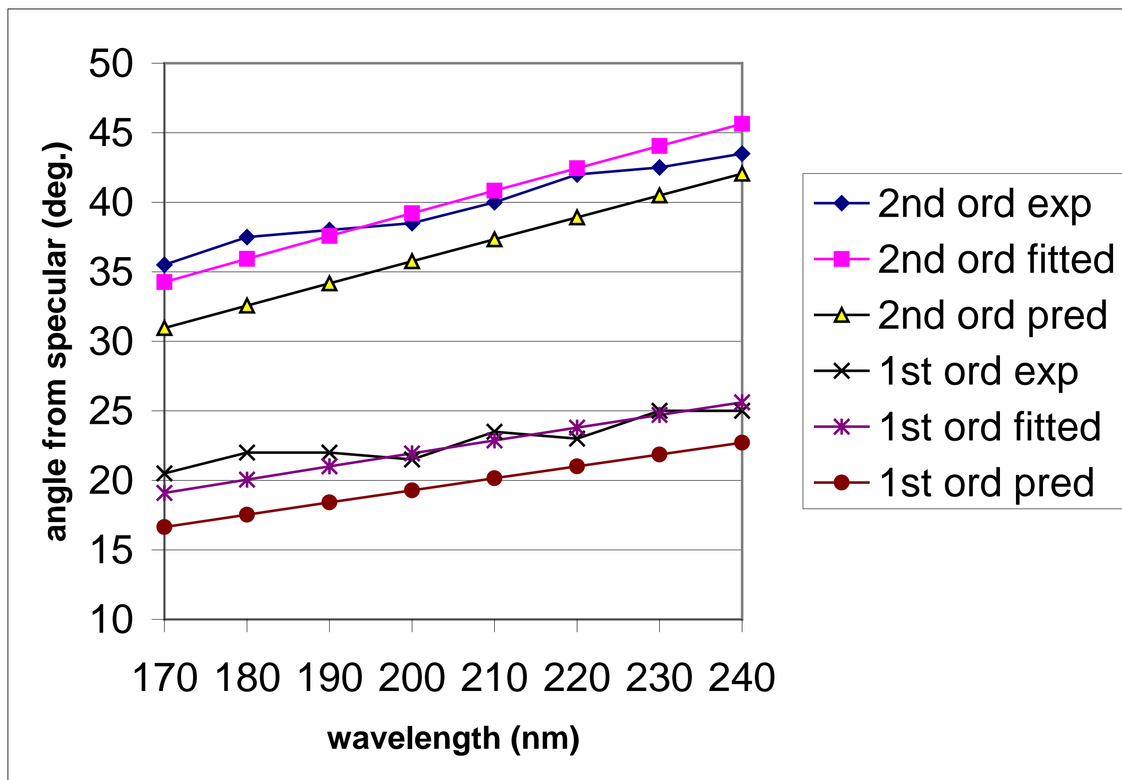

FIG. 39. Experimental, predicted, and fitted angular positions of the first and second diffraction orders from the HAR via arrays *vs*. wavelength.

This is a fairly large deviation though, since the error in angular alignment is not expected to be more than a few degrees. The deviation from the predicted values is probably the result of both this error and some deviation of the via pitch from the nominal value, to which the position of the diffraction orders is also fairly sensitive. A pitch of a little more than 0.7 μm would fit the observations closely as well.

IV. DUV-STIMULATED PHOTOEMISSION MEASUREMENTS

The photoemission capability of HEUDI is its most novel feature. While photoemission scanning microscopy has been demonstrated for a few decades and PE microscopes are even available commercially, those systems have focused on even shorter wavelengths than the HEUDI system, and have never been integrated as part of a scatterometry system. As important as the system itself though are the new concepts of surface inspection that it was designed to explore and test.

The experiments fall into these three main thrusts:

- Initial material photoemission measurements
- HAR via photoemission measurements
- Carbon deposition experiments

The material photoemission measurements mostly add little to the body of photoemission knowledge but are good starting points to work from for setting up the more interesting experiments and informing their interpretations. The simple material measurements do however show that even a fairly weak vacuum is adequate for PE-based inspection of the kinds of materials seen in semiconductor manufacturing. Photoemission signals from uniform layers of different compositions are measured and compared. Aside from testing the instrument, these measurements also give important information about the potential usefulness of photoemission from unprepared samples in a high vacuum environment, at the DUV/VUV wavelengths conceivably useful in a hybrid emission inspection system.

The HAR via measurements are intended to determine how effective photoemission inspection can be for finding topographic defects, in this case underetched high-aspect-ratio vias.

Finally, the third thrust is an attempt to determine whether carbon deposition produced by DUV-stimulated photoemission may be controlled by biasing the substrate. These experiments also allowed photoemission yield calculations for the two primary material surfaces involved, Si and SiO_2.

Additionally, Chapter V deals with the related topic of photoemission voltage contrast.

A. Photoemission apparatus

As discussed in Chapter II, the photoemission facility of the HEUDI apparatus currently uses an Amptek 501 channeltron as the photoelectron detector. This detector has the advantage of begin able to detect discrete photoelectrons (albeit with rather low efficiency) and amplify them to an easily countable pulse. The disadvantages are that it does have a rather low efficiency for low-energy electrons, making it quite susceptible to shot noise. It is also somewhat sensitive to vacuum ultraviolet photons, so that a certain background level of photon counts can add on top of the true photoelectron signal.

Several steps were taken to prevent the possibility of photon-originated spurious counts, most notably by positioning the channeltron at viewing angles that minimize scatter, particularly at out-of-plane angles for non-normal incidence angles. Detector proximity to the sample also can play a role with shorter distances increasing the received

photon flux, although the possible loss of photoelectrons must be balanced against this $1/r^2$ decrease.

The exact extent of photon background was tested with several approaches, mainly involving selective electrostatic rejection of the photoelectron current. One may also physically obstruct the aperture of the channeltron with an optically transparent but photoelectrically opaque piece of glass or (for shorter wavelengths) fused silica or fluoride. This method however seems to result in a situation wherein the obstructing window acts as the dielectric in a capacitor, so that after a time, a potential difference over the window builds up and eventually allows some detectable degree of current.

The 501 channeltron has a useful feature that allows two different pre-detection potentials to be selected, one at –400 V and the other at +100 V. The negative bias, used primarily for ion detection, rejects low-energy electrons, while the positive bias tends to reject ions and attract electrons. For PE experiments, the electron detection mode is naturally selected (so that most electrons strike the channel electron multiplier at 100 eV or slightly more), but by comparing measurements of a signal taken in both modes, we can infer the level of photon contribution, since only scattered photons contribute to the signal in the ion detection mode. This is somewhat inconvenient though, because this mode is switched via a jumper on the channeltron circuit board, making it necessary to shut down the vacuum system, remove the channeltron, and disassemble it to perform different experiments.

To make electrostatic photoelectron rejection somewhat more convenient, a simple external electrostatic deflector was mounted over the channeltron aperture.

Supplied by the PMT power supply, this can set up a 1000 V or more potential between two plates separated by approximately 5 mm. This can effectually draw off any electrons bound for the channeltron aperture and can be switched on or off (or adjusted in voltage) from outside the chamber.

The deflector also has an advantage in that it can be used to improve photoelectron collection efficiency at low voltages. With a high voltage, photoelectrons are completely swept into the deflector anode, but at low voltages, the electrons are deflected towards the anode but can still reach the channeltron aperture. Since the incoming electrons are not isotropically distributed, there is some inefficiency in the detector resulting from some portion of the electron stream missing the aperture and striking the front plate of the channeltron. The deflector can be used to alter the direction of the incoming electron stream (though in a slightly non-linear manner due to the energy spread) so that collection may be optimized. The function of the deflector plate is then closely analogous to an optical prism.

These experiments found that the photon background was quite small, enough so that it was unclear whether the counts were due to photons or perhaps a few stray electrons getting past the filter. In any case, the effect was found to be negligible in the experimental geometries used in this work.

FIG. 40 shows a typical plot of channeltron counts vs. deflector plate bias, for Al with 185 nm illumination. Typically, only a few volts' potential is required to steer the electron stream to an optimal direction, but the resulting increase in signal level can be a factor of 10 or more. Even the simple presence of the grounded deflector plates seems to

improve the signal somewhat, probably due to reshaping the electric field “seen” around the aperture.

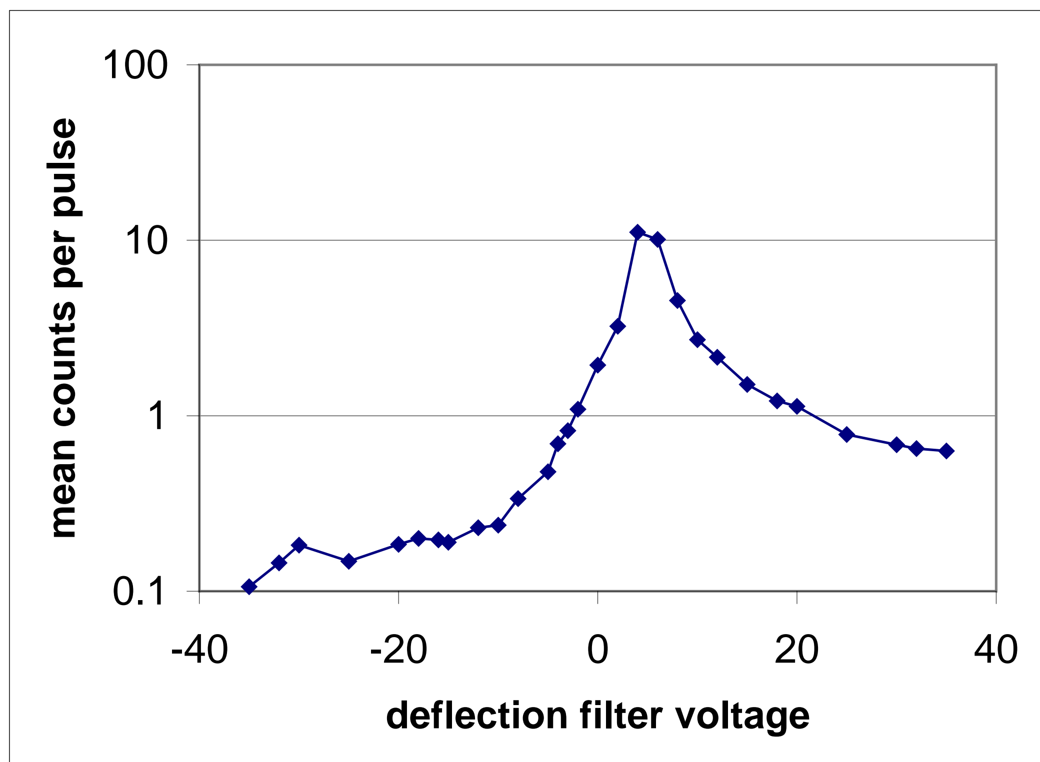

FIG. 40. PE rate with varying deflection filter voltage (aluminum, at 185 nm).

Experiments performed using the jumper feature have shown that there can in fact be quite a significant photoelectron background, particularly if the specular beam is not attenuated properly. However, even if the specular beam is “dumped” into a non-photoemitting surface, experiments show a fairly strong tendency to receive background photoelectrons. This background signal most probably comes from scattered light striking the chamber walls and various pieces of metallic equipment inside the chamber. This effect could be reduced by designing the electric field of the interior to retard photoemission from the walls (via a slight positive bias to certain components and

surfaces) and at the same time to direct electrons emitted in the sample region toward the detector aperture.

For the PE experiments, the beam convergence angle also does not have to be restricted (with a field stop) as tightly as in scattering experiments, so opening up the field stop with a smaller entrance aperture allowed a fairly tight and well controlled spot to be achieved without sacrificing too much power.

B. Analysis

The data obtained provide us with two important figures, photoelectron yield and contrast.

Photoelectron yield, the mean number of photoelectrons per incident photon, requires considerable knowledge of the experimental conditions to compute and depends on a number of poorly known quantities. The total yield,

$$Y = \frac{F_e}{F_p}, \tag{17}$$

of course depends on the total electron flux and the incident photon flux, neither of which are directly measured, since not every photoelectron enters the detector and only a fraction of those that do enter the detector produce a signal pulse.

Our measured photoelectron flux, F_m, is related to the total photoelectron flux F_e by

$$F_m = \eta_g \eta_c F_e, \tag{18}$$

where η_g is the geometric efficiency and η_c is the conversion efficiency of the channeltron.

η_g expresses what proportion of emitted photoelectrons reaches the channeltron and is influenced by the distance from the sample along with the electric field around the detector-sample area, and η_c expresses the probability of an incident electron being converted to a channeltron pulse. While detector distance is easily determined, it is much harder to determine the ambient fields; however the channeltron in electron collection mode produces a strong (100 V) accelerating potential which can be expected to collect electrons very efficiently when it is close to the sample. Thus at some minimum distance, this factor should be fairly close to unity and not vary significantly as the channeltron is brought closer.

The geometric efficiency also depends on the presence or absence of the channeltron aperture. This is usually removed for low-yield samples, although removing the aperture does expose the delicate electron multiplier tube to possible physical damage, so care must be taken when doing so. The aperture has an area of 0.1 cm^2 while the area of the funnel mouth uncovered is 0.79 cm^2, 7.9 times larger.

However, the effect of the aperture is not linear with area, with experimental measurements showing that the aperture reduces the detected signal by a factor of 40 ± 2, giving a geometric efficiency estimate of 0.025. The non-linearity with area may arise from the concentration of the photocurrent density along particular paths, which the small aperture has a higher likelihood of excluding. This explanation would agree with some deflection plate experiments that have suggested that steering the photocurrent along the face of apertured channeltron can have a substantial effect on the observed photocurrent.

The conversion efficiency of the detector η_c is also difficult to determine exactly, which makes PE yields inherently rather uncertain. With η_c though, the value is not so strongly dependent on the experimental setup, and so a rough figure can be obtained from the literature, if the PE energy is known. The energy of the incident photons (< 9 eV) is fortunately small compared to the channeltron acceleration potential of 100 V, so most photoelectrons, having only a fraction of the incident photon energy, will have energies only slightly more than 100 eV. At this energy, this channeltron, and channeltrons in general, tend to have a conversion efficiency of around 25%, as reported by Pashman *et al*.[53] These investigators, incidentally, found a rather wide range of values in the literature, which, the author suspects, might in some cases be due to a failure to appreciate the effects of the geometric efficiency.

Thus our best estimate of the relation between total and measured photoelectron current is

$$F_m \cong 0.005 F_e, \tag{19}$$

with the channeltron aperture. The coefficient increases to 0.2 when the aperture is removed.

F_p the photon flux is somewhat harder to measure, though it can determined much more accurately than F_e. We need to measure the incident beam power P_I and derive the incident photon flux,

$$F_p = \frac{P_I}{E_{phot}} = \frac{P_I \lambda}{hc}, \tag{20}$$

from that. E_{phot}, the photon energy, depends on λ, the wavelength, as well as the speed of light c and Planck's constant h. P_I, we measure using a VUV Si photodiode, an International Radiation Detectors UVG-5 photodiode, which has been calibrated by the manufacturer for VUV wavelengths.

The same gated integrator apparatus is used for measuring the incident beam as for collecting scattering signals from the photomultiplier and PE signals from the channeltron, and the characteristics of the detection system are already well known, so we can use

$$P_I = \frac{V}{Z} R_\lambda , \tag{21}$$

where V is the mean voltage per pulse measured by the GI, Z is the preamplifier input impedance (4700 Ω), and R_λ is the responsivity of the detector at the measurement wavelength.

The manufacturer's calibration data points were fitted to a cubic spline to interpolate at the decile wavelengths at which most experiments are conducted with the HEUDI system to produce

Table 2.

Table 2. UVG-5 photodiode spectral responsivities.

Wavelength (nm)	Responsivity (A/W)
140	0.06229
150	0.07665
160	0.1164
170	0.1377
180	0.1369
190	0.1149
200	0.09540
210	0.08295
220	0.07483
230	0.07481

The mean voltages were measured by scanning the photodiode through the beam on the sample stage and averaging 25 means of 100 samples (the same sample rate usually used for PE detection) taken around the center of the photodiode's active area. The 2500 samples per wavelength reduce the random error to insignificance compared to other likely sources.

The whole formula then for photoelectron yield may then be expressed as

$$Y = \frac{0.005 F_m Zhc}{V R_\lambda \lambda} = 4.67 \times 10^{-4} \frac{F_m}{V R_\lambda \lambda}, \tag{22}$$

for λ in nm, V volts, F_m in electrons/s, and R in A/W.

The error in the expression is probably dominated by the errors in the channeltron efficiency, probably around half a decade, and in the geometric efficiency. The error in the geometric efficiency is though much more prone to causing underestimation of yield

than overestimation, because uncollected photoelectrons are inherently uncountable and missing them leads to overestimates of geometric efficiency.

Contrast is (in contrast) straightforward to calculate,

$$C = \frac{F_S}{F_B}, \tag{23}$$

where F_S and F_B are the detected signal and background fluxes. It should be observed that using the measured photoelectron fluxes rather than attempting to compute the true total fluxes emitted from the sample is more convenient for computing contrast. The ratio should be the same in either case, unless the detector collects the signals with different efficiencies or the detector is driven into the non-linear range. Instrument originated background, for example photoemission from the converging optics, can also influence this figure.

C. Experiments

1. Initial material contrast samples

These measurements were among the first performed, before the incident beam power was measured in absolute terms, so there are no absolute yields calculated. Section 3 however gives yields for some cases.

The first sample of this group, A, is a glass slide with aluminum foil laid over one side. Sample B is a 4-metal-layer BiCMOS test wafer. Sample C is a 2 inch single-side polished CZ-grown <100> silicon wafer purchased from Virginia Semiconductor. The focal spot size for the experiment was fairly large, around 1 mm, due to temporary problems with the focusing system. Measurements were conducted at several incidence

angles with incoherent unpolarized DUV illumination, mostly at 230 nm and 185 nm (3.4 nm bandwidth).

Sample A is a simple construction but provides a simple test of the photoemission measurement capabilities. Fig. 1 shows a scan of a 10 mm × 22 mm area (0.5 mm steps) covering both the foil and the glass background (lower part of scan). The Al region can be seen to be rather non-uniform. This is due to the relative roughness of the foil surface.

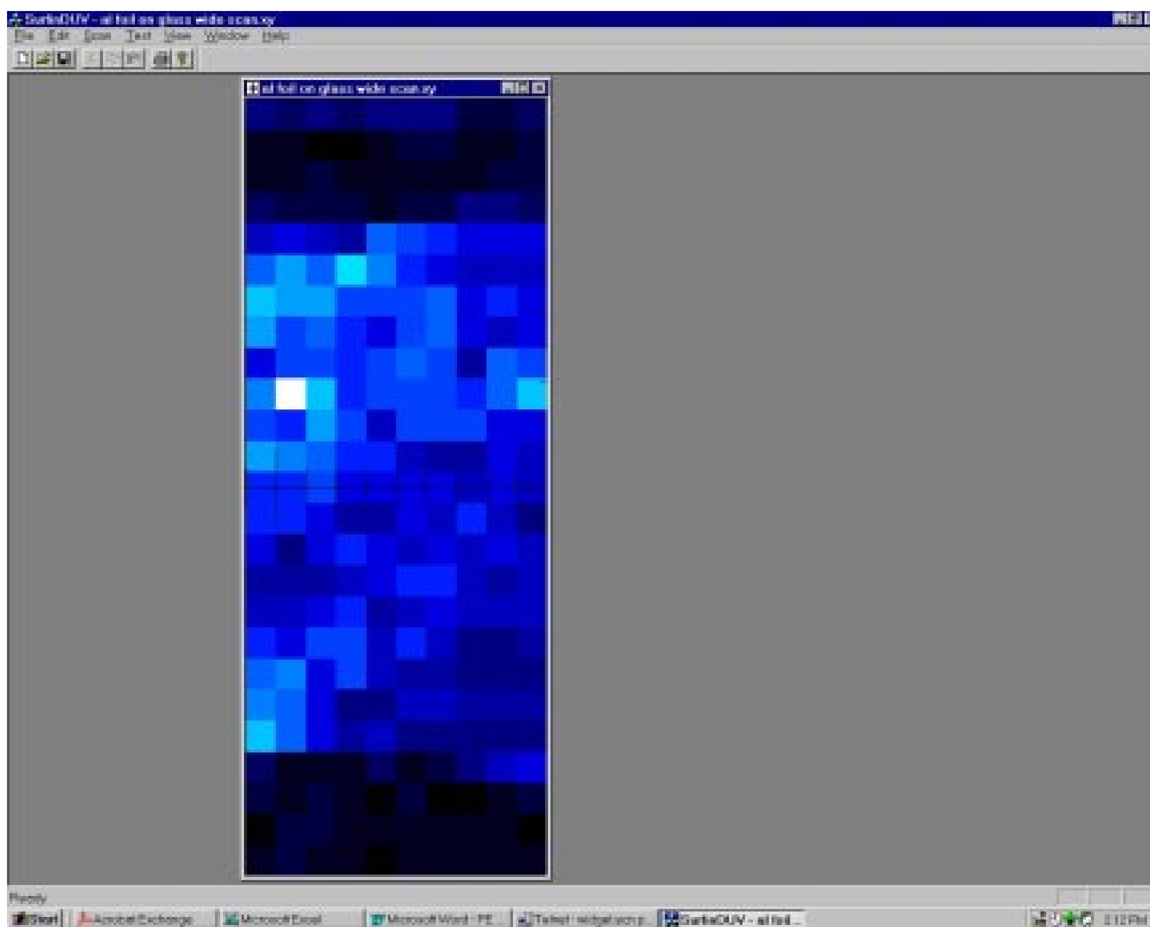

FIG. 41. Wide area (10 mm × 22 mm) 185 nm photoemission scan of sample A, Al foil on glass. Above the upper boundary of the bright region, the signal comes from the stage surface; below the lower boundary is the glass surface. Normal incidence.

FIG. 42 plots a vertical section of this map to illustrate the quantitative difference in signal levels. The graph in the 7 to 12 mm range corresponds to the glass surface while the range –7 to 7 mm corresponds to the Al foil. The signal level in the glass region is many orders of magnitude higher than the detector dark current, so this signal does represent some real quanta being detected by the channeltron. Photoemission by glass at this wavelength should be very weak if observable at all, so the signal probably consists mostly of stray photons. Some photoelectrons generated by stray light striking interior metallic surfaces are probably being collected as well, however.

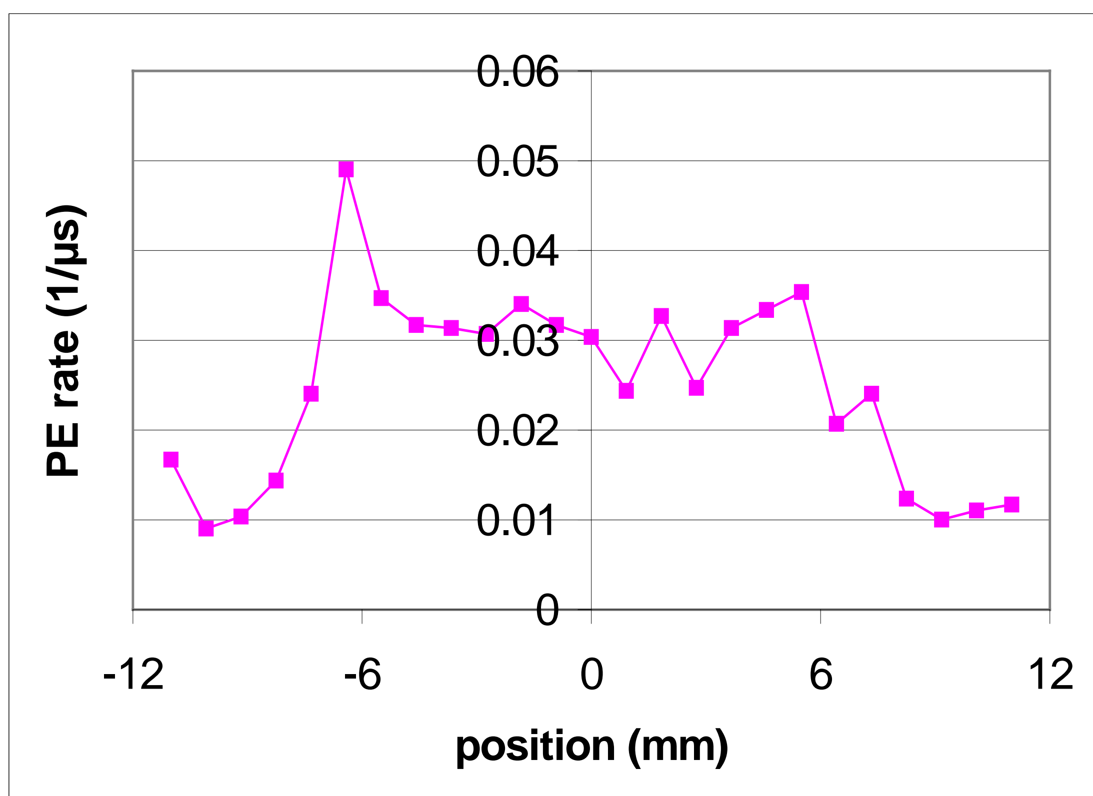

FIG. 42. Signal variation along Y direction (X = -7.66 mm) of FIG. 40.

Sample B is the most interesting sample of the first 3, since it consists a BiCMOS pattern (courtesy of Sang-Youp Lee), though from a large-scale test process. It is however harder to interpret, and the small sizes of the structures make them difficult to correlate with the PE signal, given the spot size in this particular experiment. FIG. 43 shows a straight-line scan from a central bare Si region (left) through two large metallic pads (large peaks at around –2.5 and 4 mm). The valley at 1 mm may be an oxide region.

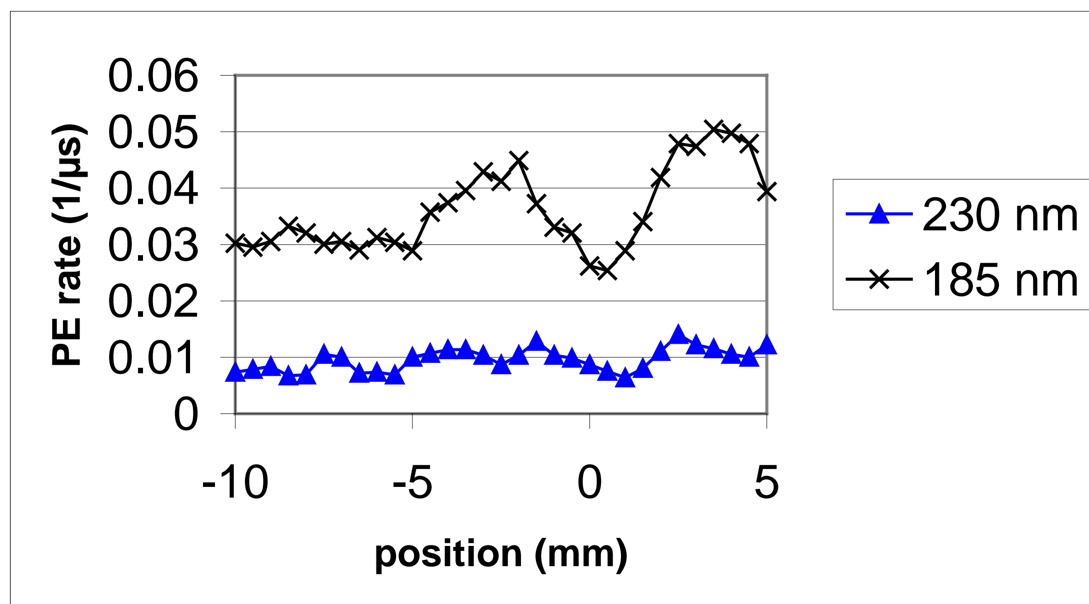

FIG. 43. PE line scans of BiCMOS wafer, 60° incidence (90° = normal) at 185 nm and 230 nm wavelengths.

Sample C is the least interesting in terms of features but it did provide a good uniform target for testing, and the Si photoemission measurements are of interest. FIG. 44 shows a plot of the count rate vs. wavelength. This indicates the system to be functional down to 130 nm, consistent with the design goals, and points out the spectral regions where system response to Si photoemission is at its peak. The area around 185

nm notably produces the strongest signal, with a weaker but significant peak around 230 nm. The latter peak is known to correspond to a spectral power peak in the source, and a peak is known to exist near 185 nm, but the 230 nm peak is believed be the more intense. The dominance of the 185 nm peak in channeltron counts probably results from a combination of the energy dependence of photoemission current and the stronger sensitivity to stray light at shorter wavelengths in the channeltron. Count levels in the most technologically important wavelengths, 157 nm, 248 nm, and 193 nm, are adequate or good, in the last case.

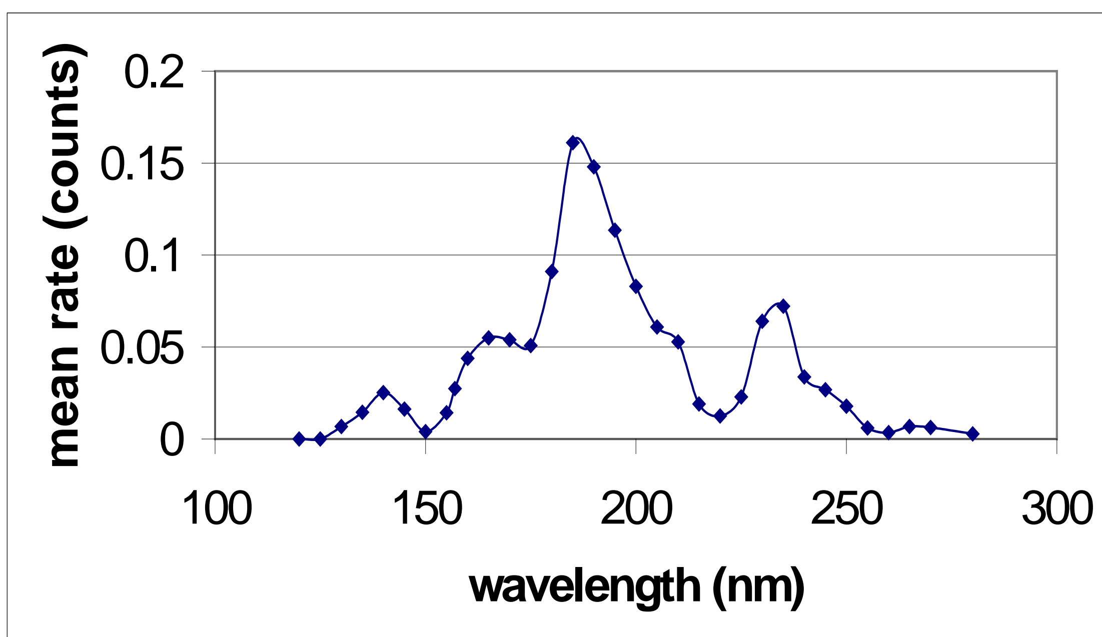

FIG. 44. Mean count rates (per 3 μS pulse) from Si for different wavelengths.

2. Carbon deposition experiment

The goal of the carbon deposition experiment was to determine the effect of PE-stimulated carbon deposition and whether this deposition can be controlled by a bias

potential on the metallic reflecting surface. Boller *et al.* have established that the buildup of graphitic carbon on mirror surfaces due to synchrotron radiation is due mainly to electrochemical reduction of residual hydrocarbons by photoelectrons rather than the primary photons themselves.[54] Similar buildup is known to occur in deep ultraviolet systems, and deep ultraviolet illumination produces photoemission, albeit at much lower energies, so it is reasonable to assume that a similar photoelectron-involving electrochemical process is at work.

It is well known that photoemission can be reduced and even stopped altogether by applying a sufficiently large positive potential to the emissive surface, so it is supposed that this carbon buildup may be significantly decreased or even prevented by applying positive potentials to them, relative to their surroundings. While Boller *et al.* used comparatively energetic illumination, in the range of several hundred eV and consequently requiring several hundred volts of potential to suppress the photoemission, for DUV photoemission, in which PE energies tend to be less than 5 eV, very small potentials should suffice. Even biasing mirrors to several hundred volts is probably readily feasible, but a bias on the order of 10 V would present even less difficulty in terms of special design for DUV reflective optics.

Therefore it was proposed to take an aluminum sample to which a varying potential may be applied and to expose it to a long series of DUV pulses while monitoring the reflectance from the sample. This experiment is quite easy to set up in the HEUDI system, which already has the required feedthroughs and optical detectors. A major disadvantage to using the HEUDI system for testing this hypothesis though is that

the flash lamp source has very little throughput compared to a typical synchrotron beam. The lower throughput of course implies that the total exposure time required to produce detectable carbon buildup is quite long, but the effects of a given degree of carbon buildup specifically on DUV reflectance were also unknown. The experiment was thus deemed worthwhile, if only to determine whether the instrument would be capable of this investigation. It also had the advantage that it could be performed during one of the periods when the stage motors were being upgraded.

Boller *et al*. found that under most conditions, a 50-Å layer of carbon could be laid down with a dose of around 10 A·s, or about 6×10^{19} photons. The HEUDI source can provide a few tenths of a microwatt (in pulses) at its highest throughput, which is a flux equivalent to about 1/5 that in microamps. Clearly, the source must run for at least 10^{8} s to lay down a layer of that thickness, assuming the low energy photoelectrons have the same hydrocarbon reduction efficiency, clearly an impractical amount of time to run the experiment.

However, one does often find that carbon deposition is considered to be a problem with optics while using DUV and VUV sources of comparable power to the HEUDI flashlamp, so the experiment was attempted nonetheless, in case the DUV wavelengths are more prone to the effect than expected from the results of Boller *et al*. Studies of the effectiveness of oxygen plasma cleaning at the Photon Factory in Japan[55,56] have indeed shown that the reflectance degradation peaks at around 7 - 8 eV (180 - 155 nm), and is generally stronger at lower photon energies, so that reflectance measured in the upper VUV range should tend to be particularly sensitive to carbon deposition.

Visual examination of the optics of the source collector mirror after about a year and a half of operation did not reveal any signs of fouling, but the metal monochromator slits clearly displayed carbon deposition. Carbon could also be seen on some of the exposed metal surfaces near the lamp, in a pattern apparently following the light distribution. This suggests that such deposition can be a significant influence on some components during the lifetime of this source.

The experimental setup was simple. A cleaned and abraded piece of aluminum sheet stock was wired to a lead connected to an electrical feedthrough and mounted with one end clamped between two glass slides, to insulate it electrically from the stage body. The stage was then positioned to place the aluminum sample at the focus of the 50 mm MgF_2 converging lens, with no beam reducing apertures in place so as to allow maximum throughput. Then the system was evacuated and the photomultiplier tube positioned to monitor the specular reflection. The specular beam of course usually saturates the PMT under high-throughput conditions, so the PMT accelerating potential was reduced from the usual 900 V setting to 800 V to lower the gain. A voltage was then applied to the sample from an external power supply and the lamp was fired at 50 pulses per second for an extended period. The specular reflection signal was recorded at intervals to monitor changes in reflectance.

This procedure was applied for 200 nm and 180 nm light with biases of +30 V (photoemission suppressed) and –30 V (photoemission enhanced) to get the data shown in FIG. 45.

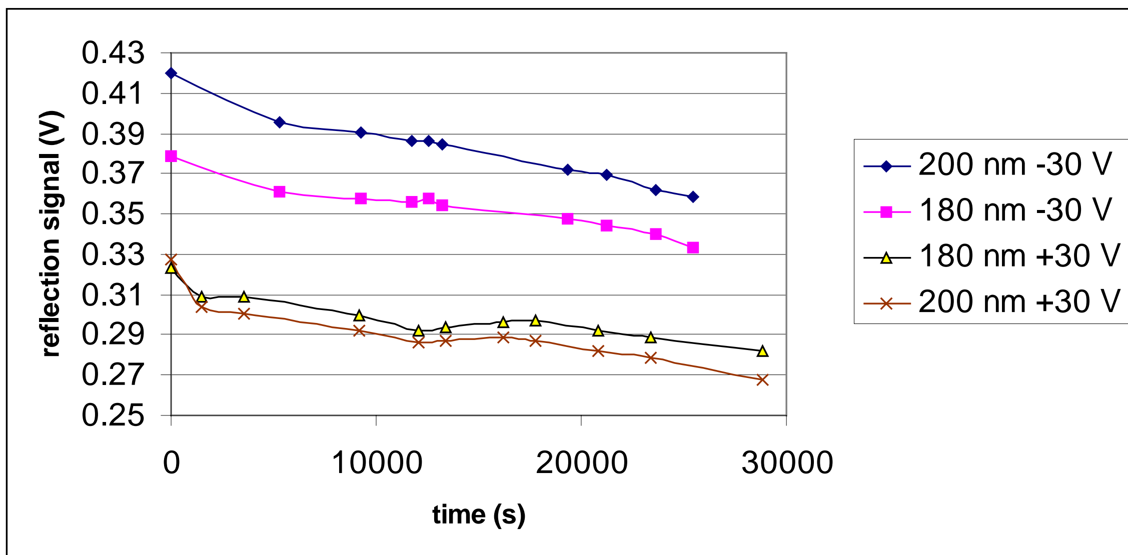

FIG. 45. Reflection signal vs. beam exposure time.

These curves show considerable decline in the reflection signal over time, however this decline occurs in both biasing cases, so it is unlikely to be due entirely (or even primarily) to photoemission from the reflecting sample. The flashlamp used is known to decrease in output power over time, however according to the manufacturer's specifications, this type of lamp, even at maximum pulse energy, should lose 50% of its output only after more than 10^8 pulses. These plots suggest approximately a 10% loss over 10^6 pulses and thus 50% after only 6 - 7 million pulses, more than 20 times faster than expected for the lamp-originated throughput degradation alone.

Two other possible explanations for this high rate of signal decrease are carbon deposition on the reflecting surfaces and solarization of the transmission optics. Carbon buildup on the sample itself despite the biasing conditions was eliminated as an explanation since changing the beam spot position to an unexposed part of the sample surface did not change the reflection signal significantly.

The system of course contains a number of reflective elements beside the experimental sample, the monochromator grating, the source collection mirror, and the two collimator mirrors. These optical-train components may be grounded and so should be subject to the hypothetical PE-mediated carbon deposition, however most of them also do not have beam concentration points on their surfaces, the grating being the exception. The experimental sample is at a beam focus (concentrated by about a factor of 200 in irradiance) and so should show a much faster rate of reflectance degradation than the elements in afocal planes. Two of the reflection elements, the source collector and the grating, however are illuminated by the full spectrum beam, and thus receive something on the order of 50 - 100 times as much total UV radiation, which will offset some of the concentration on the experimental sample. The grating though receives both concentration and the full spectrum, so, if it does experience carbon deposition, it may be the main source of the degradation.

One other factor may offset the grating's putative dominance of the degradation, which is the voltage bias of the sample. The grating certainly would have a potential no more negative than ground, while the sample had a –30 V bias, which in theory should have increased the sample photoemission rate significantly.

If the grating is the main culprit, the experiment might work better by temporarily removing the monochromator from the system and retrying the experiment with the full lamp spectrum illuminating the sample. This modified version of the experiment has not yet been performed though.

Even with throughput losses from other sources, the change in bias might have caused a detectable change in the rate of decrease in reflection signal. In fact, some slight decrease was found for the positive biases (perhaps apparent in the plot) but the change in the rate was not significant against the measurement error.

A future improvement of this experiment could also incorporate a beam splitter and a reference detector, which would allow removing most of the influence of the system throughput degradation from the signal, allowing the sample reflectance to the directly measured. The system's Rochon polarizer could be put to this use, assuming the degradation processes are not polarization-selective. The monochromator might also be used to select a wavelength especially sensitive to reflectance degradation, although the DUV-detectors (especially the PMT) may already be close enough to the optimal spectral sensitivity to make monochromation of the reflected beam only marginally useful.

3. HARI photoemission measurements

The HARI defect wafer is an interesting example of a type of defect for which photoemission inspection should be very well suited. As discussed in Chapter III, the high-aspect ratio vias are 1000 nm-deep circular holes in SiO_2, nominally 210 nm in diameter, which normally penetrate down to an underlying Si layer or substrate. The programmed defects are underetched vias, which have a 500 Å layer of SiO_2 over the silicon. Two problems with inspecting such vias optically are that incident fields do not penetrate sub-wavelength holes very efficiently and that the small bit of SiO_2 has very little effect on the reflected and scattered fields anyway.

Sub-wavelength apertures indeed resemble near-field optical probes,[57] such that we can think of a sub-wavelength-diameter via as a sort of near-field probe of its own interior with the attendant exponential decay of the field away from the surface (an evanescent wave). We should though keep in mind that along with this evanescent component that results from “leakage” of the surface reflection, there is also a transmitted component as well.

The decay length (analogous to penetration depth) of the evanescent wave of course is proportional to wavelength, so in that respect, shorter wavelengths reduce the likelihood of the via bottom to be illuminated. However, in this case, the via diameters are of the same scale as the wavelength, so the field can be expected to begin to lose its evanescent character at some point, improving the penetration. The simulations of Bionda, referred to earlier, seem to show just such an effect, which suggested that DUV illumination might be well suited for this purpose.

It was proposed that DUV light, of shorter wavelength than usually used in optical inspection, could improve the light penetration to the via floor, which was investigated in Chapter III, with equivocal results. It was also proposed that the light penetrating the via would produce much stronger photoemission contrast from the SiO_2 surface than the light produces in scattering (or reflectance) contrast.

The basic reason for this expected contrast is quite simple. In the fully etched vias, the exposed via floor is the semiconductor Si, while in the underetched vias, the exposed via floor is the insulator SiO_2. Semiconductors in general tend to photoemit more strongly than insulators because they accumulate less charge, and as well the

photoemission threshold for semiconductors tends to be less than for insulators, which is certainly true for the case of silicon and silicon dioxide.

Thus, fully etched vias should appear brighter in photoemission than underetched vias. Predicting the exact level of contrast is difficult however. First, we must know the wavelength dependent relative photoemission yields of Si and SiO_2. Then, we need to consider the cross-sectional area of the via relative to the spot size. Obviously, for spot sizes larger than 200 nm (which is effectively the case for anything but a near-field optical probe) the ratio of the via area A_v to the spot area A_s will, at best, multiply the ratio of the two PE yields to give the ratio of defect signal to good-via signal.

That simple model neglects though the possibility that the narrowness of the via might restrict the flow of photoelectrons. As well, the distribution of the electromagnetic field in the via, particularly right at the via floor, should have a strong influence on the signal. It is even possible that the via edges of the via mouth might enhance SiO_2 emission by concentrating the electric field lines. These effects would tend to reduce the defect contrast. Another possible non-obvious effect that could come into play, given our observations of evidence of SiO_2 surface conduction under DUV light, is conduction of current along the via walls to the Si floors of good vias. This effect might actually work to increase the defect contrast by brightening the PE signal around good vias. Though for a sufficiently thin SiO_2 layer on the via floor, it might instead brighten the defective via signal, reducing contrast.

Because of the apparent good potential of this technique and the many possible complications predicting its true utility, an experimental investigation seemed in order.

The first experiments used the weaker 50 mm MgF_2 lens because the channeltron is difficult to mount with short working distances. With the initial setup, basically the same as that used with the chrome mask voltage contrast sample (see Chapter V), no PE contrast, and indeed very little photoemission at all could be observed. This was not surprising, since the beam was large (~200 μm) and most of the area illuminated was a weakly emitting SiO_2 surface with very few conductive structures.

Removing the channeltron aperture and reducing the detector distance improved the PE collection efficiency sufficiently to get useful measurements.

Using the PMT to scan the surface for via scattering signatures and improve the focus, the via arrays were finally located (showcasing an advantage of the hybrid-emission approach at least for experimental work) and some PE contrast was detected, FIG. 46.

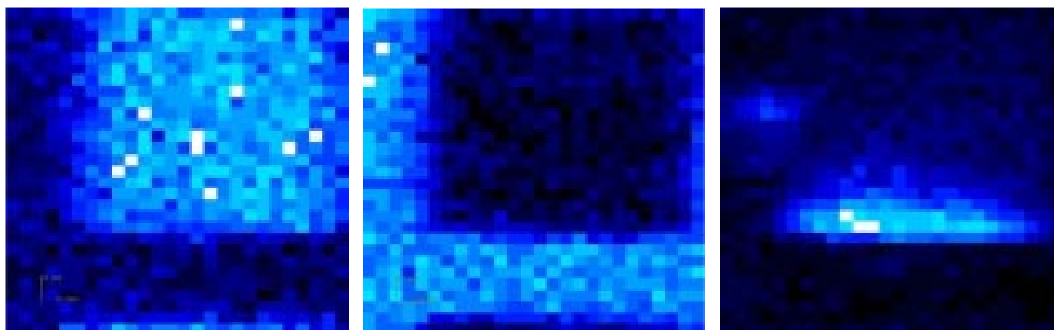

FIG. 46. Large spot via array scan, 200 nm illumination at normal incidence. Left-scatter at 60º, middle – scatter at 52º, right – photoemission.

The most noticeable features of the photoemission scan are the bright spot on the middle-left and the elongated feature at the bottom of the via area. These were surprising at first, but upon consideration it was noted that the HARI sample wafer was fabricated

with a large number of fiducial marks on the surface, which consist of areas where the SiO_2 layer has been etched away. Underlying the oxide is of course the highly emissive Si surface, so these fiducials, which are too small to be resolved individually with this beam size, appear quite bright in photoemission scans. Several such fiducials are located next to the via areas in order to indicate where the defects are, and these are apparently what produce the bright features. Unfortunately, the large beam, particularly the low-irradiance regions near the edge, tends to smear the signal out over the most interesting area, the largest programmed defect region near the middle-left.

More significant however than the fiducials is the light contrast over the via array in general. The mean via signal, outside of the fiducial-flare areas, is around 2.1 counts/pulse compared with about 1.3 for the oxide background (the fiducials peak at 4.7 and 2.6 for the brighter and dimmer features). There are 4 000 000 vias of about 0.03 μm^2 area, or about 120 000 μm^2 total for one via array, which is 12% of the surface area, so the expected contrast against the oxide background would be

$$C = 0.12C_m + 0.88\,, \qquad (24)$$

where C_m is the material contrast.

This would imply a material contrast of about 6. Other experiments suggest the Si/SiO_2 material contrast is around 2.8 at the 200 nm wavelength (FIG. 47).

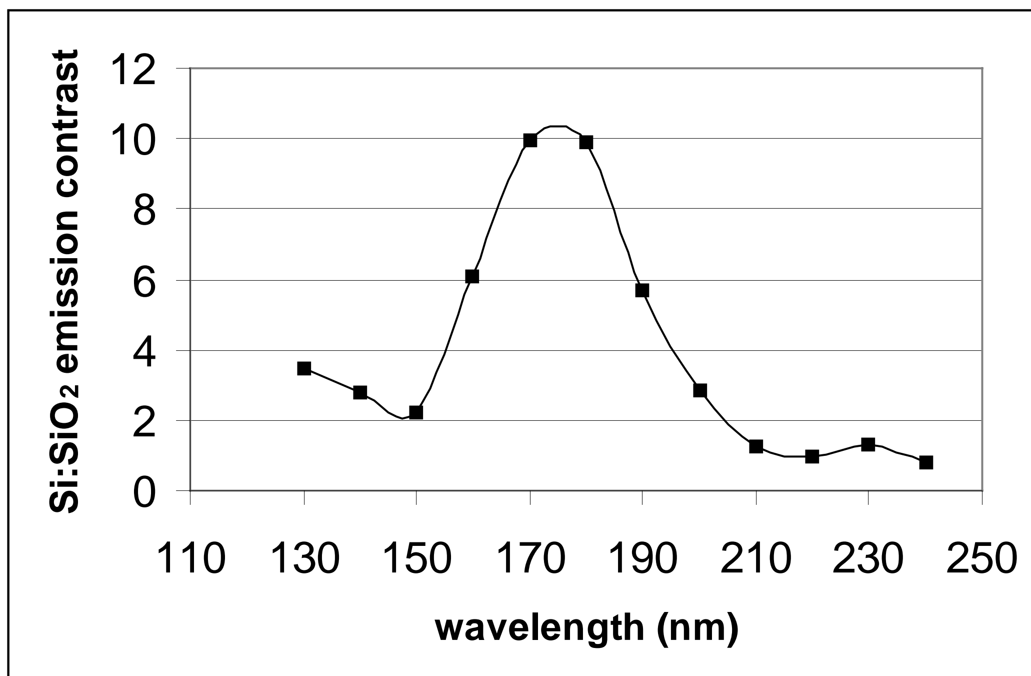

FIG. 47. Spectral Si (fiducial) to SiO_2 contrast for the HARI sample (95% conf. interval from sample error < 5%).

The at least rough agreement of the areal photoemission model does have positive implications for the detection of underetched vias though. It means that a significant part of the emission probably does originate from the via floors, where the defect contrast mechanism acts.

Scans at 140 nm revealed similar emission patterns, with the via area and oxide area emissions at about the same ratios, which is somewhat surprising since the spectral dependence of the PE yield is expected to differ significantly between different materials.

Having discovered these facts, it was endeavored to repeat the experiments with a smaller spot size. Reducing the spot size for the PE experiments was challenging

however. The more powerful 9-mm focal length fused silica lens was needed, along with a corresponding reduction of the working distance by about 35 - 40 mm.

At this closer distance, the channeltron aperture was almost completely obstructed, so initially the channeltron was repositioned with the long axis parallel to the wafer surface, so that its field of view was directly upward. This geometry lead to a very poor PE signal, suspected to result from the position of the aluminum lens mount relative to the channeltron. In that configuration, the path of the photoelectrons from the incidence spot to the channeltron aperture passed for several centimeters between the grounded lower lens support and the grounded wafer, which apparently diverted a large proportion of the current away from the detector.

This geometry problem was solved by rotating the lens mount 90° so that the lens supports were horizontal and perpendicular to the photoelectron path. This also allowed the channeltron aperture to be brought closer to the incidence point and aimed more directly at it. These steps increased the signal to usable levels, although there was still marked attenuation of the signal.

To determine the magnitude of the effect of this attenuation, photoemission from a Si wafer, bare except for a sparse deposition of 700 nm PSL spheres, insignificant to the PE yield, was measured with varying lens distances, FIG. 48. A uniform surface was necessary for this experiment of course to eliminate the effects of varying spot size as the distance was changed. In cases of very low conductivity and very high photon flux density, it is possible that spot size might have some effect on the total current due to

highly localized charging, but for this low-intensity semiconductor sample, such an effect is very unlikely to be significant.

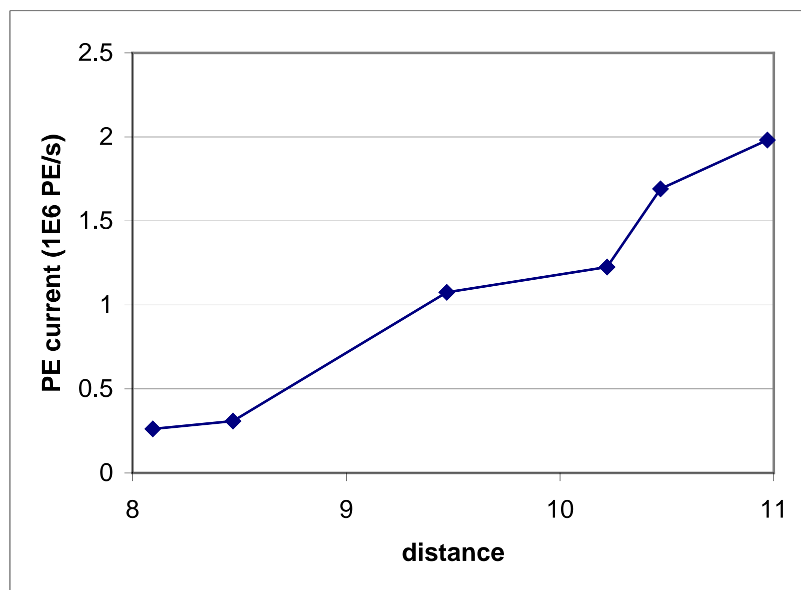

FIG. 48. PE rate vs. distance between lens and sample for Si wafer at 230 nm.

The data curiously seem to give a linear dependence on the distance, at least over this range. For the weaker lens with 45 - 50 mm working distance, this effect is not observed. It is clear however that short working distances can produce a quite strong attenuation of the PE signal. This effect could probably be reduced by several means. A lens mount made of insulating material might help, or the metal mount could be biased to some low negative potential, high enough to present a repulsive force to photoelectrons but low enough not to induce a significant positive charge in the sample. The latter electrostatic solution would probably require some fine tuning to get the best compromise between its influence and that of the electron detector.

With the longer-working-distance lens, some slight dependence of signal on lens-mount distance is observable, though it is usually no more than 10% over the distance typically moved by the mount during focusing, a few millimeters.

Experiments with the orientation of the channeltron aperture were also performed to determine how this affects the apparent signal. In one run, the channeltron was faced more vertically, with a direct view of the lower edge of the lens mount. In a subsequent run, the channeltron was faced more directly toward the beam incidence point on the sample. Interestingly, in the oxide areas, this produced only a slight difference in measured photocurrent (hardly even noticeable against the shot noise), however in the via areas, the signal was up to twice as strong as it had been. This suggests that much of the apparent oxide emission signal is really background photoemission from the lens mount. The metal lens mount is not directly illuminated of course, but some reflected and scattered light obviously strikes its surface, particularly when it is close to the beam incidence point on the sample (FIG. 49).

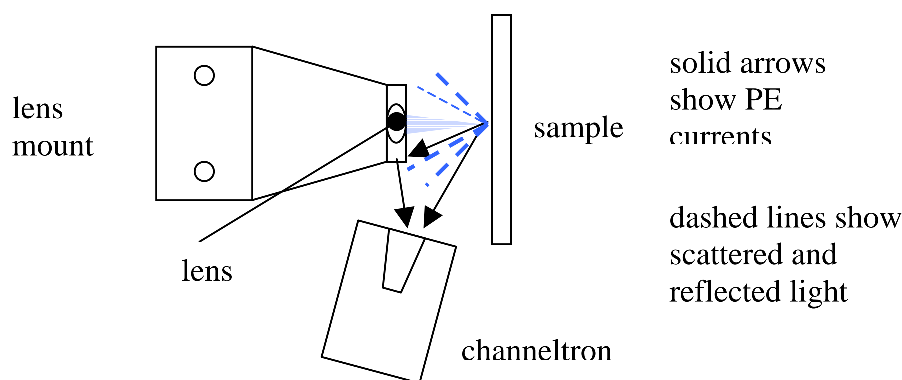

FIG. 49. 9-mm focal lens photocurrents.

To test this hypothesis, the lens mount position experiment was repeated, this time comparing the Si wafer and an oxide area on the HARI wafer, FIG. 50.

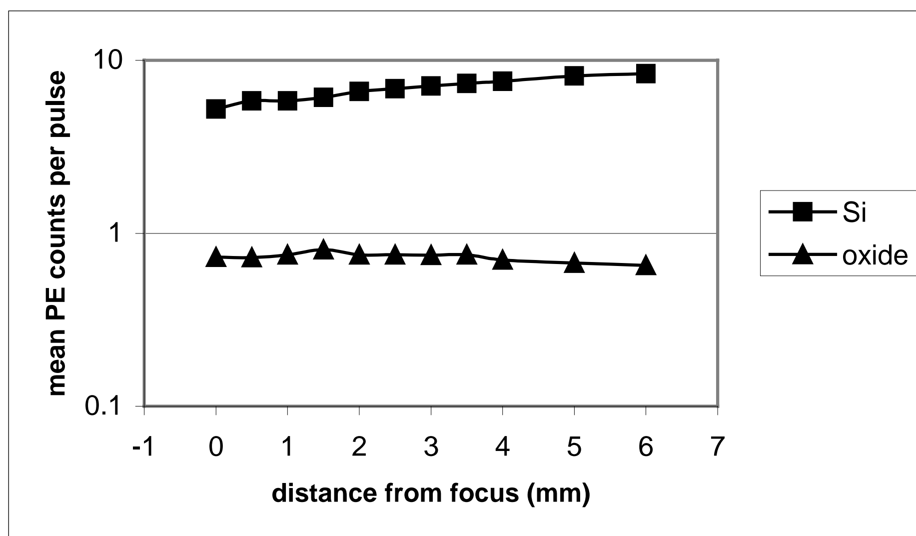

FIG. 50. Si signal and SiO_2 signal vs. distance (0 mm is for the focused beam, with negative numbers indicating a position closer to the sample).

The Si signal behaves much as in the previous experiment, increasing with increasing separation distance. The “oxide” signal however only appears to follow this pattern for a short time and rather weakly at that, and then it begins to wane as the distance increases. This can be easily understood from FIG. 49; the background photoemission from the lens mount falls less directly on the channeltron is it is pulled farther back. This apparently offsets the tendency for the signal to increase from reduced shunting of the sample photocurrent, which has very little influence because of the low signal level from the oxide.

Several methods of reducing this background signal were considered. Biasing the lens mount can either combat the shunting away of the sample photocurrent (if more

negative) or reduce the photoemission from the lens mount (if positive), but the two goals are not very compatible. Changing the mount composition would reduce both effects, but of course this requires manufacturing a new lens mount out of some other material. A simple expedient, for reducing the background at least, is to coat the suspected emissive surfaces with high-vacuum grease, which seems to reduce PE yield by at least a factor of 8, FIG. 51.

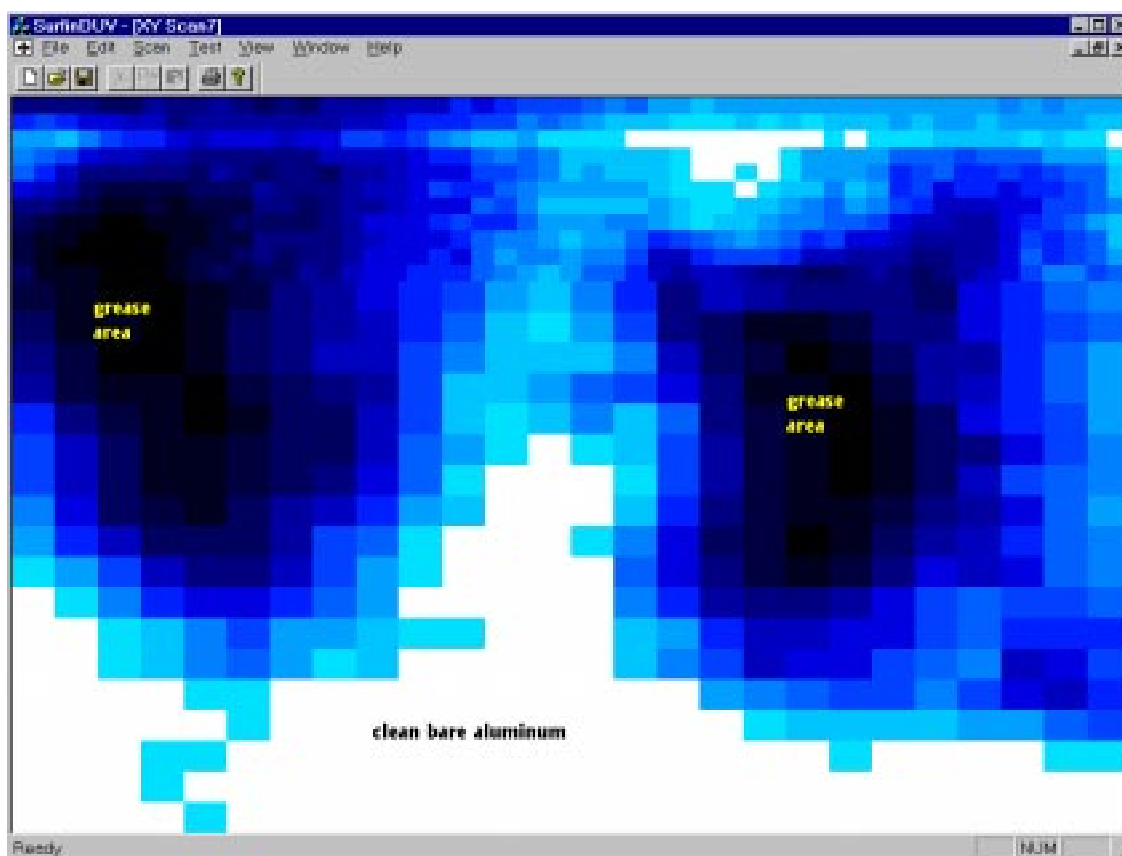

FIG. 51. PE from vacuum grease on clean aluminum.

Most of the emission seen in the grease area (up to a few mm in thickness in the darkest regions) is probably background emission from the lens mount, so the real emission reduction is probably much greater. We may also note here the slight emission

enhancement near the top of the scan, which corresponds to the edge of the aluminum sample.

Coating the lens holding pincers, the nearest exposed metal surface to the beam, however did not appear to reduce the background significantly. This suggests that the background originates from a less obvious component such as the pincer mounts, which may be illuminated by an unexpected reflection.

Focusing was a significant problem as well, since the via array edges are relatively diffuse. With the smaller spot, estimated to be around 40 μm, the depth of focus is only a few tens of micrometers as well, so the focusing procedure, usually a binary search for the optimal focus, can take a number of iterations. Fortunately, there are some very small fiducials present in the oxide field a millimeter or so away from the via areas, and these present good photoemission focusing targets.

On the other hand, getting a sharp focus for the shorter wavelengths required moving the stage closer to the sample so that the via signal starts to drop off for reasons just explained. Thus to get useful signal levels at the most promising wavelengths, the beam had to be left somewhat defocused. Fairly sharp spots in the 40 - 50 μm range were attainable at 230 nm, where the working distance is a few millimeters longer.

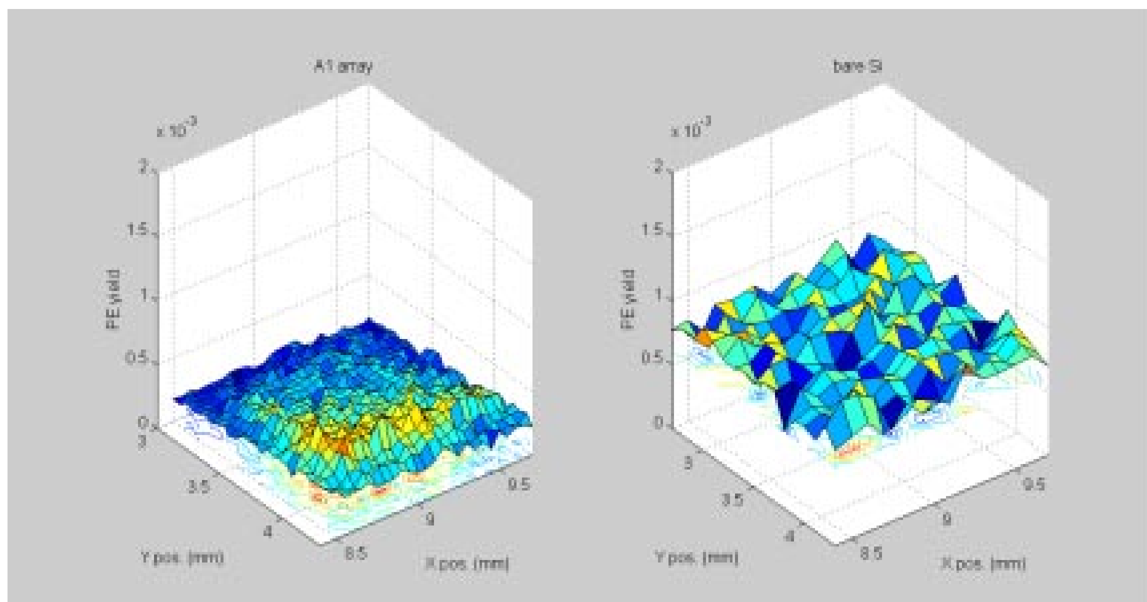

FIG. 52. 160 nm PE yields for via array A1 and bare Si, for second experiment.

FIG. 52 shows calculated photoemission yield for an A1 via area and bare Si at 160 nm. The Si surface is obviously yielding fairly strongly at this wavelength, at just under 10^{-3}. As described, the signal is probably somewhat attenuated by the proximity of the lens mount and the SiO_2 background is probably exaggerated by other background sources.

Because of these difficulties, the second group of photoemission measurements, using the high-power lens, were not as useful as was hoped. Most significantly, no defect area contrast appeared despite the smaller spot size.

A third series of measurements was attempted as well, returning to the 40 mm lens but with a very tight chamber entrance aperture. These produced the data for FIG. 47. However they likewise failed to produce clear evidence of the defect contrast. In this case the beam was rather comatic because of some adjustments made to improve

throughput to compensate for the small aperture, which helped to obscure the defect area. This new configuration, with some further adjustment, shows considerable promise however. The comparative background levels in particular appeared to be reduced, most likely because of the longer working distance. The long working distance combined with the steps taken to improve collection efficiency for the HARI wafer also allowed the acquisition of PE scans at the 130 nm wavelength, which had not been feasible previously.

V. PHOTOEMISSION VOLTAGE CONTRAST MEASUREMENTS

The observation of the photoemission voltage contrast (PEVC) effect has proved, as expected, to be one of the most difficult aspects of the hybrid-emission ultraviolet defect inspection project. Simply obtaining useful samples was somewhat challenging in itself, and a number of background effects have complicated matters.

The major requirement for a good sample to demonstrate PEVC is to have isolated conductive features on a surface, preferably with a low capacitance and a high resistance to ground. The capacitance requirement relates to the charging voltage of the structure, while the resistance determines the rate at which the charge is lost to ground.

The PE rate depends strongly on surface voltage, as seen in FIG. 53, and the surface structure may be modeled as a capacitor with capacitance C_s, so that the voltage is determined by the charge Q_s on the structure. This charge is however a time-varying quantity, initially produced at a rate $I_{PE}(t=0) = I_{PE}(V=0)$ which then decreases as the positive potential on the surface increases. At the same time, this surface potential drives a current I_G to ground through the structure resistance, R_s. This current naturally increases as the surface potential increases. Thus the surface potential is ultimately limited by the loss of charge to ground and the decrease in PE yield. For constant irradiance, this process leads to a constant steady-state surface potential, which can be modeled to some extent, given the PE voltage dependence, C_s, R_s and the incident irradiance.[58] PEVC defect detection in fact aims at finding variations in C_s and R_s, particularly the latter, as might arise in contacts deposited in the under-etched vias seen in

the HARI defect standard of Chapter III. In this respect, PEVC responds to much the same properties as scanning capacitance microscopy.

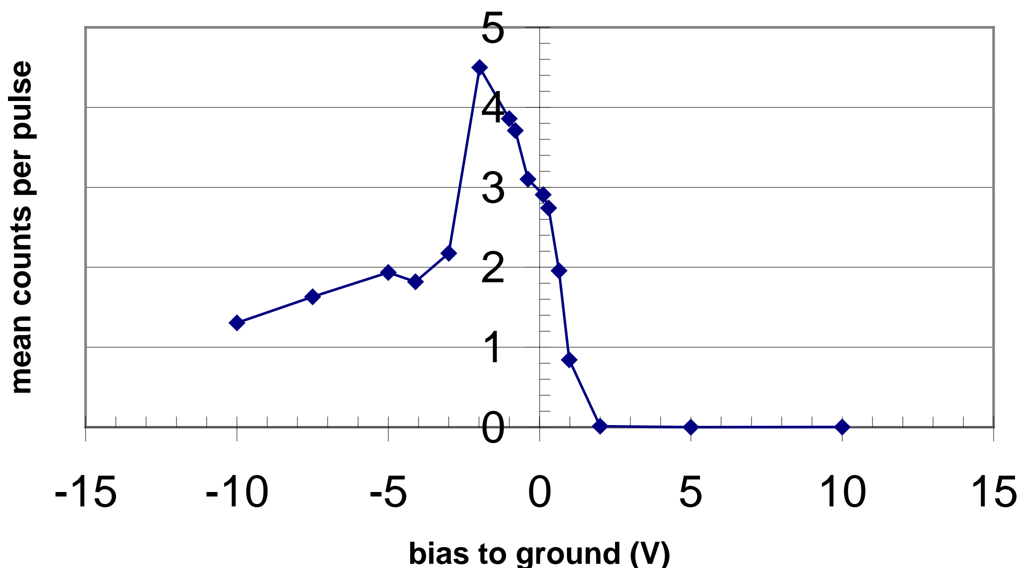

FIG. 53. Chrome photoemission current at 160 nm *vs*. bias voltage. (1 count per pulse represents a current of approximately 0.3 pA in this and subsequent graphs – the incident power and experimental geometry are adjusted to such low levels to avoid saturating the channeltron.)

A reasonable model for this process is a simple RC circuit,[23,59] with a voltage-controlled current source representing the photoemission process connected from the capacitor to ground. Unfortunately, most of the parameters can be difficult to predict so that quantitative modeling is not very useful without a very well characterized structure, but it does allow us to appreciate what sorts of structures are best for demonstrating and observing the effect experimentally, and to qualitatively predict what we should see.

High-RC structures discharge slowly to ground and so will build up the largest (positive) steady-state surface potentials, while low-RC structures will remain near ground potential. This means high-RC structures will tend to be considerably darker in photocurrent than low-RC structures.

In order to demonstrate this effect, we need multiple structures of the same composition (to eliminate material PE contrast) with such an RC difference.

A. First chrome mask

The first attempts to demonstrate PEVC with the HEUDI system used a commercially available resolution target with a chromium pattern, but an undocumented insulating layer (probably an anti-reflection coating) on the surface prevented making controlled electrical contact to the chromium structures and apparently suppressed surface photoemission.

A few attempts with macro-scale capacitor structures, metal plates separated by glass, were made, but leakage current to ground I_G tends to increase with area and photocurrent I_{PE} is approximately constant with area, assuming the emitting structure is larger than the spot size. Because large I_G with relatively small I_{PE} naturally tends to produce very small surface potentials, this approach is unlikely to work, and it did not. Such structures also may be expected to have very large capacitances, so that the relatively small charge built up by photoemission will only lead to negligible surface voltages.

More success was had with a custom-made chrome photomask, fabricated from a “bright” (uncoated) chrome blank. (FIG. 54).

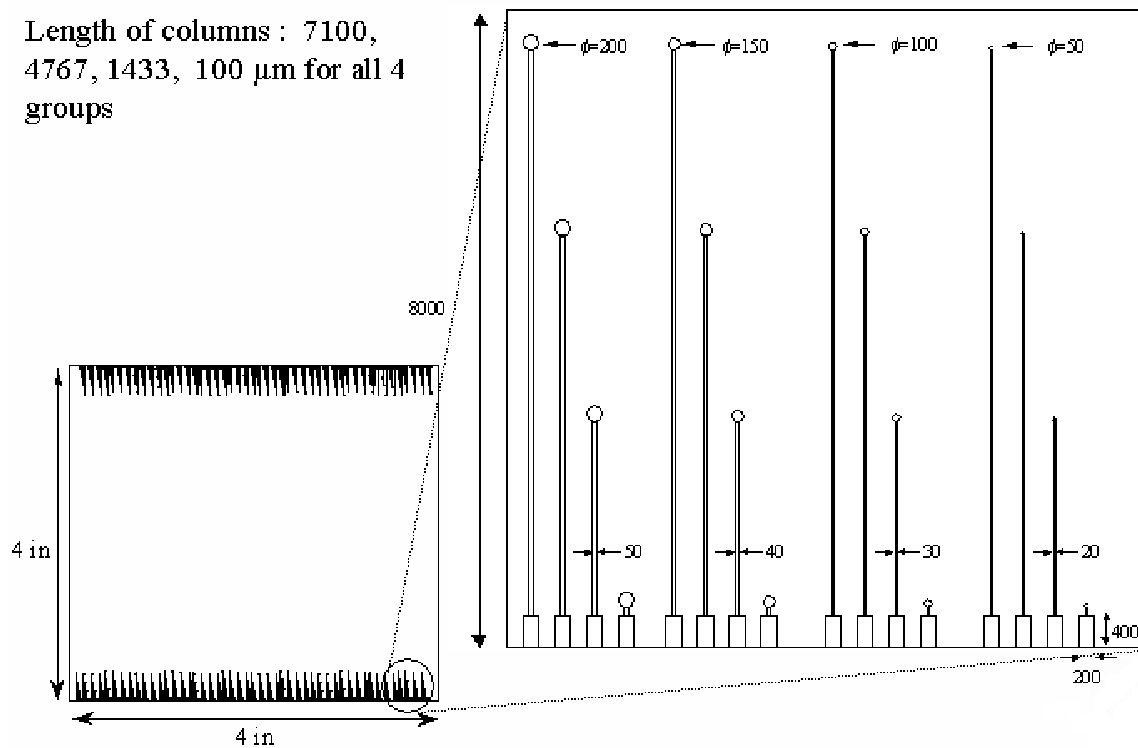

Space between contacts: 200 μm (unspecified units are μm)

FIG. 54. Chrome mask patterned region.

FIG. 55 shows a scan of this pattern, with the chrome strips floating (not connected to a bias potential), with the sample rotated approximately 45° clockwise.

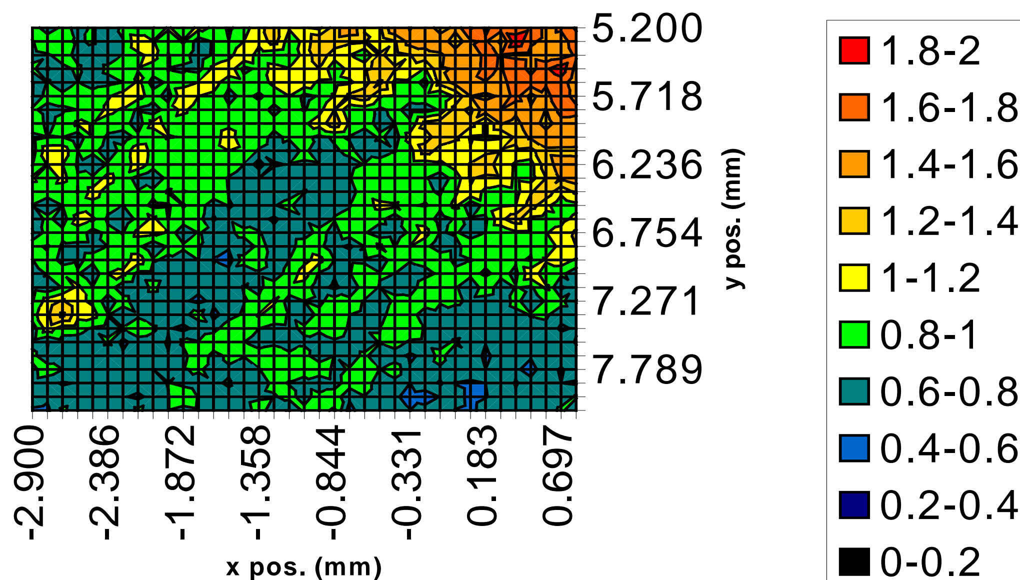

FIG. 55. X-Y map of chrome mask photocurrent with 150 nm illumination (sample rotated about 45°), mean counts per 5 μs pulse.

FIG. 56 shows PE maps of a region on the mask where two large solid chrome areas are separated by the pattern from FIG. 54. In this experiment, the right area was connected to an insulated lead, which connected to a feedthrough, through which various connections could be made from outside the chamber. For the "floating" connection, the lead was left unconnected, while for the "grounded" connection, the feedthrough output was grounded to the chamber body. The left chrome area was grounded to the stage body for both scans.

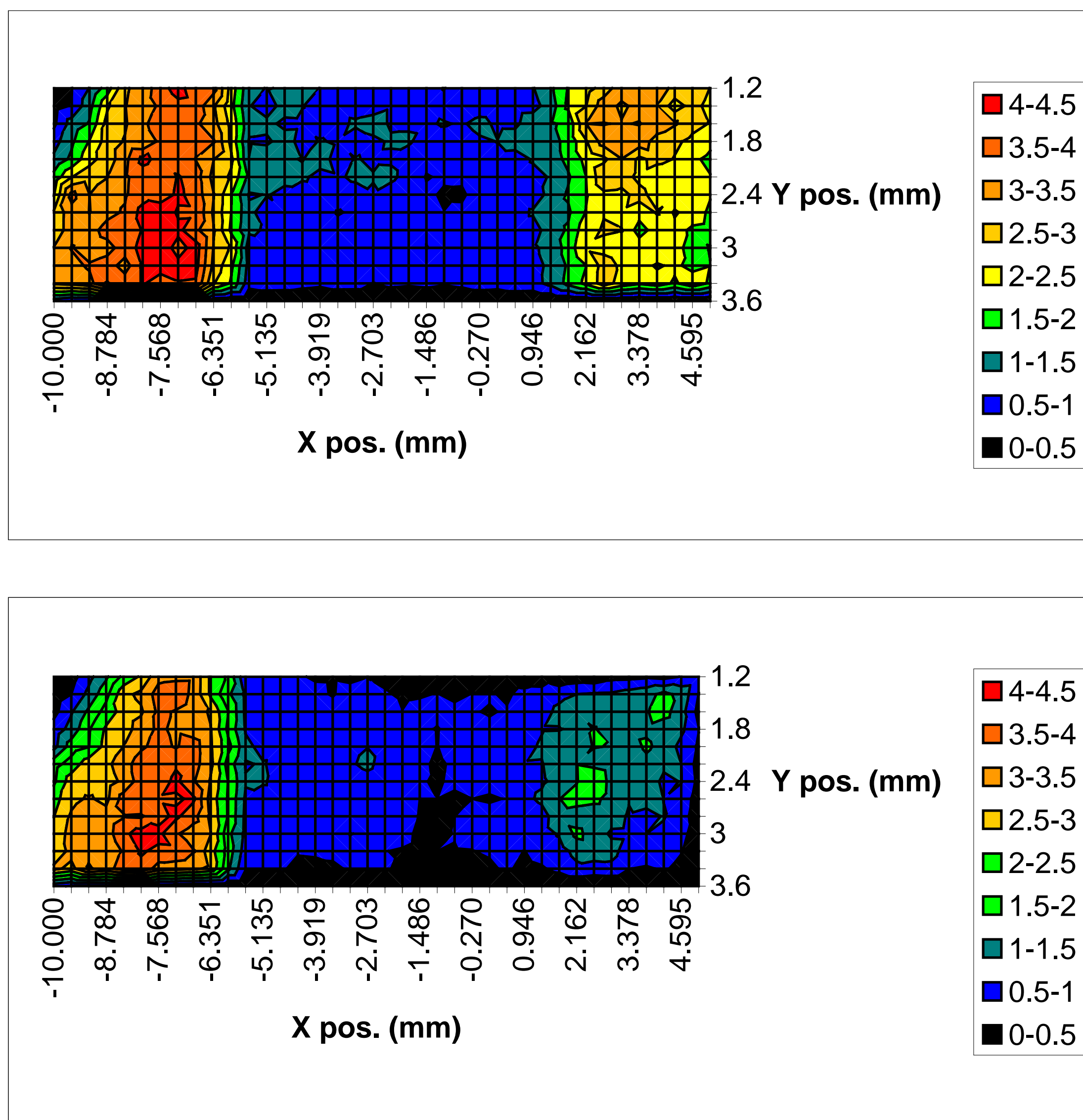

FIG. 56. Chrome mask photocurrent at 160 nm, right chrome area grounded (above) and floating (below). Position in mm, mean counts per 5 μs pulse.

The difference between the two cases is clear. For the grounded case, the right area is quite bright, comparable to the grounded left area. For the floating case, the right area is much dimmer and displays an unusual pattern of emission, probably produced by changes in the charge level as the scan progressed (in this mode, the scans run in a

clockwise spiral pattern). This experiment unequivocally demonstrates spontaneous PE voltage contrast.

The degree of contrast here is of course time varying, though it seems to range from about a factor of 5 to about a factor of 3, for the later stages of scanning. This pattern of variation is somewhat unexpected though, since the floating area should have a more positive potential, retarding the photocurrent. Most likely, this results from some electrostatic steering effect on photoelectrons travelling from the surface to the channeltron. Such effects have been observed with this sample and are discussed later.

This level of contrast would be rather weak for high-speed detection. However, the large chrome areas, which are easier to manipulate experimentally, also have quite large capacitances and probably a much larger ground current than would be typical of a floating microstructure. Because of this, the chrome area used here would be expected to have a low surface potential compared to a typical isolated microstructure.

The contrast between the grounded chrome area and the glass area is also surprisingly low, the experiment seeming to have detected substantial emission from the glass area of the photomask. This emission is typically 1/3 to 1/5 that of the neutral chrome area, which is quite substantial for an insulator. At the 160 nm wavelength, some emission from SiO_2 is to be expected, but it is surprising that the current was so large compared to the chrome photocurrent. There are several possible explanations for this, one being that substantial amounts of stray light or the outer regions of the fairly large illuminating beam might be striking the chrome areas while the central part of the incident beam falls on the glass, perhaps being reflected through the photomask substrate.

Subsequent experiments with the second chrome mask (discussed in the next section) also showed evidence for anomalously high emission for glass near chrome, particularly when the chrome is grounded, which would probably have been enhanced by the large amount of chrome on the first mask. Another possible explanation is background photoemission from exposed metal parts of the apparatus. The likely presence of such background signals would suggest that the voltage contrast is really larger than what has just been estimated.

Further experiments with varying bias voltages for the left chrome area show several important features (FIG. 57). Most strikingly, we find that the PE current over all areas of the sample varies with the bias of the left chrome area. This might at first glance seem odd, but it is a simple consequence of electrostatics. The left chrome area is quite large, so charge distributed across it produces a field extended in space, which seems to steer the photoelectrons emitted from the sample surface. Large biases, either positive or negative, will certainly deflect the photoelectrons away from the channeltron, which also explains the counterintuitive tendency of the right (biased) area's PE current to decrease with large negative bias. In that case, the electric field apparently directs the emitted photoelectrons towards nearby ground potentials rather than toward the positive but more distant channeltron aperture.

The effects of steering for very low biases are less distinct at this point, though it is clear that they should be taken into consideration, and this finding influenced the design of the second chrome mask.

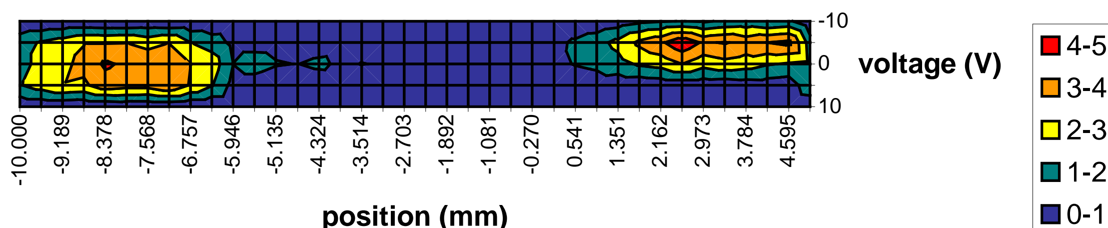

FIG. 57. PE current map for a horizontal strips (at the 2.0 mm vertical position) with varying right-area bias voltages (-10, -1, gnd., +1, +10 V).

FIG. 57 clearly shows that emission from the grounded left area is fairly symmetrical with respect to the sign of the right-area bias, which we would expect if the photocurrent was being shunted between the two chrome areas in the presence of an external bias. The biased right area shows the expected tendency for the PE current to increase as the bias becomes more negative, though somewhere between –1 and –10 V, the biased-area-to-ground fields begin to siphon off photoelectrons.

Since the count rate can be reduced to nearly zero by changing the electrostatic conditions of the sample, these experiments also confirm that the observed channeltron counts are virtually free of photon signal at this wavelength (160 nm). In some circumstances, VUV photons can contribute to the observed count rate, so this observation lends greater confidence to the interpretation of the channeltron signal as being photoelectric in origin.

B. Second chrome mask

A second version of the chrome mask was fabricated with isolated chrome areas, eliminating the large chrome surfaces of the first mask. This change greatly reduces the influence of the steering effects. The new mask also changes the orientation of the strip contacts so that they lie towards the outside of the mask, making it easier to attach external leads. The pattern of the new mask is a mirror image of that on the first as well. Otherwise, the pattern and its dimensions are the same as in the first chrome mask.

In the second mask experiments, the incident beam power for wavelengths longer than 150 nm was measured, allowing the photoemission yields to be calculated per the procedures in the previous chapter. Incident power for the 150 nm and 140 wavelengths was too low to be measured with the calibrated photodiode, but from this we can infer upper limits on these figures which allow us to place lower limits on the photoemission yield (Table 3). 140-150 nm photoemission was often stronger than at much longer wavelengths with far greater incident power, suggesting that at these short wavelengths, the PE yield was quite high, probably as much as 10^{-4} in some portions of the sample.

Table 3. Second mask incident powers and PE yield factors.

Wavelength (nm)	Avg. Pulse Power (W)	PE Yield Factor
140	$<1.54\times10^{-7}$	$>3.69\times10^{-4}$
150	$<1.25\times10^{-7}$	$>4.24\times10^{-4}$
160	4.44×10^{-8}	1.12×10^{-3}
170	1.86×10^{-7}	2.51×10^{-4}
180	4.41×10^{-7}	1.00×10^{-4}
190	1.48×10^{-6}	2.82×10^{-5}
200	6.37×10^{-7}	6.23×10^{-5}
210	3.66×10^{-7}	1.03×10^{-4}
220	3.72×10^{-7}	9.70×10^{-5}
230	2.41×10^{-6}	1.44×10^{-5}

Additionally, a much better focus was obtained, allowing the finer chrome strips to be detected and resolved. FIG. 58 shows a surface plot PE yield between two 50 μm-wide chrome strips separated by 350 μm between their edges. This suggests the effective resolution to be somewhat less than 50 μm at this particular focus. For the longer wavelengths, the more powerful fused-silica lens could be used, but the short-working-distance mount tends to interfere with the channeltron, as discussed in Chapter IV.

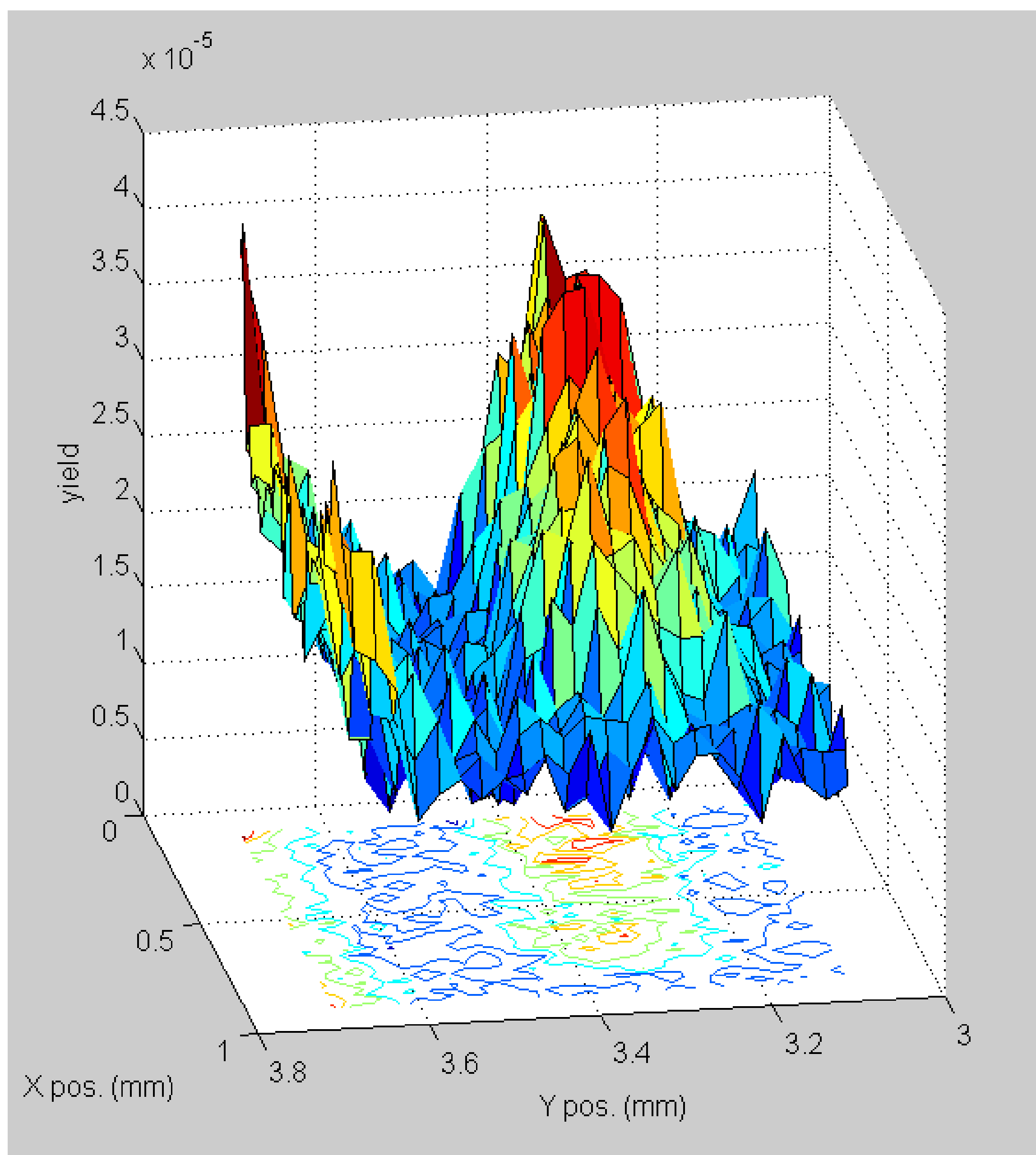

FIG. 58. 190 nm PE scan of area between two 50 um-wide grounded chrome strips.

During the investigation of the second chrome mask, the deflection filter (described in Chapter IV) was mounted on the channeltron to make sure pulses detected from the glass regions were not photon originated. This had been a concern, since the

glass emission levels increased with shorter wavelength, a behavior that might be expected since the channeltron's photon sensitivity increases rapidly below 180 nm. However a range of scans taken with small and large filter voltages indicates that most of the measured pulses in both the metallic and glass regions are indeed photoelectrons (FIG. 59).

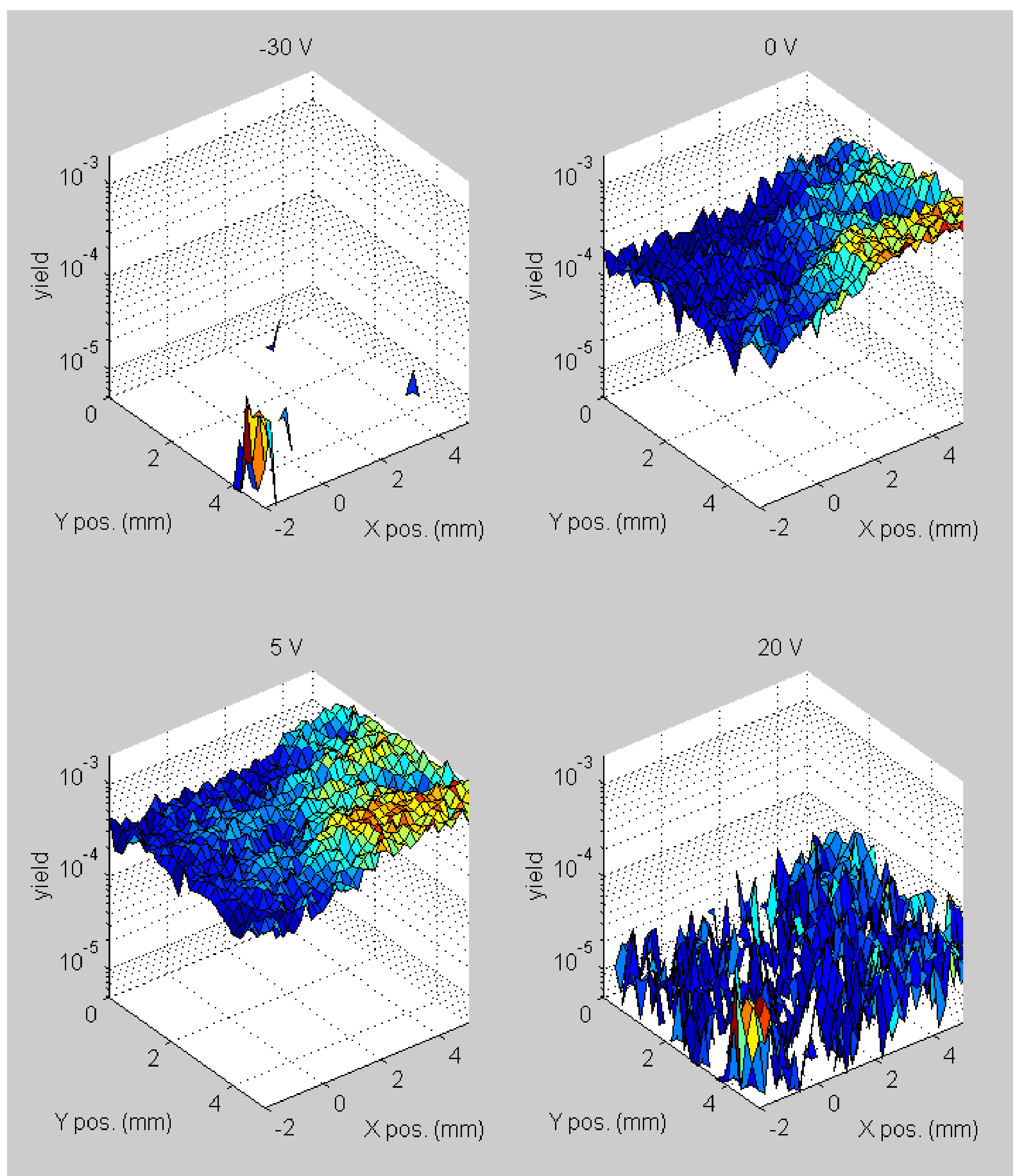

FIG. 59. Strips and background at various filter voltages (160 nm illumination).

These measurements also show an interesting tendency for certain voltages, -30 V in particular, to selectively emphasize the aluminum contact (roughly located at (5, -2),

the corner facing the reader). This selectivity probably arises from the energy dependence of deflection of the PE current flowing through the deflection filter (more energetic electrons experience less deflection). Surfaces of different composition usually have different work functions and thus the emitted photoelectrons have different energy distributions. It is however a fairly minor effect with this filter, which was not designed specifically for energy selection.

FIG. 60 shows a PE scan of the strips connected to a -0.73 V potential with 190 nm illumination.

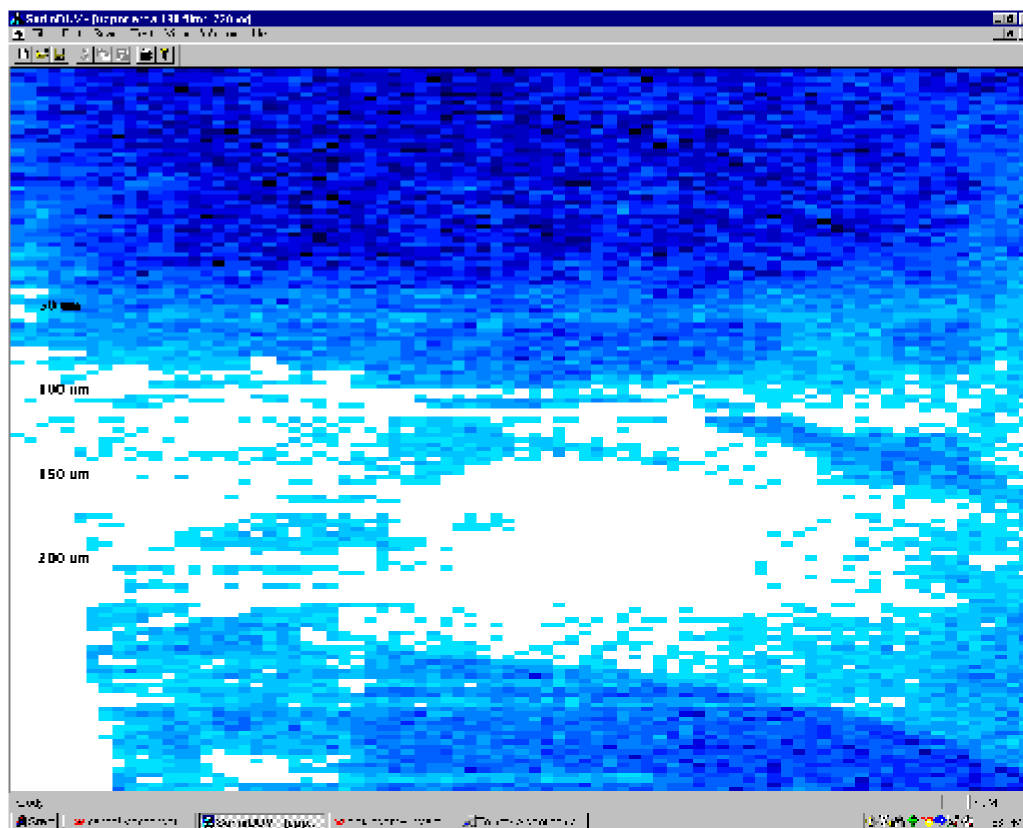

FIG. 60. 190 nm scan of strips at -0.73 V potential (area 8 mm wide by 5 mm high).

The contrast between the floating strips and the negative strips (center three sets labeled “100 µm,” “150 µm,” and “200 µm”) is strong. A bright “flare” of emission can also be seen spreading out toward the right of the image. The exact nature of this flare is uncertain, though similar features have been observed in other observations with the strips grounded or negatively biased. This emission perhaps represents regions where surface currents act to discharge the SiO_2 and thus enhance its emission levels. While this wavelength is too long (in theory) to give significant photoemission from SiO_2 or to promote carriers over the bandgap, its 6.5 eV energy might be sufficient to promote carriers from the numerous interband states found in typical amorphous SiO_2 samples, especially those in which trace impurities have not been intentionally controlled.

Supporting this idea is the fact that this “flare” feature disappears at longer wavelengths (becoming virtually undetectable at 230 nm) and becomes much stronger relative to the chrome emission at shorter wavelengths. Against this idea is the short lifetime expected of such carriers in a largely amorphous material, which would limit their ability to aid in neutralizing the surface charge.

There are also a few isolated features of uncertain nature. These are suspected to be surface contaminants left from the placing of the aluminum contact.

The presence of the contact may also have some effect of the measured emission. Looking closely at the scan, it may be observed that several groups of strips apart from the three electrically connected groups seem to show enhanced emission compared to the top two groups, which are all but invisible. These medium-bright groups happen to lie at the same height as the aluminum contact, the point of which rests on the pads of the three

very bright electrically connected central groups. Thus it appears that the nearby presence of the contact itself alters apparent emission levels somewhat, possibly via the steering effects discussed earlier.

Because of this, a different contact method was tried for the next experiments. To reduce the size and possible influence of the contact, the biasing lead was connected to the strip pads with colloidal silver paste (unheated), which is often used in electron microscopy for similar purposes.

Using this silver paste contact, a pair of chrome strips not connected to the contact were scanned while varying voltages were applied to the contact. FIG. 61 shows a surface/contour plot of yields along the Y direction at a fixed X coordinate. The strips run in the X direction and so the Y-sections cut through them.

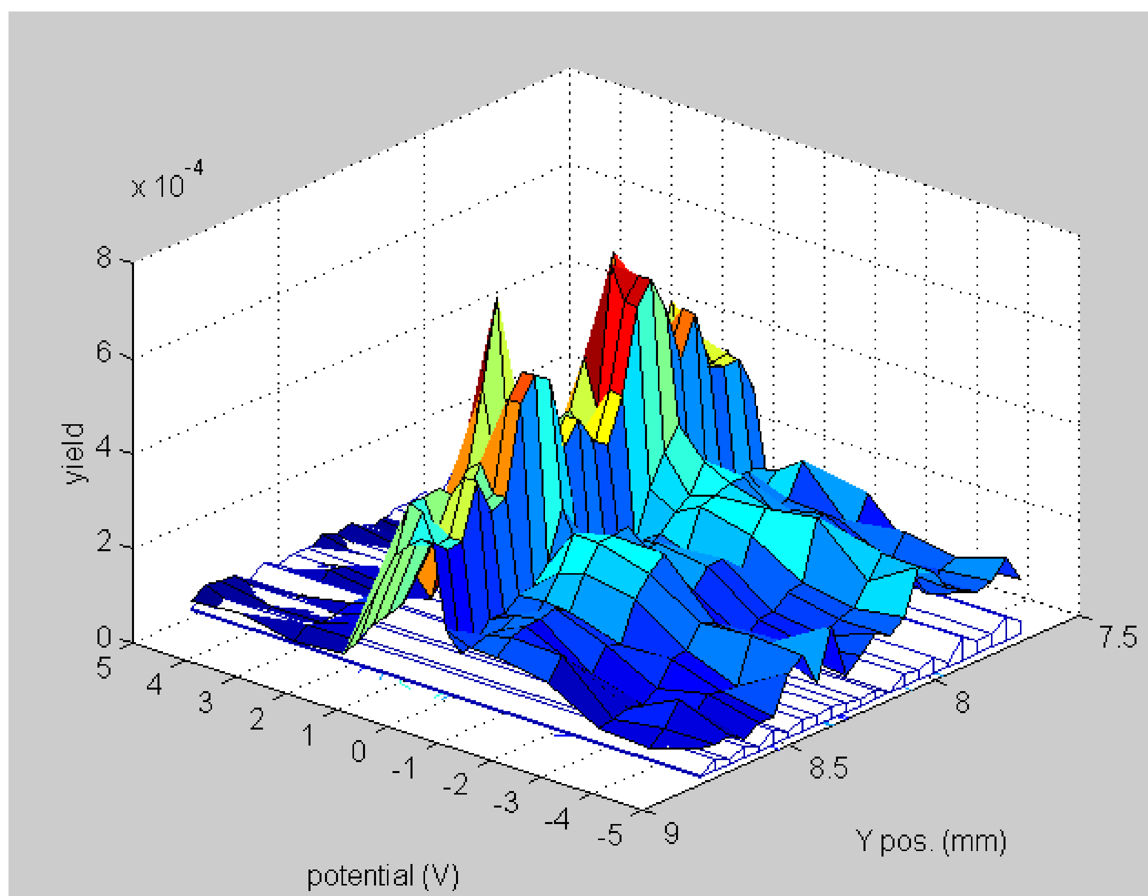

FIG. 61. Chrome strips with varying contact potentials at 140 nm.

The floating-contact emission was measured as well and appears as the white mesh plot underlying the controlled-voltage surface plot. This would seem to indicate that this effect is produced either by the contact, which in this case was 6 mm away and only around 3 mm × 4 mm in area, or by the adjacent chrome strips.

The "flare" around the grounded chrome strips seen in the last experiment was strongly in evidence once again as well. Since this flare area was quite large in extent, covering perhaps 10 times the area of the contact itself and much closer to the pair of voltage-varied strips than the contact was, the influence of this region is most likely to

explain the emission variation. Supporting this idea, scans around the contact itself showed that varying the voltage from ground to –4.37 V had no measurable effect on the emission from the glass area a mere 200 μm from the contact but quintupled the emission from the contact itself.

It remains though to determine why the flare area has this effect. The two clear possible mechanisms are photoelectron steering and surface conduction. Steering is fairly easy to rule out, since the steering effect would be expected to be noticeable around the contact, which is merely the left edge of the flare area. Other facts to note are that the glass surface emission around the strips is enhanced (very unlikely to result from steering) and that the form of voltage-emission curve strongly resembles the curves of FIG. 53 and the right side of FIG. 57, although shifted a few volts toward the positive direction.

These observations would be consistent with the idea that the surface is offering a weak conduction path in the flare area, so that the voltage-varied chrome strips are electrically connected to the contact through a resistance small enough that the strips no longer behave as if they are insulated.

Neither explanation for the emission variation though quite explains why it peaks at a slight positive voltage. The peak emission has been frequently observed to occur, for reasons unclear, at small negative voltages, falling off at large negative voltages. In this case, the peak simply appears to have been shifted a few volts in the positive direction, so the phenomena seem to interact somehow.

The flare feature was also observed around a second contact and set of chrome strips in subsequent experiments, so this appears to be a repeatable phenomenon for this chrome-on-glass mask.

It should be noted as well that the 140 nm incident beam was so weak that it could not be measured by the photodiode, so the yield values in FIG. 61 represent a minimum yield. The true yields are likely to have been as much as a decade higher.

VI. SUMMARY AND CONCLUSIONS

A. Experimental topics

The project has succeeded in constructing a dual-purpose scanning DUV scatterometer and photoemission apparatus. In some respects the instrument has met or exceeded expectations, particularly in its speed and throughput. However, spot-size and thus spatial resolution limit are still about 4 - 5 times larger than desired, which has created some difficulties with certain experiments. This problem arises from the nature of the light source used, but it can be resolved for future work at the expense of throughput with some redesign of the optics, particularly the introduction of a smaller aperture in the optical train. This will require some mechanical ingenuity, but it is feasible.

The construction of the system in itself provided a wealth of useful information which can now be used to inform the design and construction of similar systems.

The next three sections will summarize the conclusions for each major experimental topic.

1. Scattering

The DUV scattering experiments have yielded some interesting results with the high aspect ratio sample. However, the particle scattering measurements have had little success. Several difficulties have plagued the particle scatterometry experiments, firstly that the converged spot from the Xe lamp source has not achieved spot sizes as small

(and intense) as would be necessary for the detection of scattering by individual nanoparticles, which were a primary interest of the project. Secondly, the standard polystyrene latex particles used in visible-light scatterometry appear to scatter far less effectively than expected at DUV wavelengths. It is suspected that the optical properties of PSL differ considerably from the values that were estimated in preliminary modeling. Efforts are underway to determine the true DUV optical properties of PSL spheres, though the data have not yet been obtained. Standard particles of a different composition, mostly likely of some metal or silica, are a logical alternative.

While the HARI wafer measurements did reveal some interesting features, the system was unable to detect scattering contrast from the defects in the A1 via region in any of the experimental configurations. Unfortunately, the most likely angles for detection, near normal incidence, produced no strong scattering signals which could be compared between different X-Y positions. Further modification of the instrument might eventually allow this, particularly a smaller minimum spot size or a maximum scan angle closer to the incident beam direction. It is clear though that *s*-polarized light gives stronger scattering from the vias, and so this is the most likely mode to detect the via defects. The *s*-polarization though does have some disadvantages in that it seems to admit more oxide background scattering features (to be expected from the theory of roughness scattering), which are in some cases not stationary with respect to the wafer surface.

2. Photoemission

A significant finding of the photoemission project was that DUV-stimulated photoemission yields from common semiconductor materials are in line with the expectations that motivated the project. In some cases, PE yields as high as 2×10^{-3} have been seen, and yields in the range 10^{-4}-10^{-5} are routinely encountered.

In addition to the expected findings, an unusual effect has been observed in photoemission from insulating SiO_2 with conducting strips on the surface. This apparent effect gives regions of enhanced photoemission from the oxide surface around metal films, particularly grounded films. The effect perhaps results from generation of excess carriers in the oxide by absorption of DUV light and thus the conduction of current over the oxide surface, reducing the charging effect and thus enhancing photocurrent. However, the expected short lifetime of such carriers makes this explanation at least uncertain.

This enhanced oxide emission can have both positive and negative consequences for photoemission inspection. On one hand, it tends to obscure metallic patterns against the surrounding oxide emission, but on the other hand, it makes the presence of a grounded conductor quite evident, enhancing the apparent voltage contrast.

3. Photoemission voltage contrast

The PEVC portion of the project has had fairly positive results, chiefly showing that:

- Voltage-contrast surface inspection may be performed with DUV light at modest vacuum levels (apparently limited only by photoelectron mean free path).
- Voltage contrast can be as much as a factor of 10, and probably can be shown to be much greater with the elimination of background influences.

B. Implications for practical DUV inspection

Given these results, we can now more confidently analyze the potential of DUV inspection as a tool for semiconductor yield management.

The first conclusion is that DUV scattering in general is not as attractive as was suggested by models at the outset, though the lack of clear experimental data for small particles still leaves this uncertain. The HEUDI apparatus should however be capable of addressing this uncertainty with some future modifications.

Photoemission on the contrary has turned out to be quite promising. Of most interest are the distinct electrical effects that have been observed. Though some aspects of these effects are not fully understood, it is clear that photoemission inspection is capable of detecting non-topographic electrical qualities, which are of course the physical data that optical topographic inspection modes frequently aspire to infer. Photoemission is also naturally capable of the same scanning resolution as optical techniques, and, although this technique was not applied in the present work, imaged photoelectrons can even give resolutions approaching those found in electron microscopy.

This work has also addressed several major concerns with the practicality of this technique, showing that DUV-stimulated photoelectron yields are well within the levels required for high-speed scanning. With emitted electron fluxes only three decades or less

below the incident photon flux, photoemission stimulated by available laser sources, as discussed in Chapter I, should allow hour-per-wafer scan rates. Although DUV optical inspection does not seem to have a clear advantage over visible inspection, neither does it seem to be inferior. If the two techniques are coupled such that only selected appropriate areas are subject to the slower photoemission inspection mode, this hybrid photoemission/scattering technique could conceivably be only slightly slower than present day visible-light inspection technologies.

This work has also shown that easily obtainable industrial vacuum levels are entirely adequate to this application, and solutions to problems likely to be encountered with inspection *in vacuo* have been developed.

Even the mirror-fouling experiments, while they have not yet succeeded in showing how to prevent fouling, suggest that the DUV-stimulated carbon deposition rate is low enough such that it only poses problems with source optics and is unlikely to be a serious surface contamination concern.

C. FUTURE WORK

A number of future avenues of research are suggested by the foregoing results. On the light-scattering side, a brighter source would certainly improve the likelihood of getting good measurements of scattering by small particles. Commercially available DUV excimer lasers have improved considerably in just the past few years since the beginning of the project, and any of the commonly available 157 nm (F-F), 193 nm (Ar-F), or 248 nm (Kr-F) excimer wavelengths would work well experimentally as well as for

possible industrial inspection systems based on this technology. The HEUDI data collection system is already designed for pulse-mode data acquisition, so the most commonly available pulsed forms of such lasers could be connected to the system fairly easily.

Other potential applications for DUV scattering might be explored as well, such as critical-dimension (CD) measurement and evaluation of roughness scatter for DUV lithographic optics.

For photoemission, there are several interesting new topics to be explored. Chapter IV has already discussed ways to proceed with investigations of unwanted carbon deposition and its control. This phenomenon also has a number of interesting possible implications. For one, optically controlled carbon deposition might have some applications in the area of carbon nanotubes, allowing optical pattering of nanotube growth, which is a rather random affair by current methods. Optically controlled growth of graphitic carbon films in general might find some useful applications.

Another possibility is that use of near-field VUV probes in combination with bright excimer laser sources could allow sub-wavelength high-resolution photoemission microscopy (or even spectromicroscopy, in which photoelectron energy distribution is observed), a technique which has only been demonstrated with synchrotron sources. Smith *et al.*[60] have already treated the use of silica capillary tubes as scanning near-field optical microscopy (SNOM) probes for the 10 - 200 eV photon energy range, but it is certainly conceivable that transmissive fluoride fibers could be used for energies up to about 10 eV (the approximate transmission cutoff for fluoride transmission). The

advantage of fibers over capillaries is of course that fibers can have total internal reflection in the VUV range, which can make them more efficient for transporting light than capillaries.

Indeed, given the amount of recent literature on photoemission cited throughout this work, it seems that there are many aspects of photoemission which could be applied with excimer DUV/VUV sources as an alternative to the expensive institutional synchrotron sources which are conventionally used.

REFERENCES

[1] L. Reimer, *Scanning Electron Microscopy: physics of image formation and microanalysis*, (Springer, New York, 1985).

[2] B. D. Buckner, L. Suresh, and E. D. Hirleman, in *SPIE Vol. 3275, Flatness, Roughness, and Discrete Defect Characterization for Computer Disks, Wafers, and Flat Panel Displays II*, edited by J.C. Stover, (SPIE, Bellingham, WA, 1998), pp. 90-101.

[3] S. Stokowski and M. Vaez-Iravani, in *Characterization and Metrology for ULSI Technology: 1998 International Conference*, edited by D.G. Seiler (AIP, Woodbury, NY, 1998), pp. 349-359.

[4] M.Kurz, A. D'Anna, A. D'Alessio, S.S. Mereola, and A. Borghese, "UV-broadband light scattering measurements during metallic particle formation in a combustion-like environment," Part. Part. Syst. Charac. **16**, pp. 77-84, (1999).

[5] S.S. Mereola, B.M. Vaglieco, S. Consales, F.E. Corcione, and G. Formisano, "Determination of size of fuel droplets and soot particles in a diesel engine by broadband extinction and scattering spectroscopy," Part. Part. Syst. Charac. **18**, pp. 235-242, (2001).

[6] J. Ferré-Borrull, A. Duparré, and E. Quesnel, "Roughness and light scattering of ion-beam-sputtered fluoride coatings for 193 nm", App. Optics **39**, pp. 5854-5864, (2000).

[7] Y. Liu and Futian Li, "Characteristics of various diffuser materials at UV-VUV spectral range," Acta Optica Sinica **21**, pp. 371-275, (2001).

[8] V. Liberman, T.M. Bloomstein, and M. Rothschild, in *SPIE Vol. 3998, Metrology, Inspection, and Process Control for Microlithography XIV*, (SPIE, Bellingham, WA, 2000), pp. 480-491.

[9] W. Viehmann and R.E. Predmore, in *SPIE Vol. 675, Stray Radiation V*, (SPIE, Bellingham, WA, 1987), pp. 67-72.

[10] J.C. Stover, *Optical Scattering: Measurement and Analysis*, (SPIE Optical Engineering Press, Bellingham, WA, 1995).

[11] H.H. Rotermund, G. Ertl, and W. Sesselmann, "Scanning photoemission microscopy of surfaces," Surface Sci. **217**, pp. L383-L390, (1989).

[12] G. Magaritondo and F. Cerrina, "Overview of soft-X-ray photoemission spectromicroscopy," Nucl. Instrum. Methods A **291**, pp. 26-35, (1990).

[13] H. Ade, J. Kirz, S.L. Hulbert, E.D. Johnson, E. Anderson, and D. Kern, "X-ray spectromicroscopy with a zone plate generated microprobe," Appl. Phys. Let. **56**, pp. 1841-1843, (1990).

[14] R. Nyholm, M. Eriksson, K. Hansen, O-P. Sairanen,, S. Werin, A. Flodström, C. Törnevik, T. Meinander, and M. Sarakontu, "Submicrometer-resolution photoelectron spectroscopy at MAX Lab," Rev. Sci. Instrum. **60**, pp. 2168-2171, (1989).

[15] H.H. Rotermund, S. Jakubith, S. Kubala, A. von Oertzen, and G. Ertl, "Investigation of surfaces by scanning photoemission microscopy," J. Electron Spectrosc. Relat. Phenom. **52**, pp. 811-819, (1990).

[16] J. Westhof, G. Meister, F. Lodders, R. Matzdorf, R. Henning, E. Janssen, and A. Goldmann, "UV-photoelectron spectroscopy with lateral resolution," Appl. Phys. A **53**, pp. 410-413, (1991).

[17] A.W. Potts, S. Anjum, R.E. Burge, A.D. Tournas, and A. Yacoot, "A scanning UV photoemission microscope," J. Electron Spectrosc. Relat. Phenom. **24**, pp. 27-41, (1992).

[18] F. Barbo, M. Bertolo, A. Bianco, G. Cautero, S. Fontana, T.K. Johal, S. La Rosa, G. Magaritondo, and K. Kaznacheyev, "Spectromicroscopy beamline at ELETTRA: Performances achieved at the end of commissioning," Rev. Sci. Instrum. **71**, pp. 5-9, (2000).

[19] P.A. Bionda, M.S. Thesis, Arizona State University, 1998.

[20] C. Girard, C. Joachim, and S. Gauthier, "The physics of the near field," Rep. Prog. Phys. **63**, pp. 893-938, (2000).

[21] C.F. Bohren and D.R. Huffman, *Absorption and Scattering of Light by Small Particles*, (Wiley-Interscience, New York, 1983), p. 212.

[22] E. Brüche, "Elektronenmikroskopische abbildung mit lichtelektrischen elektronen," Z. Phys **86**, pp. 448-450, (1933).

[23] S. Günther, A. Kolmakov, J. Kovac, and M. Kiskinova, "Artefact formation in scanning photoelectron emission microscopy," Ultramicroscopy **75**, pp. 35-51, (1998).

[24] B. Feuerbacher, B. Fitton, and R.F. Willis, in *Photoemission and the Electronic Properties of Surfaces*, edited by B. Feuerbacher, B. Fitton, and R.F. Willis, (Wiley, New York, 1978), p. 12.

[25] M. Cardona and L. Ley, in *Photoemission in Solids I*, (Springer, New York, 1978), p. 49.

[26] V.I. Vedeneyev, L.V. Gurvich, V.N. Kondrat'yev, V.A. Medvedev, and Ye.L. Frankevich, *Bond Energies, Ionization Potentials and Electron Affinities*, (St. Martin's , New York, 1966), p. 182.

[27] S. Arnold in *Optical Effects Associated with Small Particles*, edited by P.W. Barber and R.K. Chang, (World Scientific, New Jersey, 1988), p.82.

[28] R. Schmehl, B.M. Nebeker, and E.D. Hirleman, “Discrete-dipole approximation for scattering by features on surfaces by means of a two-dimensional fast Fourier transform,” J. Opt. Soc. Am. A**14**, pp. 3026-36, (1997).

[29] R.M. Fowler, “The photoelectric sensitivity curves for clean metals at various temperatures,” Phys. Rev. **38**, pp. 45-56, (1931).

[30] E.O. Kane, “Theory of photoelectric emission from semiconductors,” Phys. Rev. **127**, pp. 131-141, (1962).

[31] R. Suhrmann, in *Der Lichtelektrische Effekt und Seine Anwendungen*, edited by H. Simon and R. Suhrmann, (Springer, Berlin, 1958), p. 11.

[32] J.H. Thomas III, “Transient photodepopulation measurements of electron trap distributions in thin SiO_2 films on silicon,” J. App. Phys. **44**, pp. 811-814, (1973).

[33] H.C. Pfeiffer, “Contactless electrical testing with multiple electron beams,” Scanning Electron Microscopy **1982/II**, pp. 581-589, (1982).

[34] H.C. Pfeiffer, G.O. Langner, W. Stickel, and R.A. Simpson, “Contactless electrical testing of large area specimens using electron beams,” J. Vac. Sci. Technol. **19**, pp. 1014-1018, (1981).

[35] H. Beha, H. Seitz, A. Blacha, and R. Clauberg, “Photoemission sampling technique for high-speed integrated circuit testing,” Microelectronic Engineering **7**, pp. 351-359, (1987).

[36] "Meeting Minutes for the SEMATECH e-Beam Based Patterned Wafer Defect Detection Workshop", edited by V.S. Sankaran, 1999 (unpublished).

[37] D.N. Nikogosyan, *Properties of Optical and Laser Related Materials*, (Wiley, New York, 1997), p. 98.

[38] B.D. Buckner, M.S. thesis, Arizona State University, 1996.

[39] M. Lukiesh, *Ultraviolet Radiation*, (Van Nostrand, New York, 1922), p. 36.

[40] G.L. Weissler, P. Lee, and E.I. Mohr, “Absolute absorption coefficients for nitrogen in vacuum ultraviolet,” J. Opt. Soc. Amer. **42**, pp. 84-90, (1951).

[41] J.M. Bennett and H.E. Bennett, in the *Handbook of Optics*, edited by W.G. Driscoll and W. Vaughan, (McGraw-Hill, New York, 1978), p. 10-59.

[42] Crystran Optics. (2001, Aug. 5). Magnesium Fluoride (MgF2) Data Sheet. http://www.crystran.co.uk/mgf2data.htm (27 Apr. 2002).

[43] Crystran Optics. (2001, Nov. 13). Silica Glass (SiO2) Data Sheet. http://www.crystran.co.uk/siof2data.htm (27 Apr. 2002).

[44] D.C. O'Shea, *Elements of Modern Optics Design*, p. 257, New York: Wiley, 1985.

[45] E. Hecht, *Optics*, 2nd. Ed. (Addison-Wesley, Reading, MA, 1989), p.214.

[46] F.E. Nicodemus, "Reflectance nomenclature and directional reflectance and emissivity," App. Optics **9**, pp. 1474-1475, (1970).

[47] F.E. Nicodemus, J.C. Richmond, J.J. Hsia, I.W. Ginsberg, T. Limperis, *Geometric Considerations and Nomenclature for Reflectance: NBS Monograph 160*, (US Dept. of Commerce, Washington, DC, 1977).

[48] G.W. Starr, Ph.D. thesis, Arizona State University, 1997.

[49] Y. Nakai, K. Matsuda, T. Takagaki, and T. Ideta in *3rd International Conference on Vacuum Ultra-Violet Radiation Physics*, edited by Y. Nakai (Physical Society of Japan, Tokyo, 1971), p. 31pA2-6 (1) (Abstract only).

[50] A.C. Fozza, J.E. Klemberg-Sapieha, and M.R. Wertheimer, "Vacuum ultraviolet irradiation of polymers," Plasmas and Polymers **4**, pp. 183-206, (1999).

[51] D.F. Edwards in *Handbook of Optical Constants of Solids III*, edited by E. Palik, (Academic Press, San Diego, 1985), pp. 558-535.

[52] H.R. Philipp in *Handbook of Optical Constants of Solids III*, edited by E. Palik, (Academic Press, San Diego, 1985), pp. 758-760.

[53] G. Pashman, E.G. Shelley, C.R. Chappell, R.D. Sharp, and L.F. Smith, "Absolute efficiency measurements for channel electron multipliers utilizing a unique electron source," Rev. Sci. Instr., **41**, 1706-1711 (1970).

[54] K. Boller, R-P. Haelbich, H. Hogrefe, W. Jark, and C. Kunz, "Investigation of carbon contamination of mirror surfaces exposed to synchrotron radiation," Nucl. Instrum. Methods **208**, pp. 273-279, (1983).

[55] T. Koide, S. Sato, T. Shidara, M. Niwano, M. Yanagihara, A. Yamada, A. Fujimori, A. Mikuni, H. Kato, and T. Miyahara, "Investigation of carbon contamination of synchrotron radiation mirrors," Nucl. Instrum. Methods A **246**, pp. 215-218, (1986).

[56] T. Koide, M. Yanagihara, Y. Aiura, S. Sato, T. Shidara, M. Niwano, A. Fujimori, H. Fukutani, M. Niwano, and H. Kato, "Resuscitation of carbon-contaminated mirrors and

gratings by oxygen-discharge cleaning. 1: Efficency recovery in the 4-40 eV range," App. Optics **26**, pp. 3884-3894, (1987).

[57] C. Girard, C. Joachim, and S. Gauthier, "The physics of the near field," Rep. Prog. Phys. **63**, pp. 893-938, (2000).

[58] T.J. Shaffner and R.D. Van Veld, "'Charging' effects in the scanning electron microscope," J. Phys. E**4**, pp. 633-637, (1971).

[59] T.C. Sheu, M.S. thesis, Arizona State University, 1987.

[60] N.V. Smith, W.A. Royer, and J.E. Rowe, "Channeling of vacuum ultraviolet radiation down tapered capillaries and prospects for a photoemission spectromicroscopy," Rev. Sci. Instrum. **65**, pp. 1954-1958, (1994).

APPENDIX I

SURFINDUV FILE FORMATS

SurfinDUV has two data file formats, one for X-Y scan files (.XY) and one for angle scan files (.ANG). Additionally, several functions produce simple columnar comma separated variable (CSV) outputs, but these are only used for diagnostics and calibration experiments.

Columnar fields in both .XY and .ANG files are separated by commas in plain-text ASCII files, the standard CSV format.

A. X-Y Scans

X-Y scan files are designed to store gated integrator output voltages at a range of stage positions and contain information on the experimental setup used to gather the data.

The first line always begins with the tag *SurfinDUV*, which may be followed by a time and date indicating the time and date of the original scan (the time and date stamps of the file may not correspond to the scan time).

The second line may contain one of three possible tags, *XYScan*, *XYSurfScan*, or *XYSpiral*. *XYScan* indicates a step-mode scan, in which one or more samples are acquired per point with the motors stopping at each position. In this mode, the scan rasters in the X direction. *XYSurfScan* indicates a "surf-mode" scan, in which single samples are acquired while the motors are moving, allows high scan speeds but limiting positional accuracy. With *XYSurfScan*, the raster direction is whichever direction has the highest linear density of samples, with the X direction taking priority if the densities are equal. *XYSpiral* is a step-mode scan like *XYScan*, allowing multiple samples per position, but it translates the motors in a spiral pattern to control motor heating. The spiral scan always begins by rastering in the X direction.

Line 3 contains the header for the scan setup data, *Angle*, *X start*, *X end*, *X steps*, *Y start*, *Y end*, *Y steps*, *subtracted background*, and *number of samples*.

Table 4. XY file, line 3 field headers.

Field	Description
angle	The angle at which the scan was performed (see Chapter I). For coordinate system).
X start	The starting X position of the scan.
X end	The final X position of the scan.
X steps	The number of steps in the X direction. Step size =(X end - X start)/(X steps-1)
Y start	The starting Y position of the scan.
Y end	The final X position of the scan.
Y steps	The number of steps in the Y direction. Step size =(Y end - Y start)/(Y steps-1)
subtracted background	System dark background averaged over 10 samples, which is subtracted from all data readings. This is obtained by firing data acquisition pulses with the lamp off.
number of samples	The number of samples averaged per X-Y position.

Line 4 contains the values corresponding to the headers in line 3.

Line 5 contains the heads for the array of scan data, *X*, *Y*, and either *data* or *mean*, and optionally *standard deviation* (the standard deviation estimator). If multiple samples were taken per position, the *data* label will be replaced by the *mean* label in the 3rd column. If the option to record standard deviation was selected (for multiple samples per position), a 4th column labeled *standard deviation* will be listed.

Table 5. XY file, line 5 field headers.

Field	Description
X	X position, in mm
Y	Y position, in mm
data	system output voltage
mean	mean output voltage
standard deviation	standard deviation of output voltages if more than 1

The actual X-Y data begins on line six and is laid out according to the field header labels in line 5. These lines will be 3 fields wide if the standard deviation was not recorded and 4 fields wide if it was. This data list continues for a variable number of lines, depending on how many X-Y points were sampled (=*X steps* × *Y steps)*.

After the data list, two final lines appear, corresponding to the experimental setup data from SurfinDUV. Earlier versions of SurfinDUV may have recorded fewer parameters, but new fields were always added to the end of the line. These fields are:

Table 6. XY file, 2nd to last line field headers.

Field	Description	Default Value
input power signal	Relative voltage level of the input beam. Not usually valid unless the experiment has been explicitly calibrated for absolute BRDF!	
det. area	Active area of detector (doesn't apply to electron detectors) in mm^2.	
det. distance	Distance of detector from sample in mm.	
responsivity	Estimated responsivity of detector in A/W (not usually used or valid).	
wavelength	Wavelength of experiment in nm.	
slits in	Width of monochromator input slits in mm.	
slits out	Width of monochromator output slits in nm (determines bandwidth).	
load resistance	Value in ohms of load resistor across	4700 Ω

	detector output.	
gate width	Width of gate pulse, in nS.	
gate delay	Delay of gate pulse from trigger, in nS	
GI sensitivity	GI sensitivity setting, in mV, must be 1000, 500, 200, 100, 50, 20, 10, or 5.	
beam width	Estimated beam width - usually needs to be explicitly calibrated.	
stage angle	Angle of stage, incidence angle.	
Pulse height	Voltage corresponding to single electron pulse from channeltron, if non-zero indicates measurement used discrete pulse filter, probably channeltron.	0
Polarization	May be u (unpolarized), s, or p	Unpolarized

The last line simply consists of the values corresponding to the fields of the previous line.

B. Angle Scans

Angle scan files are designed to store gated integrator output voltages at a range of detector positions, and contain information on the experimental setup used to gather the data.

As with X-Y scans, the first line always begins with the tag `SurfinDUV,` which may be followed by a time and date indicating the time and date of the original scan (the time and date stamps of the file may not correspond to the scan time).

The second line always contains the tag, *AngleScan.*

Line 3 contains the header for the scan setup data, *X Pos*, *Y Pos*, *Angle start*, *Angle end*, *Angle steps*, *subtracted background*, and *samples per point*.

Table 7. ANG file, line 3 field headers.

Field	Description
X Pos	The X position at which the scan was performed (see Chapter I for coordinate system).
Y Pos	The Y position at which the scan was performed (see Chapter I for coordinate system).
Angle start	The starting angular position of the scan.
Angle end	The final angular position of the scan.
Angle steps	The number of angle steps. Step size =(Angle end - Angle start)/(Angle steps-1)
Subtracted background	System dark background averaged over 10 samples, which is subtracted from all data readings. This is obtained by firing data acquisition pulses with the lamp off.
samples per point	The number of samples averaged per angle position.

Line 4 contains the values corresponding to the headers in line 3.

Line 5 contains the headers for the array of scan data, *angle*, and either *data* or *mean*, and optionally *standard deviation*. If multiple samples were taken per position, the *data* label will be replaced by the *mean* label in the 2nd column. If the option to record standard deviation was selected (for multiple samples per position), a 3rd column labeled *standard deviation* will be listed.

Table 8. ANG file, line 5 field headers.

Field	Description
angle	X position, in mm.
data	system output voltage
mean	mean output voltage
standard deviation	standard deviation of output voltages if more than 1 sample is taken

The actual angle data begins on line six and is laid out according to the field header labels in line 5. These lines will be 2 fields wide if the standard deviation was not recorded and 4 fields wide if it was. This data list continues for a variable number of lines, depending on how many positions were sampled (=*Angle steps)*.

After the data list, two final lines appear, corresponding to the experimental setup data from SurfinDUV. These have the same format as the final lines in XY files (see above and Table 6.)